TWO- AND-THREE-DIMENSIONAL MICROSTRUCTURAL MODELING OF ASPHALT PARTICULATE COMPOSITE MATERIALS USING A UNIFIED VISCOELASTIC-VISCOPLASTIC-VISCODAMAGE CONSTITUTIVE MODEL

A Dissertation

by

TAESUN YOU

Submitted to the Office of Graduate Studies of
Texas A&M University
in partial fulfillment of the requirements for the degree of

DOCTOR OF PHILOSOPHY

Chair of Committee,	Eyad Masad
Co-Chair of Committee,	Dallas Little
Committee Members,	Mary Beth Hueste
	J. N. Reddy
Head of Department,	Robin Autenrieth

August 2013

Major Subject: Civil Engineering

ABSTRACT

The main objective of this study is to develop and validate a framework for microstructural modeling of asphalt composite materials using a coupled thermo-viscoelastic, thermo-viscoplastic, and thermo-viscodamage constitutive model. In addition, the dissertation presents methods that can be used to capture and represent the two-dimensional (2D) and three-dimensional (3D) microstructure of asphalt concrete.

The 2D representative volume elements (RVEs) of asphalt concrete were generated based on planar X-ray Computed Tomography (CT) images. The 2D RVE consists of three phases: aggregate, matrix, and interfacial transmission zone (ITZ). The 3D microstructures of stone matrix asphalt (SMA) and dense-graded asphalt (DGA) concrete were reconstructed from slices of 2D X-ray CT images; each image consists of the matrix and aggregate phases. The matrix and ITZ were considered thermo-viscoelastic, thermo-viscoplastic, and thermo-viscodamaged materials, while the aggregate is considered to be a linear, isotropic elastic material.

The 2D RVEs were used to study the effects of variation in aggregate shape, distribution, volume fraction, ITZ strength, strain rate, and temperature on the degradation and micro-damage patterns in asphalt concrete. Moreover, the effects of loading rate, temperature, and loading type on the thermo-mechanical response of the 2D and 3D microstructures of asphalt concrete were investigated.

Finally, the model parameters for Fine Aggregate Mixture (FAM) and full asphalt mixture were determined based on the analysis of repeated creep recovery tests and

constant strain rate tests. These material parameters in the model were used to simulate the response of FAM and full asphalt mixture, and the results were compared with the responses of the corresponding experimental tests.

The microstructural modeling presented in this dissertation provides the ability to link the microstructure properties with the macroscopic response. This modeling combines nonlinear constitutive model, finite element analysis, and the unique capabilities of X-ray CT in capturing the material microstructure. The modeling results can be used to provide guidelines for designing microstructures of asphalt concrete that can achieve the desired macroscopic behavior. Additionally, it can be helpful to perform 'virtual testing' of asphalt concrete, saving numerous resources used in conducting real experimental tests.

DEDICATION

To my beloved wife, Hyesun, and sons, Anthony and Aiden

ACKNOWLEDGEMENTS

First of all, I would like to thank my committee co-chairs, Dr. Little and Dr. Masad, and my committee members, Dr. Reddy and Dr. Hueste, for their guidance and support throughout the course of this research.

Thanks also go to my friends and colleagues and the department faculty and staff for making my time at Texas A&M University a great experience. I would like to give special thanks to Dr. Abu Al-Rub, Dr. Kim, Dr. Masoud, and Dr. Kassem. I also want to extend my gratitude to the Qatar National Research Fund, which provided the economic support of my degree.

Finally, thanks to my parents and parents-in-law for their encouragement, my sister and brother-in-law for continuous concern, and to my wife for her patience and love.

TABLE OF CONTENTS

Page

Page

Page

LIST OF FIGURES

Page

Page

Page

Page

Page

Page

Page

Page

LIST OF TABLES

Page

CHAPTER I

INTRODUCTION

I.1 Problem Statement

Asphalt concrete, which is also known as hot mix asphalt (HMA), is the most widely used material in the construction of pavements. Asphalt concrete is a complex particulate composite that is comprised of mineral aggregates, asphalt binder, and air voids. The material can be separated into three distinct scales: (1) the micro-scale where fine fillers of 1-100 μm size exist surrounded by a binder-based matrix (i.e., the scale of the mastic phase); (2) the meso-scale where aggregates greater than 100 μm exist surrounded by the mastic, and (3) the macro-scale where the averaged, effective mechanical properties are used to represent the asphalt concrete composite. Mechanical properties of the composite asphalt concrete vary significantly depending on the mineral composition, proportions (mix design), size and distribution of aggregates, and physio-chemical and mechanical properties of the constituent materials.

One of the goals of this study is to predict the thermo-mechanical response at the meso-scale where three distinct material phases are considered: aggregate, matrix (or mastic), and interfacial transmission zone (ITZ). The ITZ is the zone representing the interface between the aggregate and the matrix. The effect of air voids is not considered due to high computational cost.

Numerous experimental studies have shown that the complex response of asphalt concrete is time-, rate-, and temperature-dependent [e.g. 1, 2]. However, only linear

elastic and linear viscoelastic models are mainly employed for simulating the thermo-mechanical behavior of asphalt concrete; these models are generally not sufficient to describe the material behavior. Very few studies have developed or even employed coupled thermo-viscoelastic, thermo-viscoplastic, and thermo-viscodamage (i.e., rate- and time-dependent damage) constitutive models to predict the complex response of asphalt concrete.

Although the macro-mechanical behavior of asphalt concrete can be obtained through experimental testing, it is not easy to characterize the micromechanical response of asphalt concrete in a laboratory because controlling the microstructural features including, for example, aggregate shape, size, distribution, and volume fraction is costly and time consuming. Therefore, it is highly desirable to develop accurate constitutive models and computational techniques that enable effective simulation of the micromechanical behavior of asphalt concrete. These simulation results provide an in-depth understanding of the influence of micromechanical characteristics on the overall macroscopic response.

Most of studies on microstructural modeling of asphalt concrete have focused on performing two-dimensional (2D) simulations [e.g.,3]. Very few studies used on three-dimensional (3D) microstructural modeling due to its high computational cost and because of the complexity in accurately representing the 3D morphology of asphalt concrete. In spite of these challenges, it is considered necessary to generate 3D microstructures in order to accurately describe the interactions among the mixture constituents.

I.2 Research Objectives

The primary objective of this study is to develop highly sophisticated and realistic 2D and 3D computational micromechanical models for asphalt concrete that predict the thermo-nonlinear-viscoelastic, thermo-viscoplastic, and thermo-viscodamage behavior of asphalt concrete. These models will enable effective simulation of the micromechanical behavior of asphalt concrete, and consequently, provide an understanding of the influence of micromechanical characteristics on the overall macroscopic response of asphalt mixtures under different loading conditions. These models will be capable of establishing the property-structure relationship based on simulating explicitly the material's microstructure and exploring the key microstructural features that control the overall macroscopic thermo-mechanical response of the asphalt mixture. Consequently, one can design the material for a specific desirable property (e.g., fracture toughness, resistance to permanent deformation) by directly tailoring the thermo-mechanical properties of its constituents and their distributions. Therefore, this dissertation includes four major objectives:

1. Develop sophisticated and realistic 2D and 3D microstructural finite element models for asphalt concrete microstructure based on X-ray Computed Tomography (CT) images.
2. Study the thermo-nonlinear-viscoelastic, thermo-viscoplastic, thermo-viscodamage behavior of the matrix (i.e., asphalt binder with fine aggregates and air voids) on the macroscopic response of asphalt concrete.

3. Investigate the effect of the microstructure of asphalt concrete on its thermo-mechanical behavior under various loading types and temperatures, and the fatigue damage of asphalt concrete.
4. Validate the model results by comparing it with corresponding experimental measurements on Fine Aggregate Mixture (FAM) and full mixtures.

I.3 Dissertation Outline

This dissertation consists of seven chapters. Chapter I includes the problem statement and the research objectives. Literature review on constitutive modeling of asphalt mixtures and microstructure-based models is presented in chapter II. The nonlinear constitutive model used in this research is described in chapter III. This model is developed based on the principles of nonlinear thermo-viscoelasticity, thermo-viscoplasticity, and thermo-viscodamage theory. Numerical implementation of the model is also provided in this chapter. Chapter IV presents 2D micromechanical modeling of asphalt concrete. Parametric study using various microstructures of asphalt concrete is conducted, and the effects of strain rate, temperature, and loading types are investigated using imaged-based microstructures. In chapter V, 3D microstructural modeling of asphalt concrete is addressed. The procedure to generate the microstructures of two types of asphalt concrete is explained and the effect of strain rate, temperature, and loading type is investigated using the reconstructed 3D microstructures. Chapter VI discusses the approach to identify the material parameters of FAM and full asphalt mixture. Experimental tests performed for the calibration of those parameters are presented and the identification process for viscoelastic, viscoplastic, and viscodamage

parameters is summarized. The identified material parameters are also validated in chapter VI. A series of experimental tests with FAM and full mixtures are used for this validation. Finally, chapter VII provides the summary and conclusions of this study. Recommendations are also described.

CHAPTER II

LITERATURE REVIEW

II.1 Introduction

This chapter includes the literature review on two main topics related to this dissertation: constitutive models and microstructure-based models. The constitutive models expand from linear viscoelasticity to more sophisticated nonlinear thermo-viscoelasticity, thermo-viscoplasticity, and thermo-viscodamage models. Schapery's viscoelasticity [4] and Perzyna's viscoplasticity theory [5] are mostly used to characterize the recoverable and irrecoverable response of asphalt concrete.

The microstructure-based models are divided primarily to 2D and 3D models. The 2D models are based on two different analysis methods: discrete element method (DEM) and finite element method (FEM). The 3D microstructure-based models develop into more realistic models. Three typical models are widely used to reconstruct the 3D microstructure of asphalt concrete: 1) idealized sphere or regular polyhedron model; 2) randomly-generated model; and 3) image-based model. The 3D models are more realistic than the 2D models but they are more time consuming need more advanced skills to generate. They also require more computational cost.

II.2 Constitutive Modeling of Asphalt Mixtures

The response of asphalt mixtures is very complex and is time-, rate-, and temperature-dependent as well as it exhibits both recoverable (viscoelastic) and irrecoverable (viscoplastic) deformations [e.g., 1]. Commonly, Schapery's single integral model [4] is

used to describe the recoverable (nonlinear viscoelastic) response of asphalt mixtures and has been implemented using finite-element codes [6-9].

Lee and Kim [8] proposed a coupled viscoelastic and damage constitutive modeling approach of asphalt concrete under cyclic loading conditions. They combined the Schapery's extended elastic-viscoelastic correspondence principle with a generalization of microcrack law that accounted for time-dependent damage growth in asphalt concrete. The model parameters were identified by conducting controlled-strain tensile uniaxial fatigue tests. Then, the constitutive model was validated by predicting the stress-strain behavior under controlled stress mode as well as monotonic loading with varying strain rates.

Sadd et al. [10] employed damage mechanics to develop a finite element micromechanical model for asphalt concrete. The model was implemented in Abaqus [11], and a series of indirect tensile test were simulated to investigate the effect of various microstructures of asphalt concrete specimens on their response. The comparison between the model damage evolution and the experimental photographic data qualitatively showed reasonable relationships.

Kim et al. [12] developed a computational constitutive model to predict damage and fracture failure of asphalt concrete with a nonlinear viscoelastic cohesive zone model [13]. In this model, asphalt concrete had three components: elastic aggregate particles, viscoelastic matrix, and viscoelastic cohesive zones that are subjected to damage due to cracking. Small-scale fracture properties locally measured from simple fracture tests

were utilized to show that the model could predict the response of asphalt concrete due to microcracking.

Haj-Ali and Muliana [6] studied a recursive-iterative numerical algorithm for the nonlinear viscoelastic behavior of isotropic materials and structures. This numerical modeling approach was used later by Huang et al. [7] for asphalt concrete. They integrated Schapery's 3D nonlinear viscoelastic model [14] with a displacement-based finite element environment. The proposed numerical algorithm was verified with experimental data for a glassy amorphous polymer.

Huang et al. [7] implemented Schapery's nonlinear viscoelasticity in a finite element code using the recursive-iterative method developed by Haj-Ali and Muliana [6] to characterize the response of asphalt concrete. The model parameters were identified from the experimental results using two asphalt mixtures under different temperatures, frequencies, and strain level. The model was then validated by comparing the finite element prediction with the experimental results from creep tests.

Masad et al. [9] analyzed the nonlinear viscoelastic behavior of unaged and aged asphalt binders using the implemented nonlinear viscoelastic constitutive model with the recursive-iterative algorithm [6]. Dynamic shear rheometer tests under different temperatures and frequencies were conducted to establish the master curve for the nonlinear viscoelastic materials.

Perzyna's viscoplasticity theory [5] is the most used approach to describe the irrecoverable (viscoplastic) response of asphalt concrete [e.g.,15, 16-21]. In Lu and Wright [16], asphalt concrete was considered as visco-elastoplastic material. They

employed Perzyna's viscoplasticity theory and the visco-elastoplastic constitutive model in a finite element code. The results from the finite element method and the analytical method had a good agreement, meaning successful simulation of pavement performance evaluation and development of permanent deformations in asphaltic layers.

Seibi et al. [21] proposed an elastic-viscoplastic constitutive model for asphalt concrete under high rates of loading. They employed the Drucker-Prager yield criterion in the constitutive model and implemented the model in the Abaqus finite element code [11]. The model's material parameters were calibrated from field tests using optimization technique; however, those models considered the recoverable and irrecoverable responses independently (i.e., the viscoelastic behavior did not affect the viscoplastic response).

Masad et al. [18] presented a constitutive modeling to characterize the viscoplastic response of asphalt concrete. An anisotropic non-associated flow rule based on the Drucker-Prager yield surface was chosen to describe the field stress path and material properties related to permanent deformation at high temperatures. It was found that the material parameters for this model were related to anisotropy, damage, and aggregate characteristics. Masad et al. [17] extended this work to relate the parameters of the continuum model to microstructure distribution and characteristics. Consequently, they implemented the model into a finite element code using the Newton-Raphson iteration scheme and simulated experimental tests under various confinement stress levels and strain rates.

Saadeh et al. [20] further extended the model by Masad et al. [17] by including a coupled nonlinear viscoelastic-viscoplastic constitutive model. The recoverable (viscoelastic) and irrecoverable (viscoplastic) anisotropic responses were accounted for using Schapery's viscoelasticity [4] and Perzyna's viscoplasticity [5], respectively.. The material parameters were identified using the results from triaxial repeated creep-recovery tests on three different asphalt mixtures with different aggregate characteristics. The relationship of the identified parameters to mix properties was also found. Using the proposed model, Saadeh and Masad [19] investigated the relation between microstructure properties of asphalt concrete such as aggregate characteristics, aggregate orientation, air void distribution, and predicted response. The influence of asphalt mixture microstructure on material response in terms of hardening, softening, and dilation was determined using X-ray CT.

Huang et al. [22] conducted 3D finite element simulations to obtain the response of a three-layer asphalt pavement structure under repeated loading at different temperatures using the nonlinear viscoelastic-viscoplastic constitutive model. The material parameters for the model were identified using creep-recovery test results at different stress levels and temperatures.

However, none of the above aforementioned studies considered the coupled thermo-viscoelastic, thermo-viscoplastic, and thermo-viscodamage behavior of asphalt mixes which are very important for predicting the overall thermo-mechanical response of asphaltic mixtures. Darabi et al. [23, 24] developed a coupled thermo-viscoelastic, thermo-viscoplastic, and thermo-viscodamage model for asphalt concrete based on laws

of thermodynamics. The model retrieves Schapery's nonlinear viscoelastic model [4] to predict the recoverable deformations, Perzyna-type viscoplasticity [5] with a generalized Drucker-Prager-type yield surface [17] to predict the irrecoverable deformations and derives a new generalized viscodamage law. The model was verified using a series of experimental tests including creep-recovery, creep, and uniaxial constant strain rate tests at various temperatures, stress levels, and strain rates.

Abu Al-Rub [25] developed a micro-damage healing model by improving the integrated viscoelastic, viscoplastic, and viscodamage model in order to predict the fatigue life of asphalt pavement mixtures. Single creep-recovery tests and creep tests were conducted for the identification of the model parameters. The micro-damage healing model was calibrated and validated using the uniaxial repeated creep-recovery tests. The modeling approach by Abu Al-Rub [25] and Darabi et al. [23, 24] was considered the most complete model for asphalt concrete as it was capable of considering the nonlinear response at a wide range of temperatures, stresses, loading rates, and damage levels, and adopted in this dissertation.

II.3 Microstructure-based Models

II.3.1 2D Micromechanical Models

Change and Meegoda [26] investigated temperature effects on asphalt concrete using the DEM. Burger's model was used to predict the viscoelastic response, and a 150-article assembly model was created for simulating triaxial compression tests at four different temperatures.

Abbas et al. [27] used the DEM to analyze the viscoelastic response of asphalt mixtures. The microstructure of asphalt mixtures was captured by X-ray CT, and the captured grayscale images were processed into binary images (i.e., black and white images). The material parameters of viscoelastic contact models were identified using the rheological measurements and used to simulate simple performance test.

Mahmoud et al. [28] studied the influences of aggregate gradation, shape, stiffness, and strength on fracture in asphalt concrete using the DEM and image processing techniques. Various microstructures with different internal structures were generated using the imaged scanned by X-ray CT.

However, only simple viscoelastic constitutive model was used due to relatively high computational cost. In order to overcome this drawback, FEM has been used. An image-based finite element (FE) model of asphalt concrete microstructure was developed by Masad and Somadevan [29]. The microstructure had two phases: aggregate and mastic. The viscoelastic constitutive relationship was used to represent the mastic phase. The influence of localized distribution on the asphalt concrete nonlinear response was studied using the image-based microstructure.

Papagiannakis et al. [30] analyzed asphalt concrete microstructures using the FEM. X-ray image analysis techniques were used to capture the microstructure of asphalt concrete. Aggregate phase was considered as linear elastic, while binder phase was considered as either linear viscoelastic or nonlinear viscoelastic. Simulated dynamic analysis using the image-based microstructure of asphalt concrete was compared with the corresponding experimental measurements.

Sadd et al. [10] studied the micromechanical response of asphalt concrete employing a rate- and time-independent elastic-damage constitutive model. Circular shape model was represented to simulate indirect tensile tests using the FEM in order to investigate the effect of various specimen microstructures on the sample responses. Using this micromechanical FE model, Dai and Sadd [31] performed a parametric study to investigate micromechanical effects of aggregate orientation, aggregate shape, aggregate percentage, aggregate gradation, and model porosity, based on continuum damage mechanics. Dai et al. [32] extended this work to characterized the linear and damage-coupled viscoelastic response of asphalt mixture. Schapery nonlinear viscoelastic model and rate-independent and rate-dependent damage mechanisms were implemented into a finite element incremental algorithm with recursive method.

Dessouky et al. [33] proposed a methodology to analyze microstructure of asphalt concrete using effective local material properties and strain gradient elasticity. The methodology was implemented in a FE code to analyze a number of asphalt mixes with different aggregate types and size distributions.

Woldekidan [34] proposed a meso-scale porous asphalt concrete model with viscoelastic and plastic binder to solve the problem of porous asphalt concrete raveling. Mo et al. [35] extended this work to predict the meso-scale response of porous asphalt concrete in order to investigate the effects of different stress states.

Cohesive zone models were developed by Kim et al. [3], in order to model the interfaces between aggregates and the mastic and modeled the mastic as a linear viscoelastic. The model was implemented in a FE code and a variety of image-based

microstructures were generated to determine appropriate representative volume elements (RVEs) of asphalt concrete mixtures.

II.3.2 3D Microstructural Models

Due to the very high computational cost in conducting 3D micromechanical modeling and complexity in generating accurate representation of the asphalt concrete microstructural morphology, most of the current microstructural modeling of asphalt concrete has focused on performing 2D analysis. The 3D microstructural modeling of asphalt concrete has been the focus of very few studies recently.

Collop et al. [36] generated a 3D idealized mixture model to simulate the viscoelastic response of asphalt mixtures using the DEM. Sphere aggregate shapes were used to generate the 3D model used for conducting uniaxial and triaxial compressive creep tests. Wu et al. [37] extended their work into simulating constant compressive tests with various strain rates at different temperatures using the DEM and a 3D idealized microstructural model (see Figure II-1). Burger's viscoelastic model was employed to describe time dependent shear and tensile contact stiffness.

Mo et al. [38] applied the FEM to 2D and 3D microstructural models for ravelling analysis of porous asphalt concrete. As shown in Figure II-2, sphere particles were used to represent the morphology of grains in porous asphalt concrete and considered as linear elastic, while Burger's linear viscoelastic model was employed to predict the behavior of mortar in porous asphalt concrete.

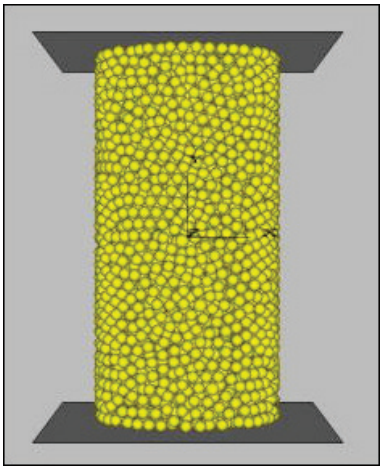

Figure II-1. Idealized microstructural model [37].

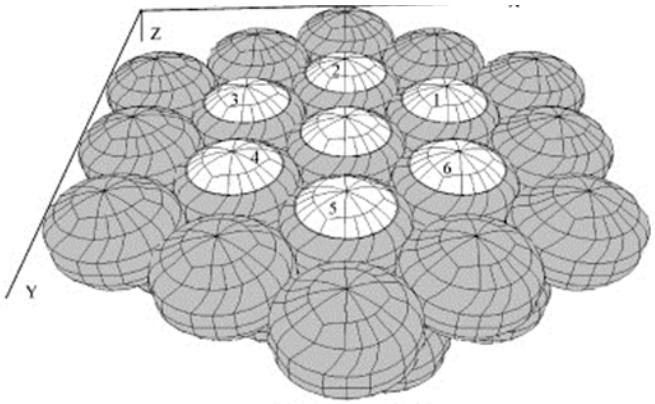

Figure II-2. 3D microstructure with sphere particles [38].

Liu et al. [39-41] employed the Burger's viscoelastic response of 3D randomly-generated microstructural model (see Figure II-3) of asphalt concrete using the DEM. Irregular polyhedron shapes were used to represent aggregate particles in the microstructures of asphalt concrete with different gradation [39]. Using these microstructures, uniaxial dynamic modulus tests were conducted with the DEM. Liu et

al. [40] improved this work by reducing computational cost for discrete element analysis. The computation time was reduced significantly by conducting the discrete element modeling with the virtual frequencies and the corresponding modified Burger's model parameters. The effects of aggregate sphericity, orientation, and angularity on creep response were studied by Liu et al. [41]. Creep compliance tests were simulated using the discrete element modeling with 3D randomly-generated microstructure of asphalt concrete. Various 3D microstructures had different aggregate sphericity index, fractured faces, and orientation angles.

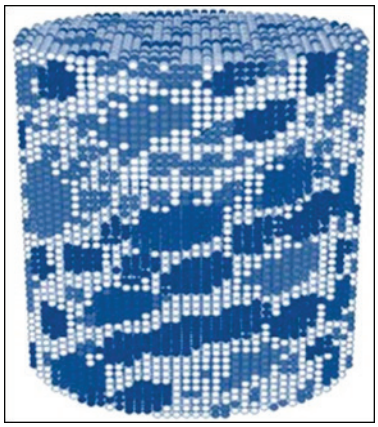

Figure II-3. 3D randomly-generated microstructural model [40].

Although randomly generated models were more realistic than idealized models (i.e. sphere/regular polyhedron model), they were still not sufficient to represent the complex microstructure of asphalt concrete with highly irregular shaped aggregates. To overcome this drawback, X-ray CT images were utilized. Wang [42] developed a 3D digital asphalt

concrete specimen based on CT images to predict the viscoplastic response using the FEM. A variety of tests such as the indirect tensile test, dynamic modulus test, uniaxial compressive test in both macroscopic and microscopic levels were simulated using the 3D digital specimen of asphalt concrete.

Image-based 2D and 3D discrete element models were created by You et al. [43], as shown Figure II-4. The linear elastic relationship between the contact force and relative displacement between particles was used to simulate triaxial compressive tests using the 2D and 3D models that included randomly distributed air voids.

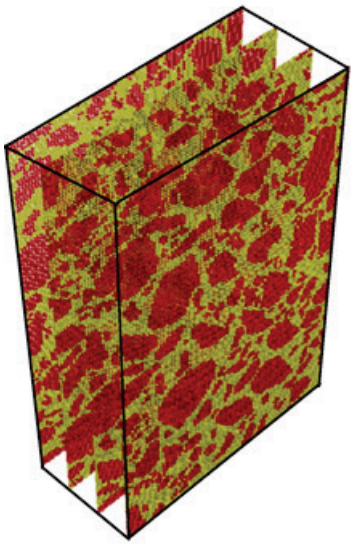

Figure II-4. 3D discrete element model [43].

You et al. [44] conducted dynamic modulus simulation of asphalt concrete using 2D and 3D microstructures that were reconstructed using the X-ray CT images. The predicted dynamic modulus from various 2D and 3D microstructures were compared

with the corresponding experimental measurements. You et al. [45] extended these works to viscoelastic modeling of creep compliance tests for asphalt concrete. The 3D microstructural-based discrete element models for asphalt concrete were developed, and Burger's linear viscoelastic model was employed to simulate the time-dependent response of asphalt concrete. The predicted creep responses at different temperatures were compared with the experimental measurements.

Dai [46] predicted the elastic damage response of stone-based model using the proposed 3D micromechanical finite-element network model. Sphere shapes were used for the idealized stone-based model by which indirect tensile test and compressive test were simulated. Dai [47] generated the 2D and 3D microstructures (see Figure II-5) of stone-based materials such as asphalt concrete to predict its viscoelastic behavior. Maxwell-type viscoelastic model was applied and X-ray CT imaging techniques were utilized to capture the internal microstructure of asphalt concrete. Using the image-based microstructures, dynamic modulus tests were simulated for comparing the experimental measurements.

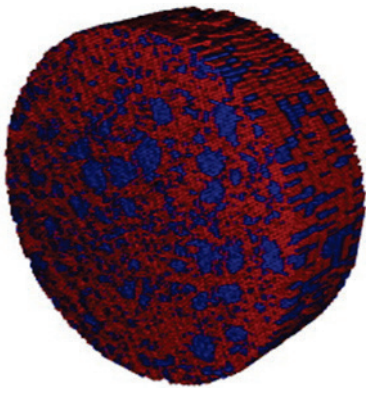

Figure II-5. 3D microstructure of stone-based materials [47].

However, none of the 2D and 3D microstructures was enough to represent complicated morphology of asphalt concrete. They also employed linear elastic or linear viscoelastic models constitutive models. In this dissertation, more sophisticated and realistic 2D and 3D microstructures of asphalt concrete were developed based on X-ray CT images.

II.4 Summary

The literature review on constitutive models and microstructure-based models was presented in this chapter. Most of the constitutive models that have been developed and used for asphalt concrete did not account for the coupled effects of temperature, nonlinear viscoelasticity, viscoplasticity, and viscodamage to describe the complex response of asphalt concrete. Moreover, the majority of the 2D and 3D models of asphalt concrete used DEM that was computationally more expensive in comparison with FEM. In addition, these DEM-based models were limited in capturing the nonlinear constitutive behavior of the mixture constituents. The 3D microstructure-based models used idealized sphere or randomly-generated shapes for aggregate phase. Consequently, there is a need to develop 3D finite element models of asphalt concrete microstructure that consider the coupled nonlinear thermo-mechanical behavior of asphalt concrete and employ realistic representation of the microstructure.

CHAPTER III

NONLINEAR CONSTITUTIVE MODEL*

III.1 Introduction

In this chapter, a summary of the main constitutive equations for the derived thermodynamic-based coupled thermo-viscoelastic, thermo-viscoplastic, and thermo-viscodamage model by Huang et al. [7, 15], Masad et al. [48], Abu Al-Rub et al. [25], and Darabi et al. [23, 49] is presented. A detailed numerical integration algorithm for these constitutive equations is also presented. In this model, Schapery's [4] nonlinear viscoelastic model and Perzyna-type [5] viscoplasticity with a generalized Drucker-Prager-type yield surface [17] were employed to predict the recoverable and the irrecoverable deformations, respectively. Additionally, the model included a viscodamage law by Darabi et al. [23, 49].

The material parameters for the model can be uniquely and systematically identified using a small number of simple experimental tests such as dynamic modulus test, repeated creep-recovery test, and constant strain rate test. Furthermore, the model was validated with extensive experimental tests including creep, single creep-recovery, repeated creep-recovery, triaxial, and constant strain rate tests under various temperatures, stress levels, confinement levels, and strain rates in compression and

---

tension [e.g., 15, 23, 24, 25, 49]. The model and its numerical implementation allow for choosing the desired parts among the whole constitutive model under the specific conditions in order to save the computational cost and reduce the required experimental tests for the identification of the material parameters. For example, only viscoelastic and viscodamage parts can be selected to predict the response of the material at low temperature, where viscoplasticity can be neglected. Last but not least, the different parts in the model are coupled. This model is used throughout this dissertation to represent the behavior of the mixture matrix or FAM as part of the microstructural model. It is noted that this chapter is the part of Abu Al-Rub et al. [50].

III.2 Strain Decomposition and Effect Stress

Assuming small deformations, the total strain is decomposed into a viscoelastic (recoverable) strain and the viscoplastic (irrecoverable) strain, such that:

$$\varepsilon_{ij} = \varepsilon_{ij}^{ve} + \varepsilon_{ij}^{vp} \tag{3.1}$$

where $\boldsymbol{\varepsilon}$, $\boldsymbol{\varepsilon}^{ve}$, and $\boldsymbol{\varepsilon}^{vp}$ are the total, viscoelastic, and viscoplastic strain tensors, respectively.

Adapting the continuum damage mechanics framework pioneered by Kachanov [51] and employing an isotropic damage assumption, the effective (undamaged) stress tensor $\bar{\boldsymbol{\sigma}}$ can be defined by

$$\bar{\sigma}_{ij} = \frac{\sigma_{ij}}{1-\phi} \tag{3.2}$$

where $\boldsymbol{\sigma}$ is the nominal stress tensor, $\bar{\boldsymbol{\sigma}}$ is the effective (undamaged) stress tensor, and ϕ is the damage density (a degradation parameter) that has a range from 0 to 1, where

$\phi = 0$ means that the material is intact and $\phi = 1$ means that the material is fully damaged.

In the following discussion, all the constitutive equations are expressed in terms of the effective stress $\bar{\boldsymbol{\sigma}}$. Moreover, the strain equivalence hypothesis is adapted in this work which states that the strain in the nominal (damaged) configuration is equal to the strain in the effective (undamaged) configuration [refer to Abu Al-Rub and Voyiadjis [52] for more details on the most common transformation hypotheses in CDM]. This hypothesis is employed in the current study since it greatly simplifies the finite element implementation of the current coupled viscoelastic, viscoplastic, and viscodamage constitutive model.

III.3 Nonlinear Thermo-viscoelasticity

The Schapery's nonlinear viscoelasticity theory [4] is adopted to model the viscoelastic component such that for one-dimensional problems one can write:

$$\varepsilon^{ve,t} = g_0 D_0 \bar{\sigma}^t + g_1 \int_0^t \Delta D^{\left(\psi^t - \psi^\tau\right)} \frac{d\left(g_2 \bar{\sigma}^t\right)}{d\tau} d\tau \tag{3.3}$$

where $\varepsilon^{ve,t}$ is the viscoelastic strain at time t; D_0 is the instantaneous compliance; ΔD is the transient compliance; g_0, g_1, and g_2 are the non-linear parameters which are functions of the effective stress $\bar{\sigma}^t$; and ψ^t is the reduced time given by:

$$\psi^t = \int_0^t \frac{d\xi}{a_T a_s a_e} \tag{3.4}$$

where a_T, a_s, and a_e are the temperature, strain or stress, and the environment time shift factors, respectively. To present the transient compliance, the Prony series is used as follows:

$$\Delta D^{\psi^t} = \sum_{n=1}^{N} D_n \left[1 - \exp\left(-\lambda_n \psi^t\right)\right] \tag{3.5}$$

where N is the number of terms in Prony series and D_n is the n^{th} coefficient of Prony series associated with the n^{th} retardation time λ_n. The superimposed t and τ indicate the response at specific time. It is noteworthy that the model in Eq. (3.3) is referred to as the nonlinear viscoelastic model since the stress-strain relationship depends also on the nonlinear parameters g_0, g_1, and g_2, which are functions of the stress and the strain magnitudes. Moreover, asphalt mixtures show a nonlinear viscoelastic response even at small deformations where the properties of the asphalt mix change with deformation such that a linear viscoelastic model (i.e., setting $g_0 = g_1 = g_2 = 1$) is insufficient to predict the response of asphaltic mixtures [7]. This has been also demonstrated for other materials, such as polymers, by several other researchers [e.g. 6, 14]. Lai and Bakker [14] generalized Schapery's nonlinear viscoelastic model to 3D problems by dividing the nonlinear viscoelastic strain into its deviatoric and volumetric components, such that:

$$\varepsilon_{ij}^{ve} = e_{ij}^{ve} + \frac{1}{3}\varepsilon_{kk}^{ve}\delta_{ij} = \frac{1}{2\overline{G}}\overline{S}_{ij} + \frac{\overline{\sigma}_{kk}}{9K}\delta_{ij} = \frac{\overline{J}}{2}\overline{S}_{ij} + \frac{\overline{B}}{9}\overline{\sigma}_{kk}\delta_{ij} \tag{3.6}$$

where $\boldsymbol{e}^{ve}$ and ε_{kk}^{ve} are the deviatoric stress tensor and the volumetric strain, respectively. $\overline{S}$ is the deviatoric stress tensor; $\overline{\sigma}_{kk}$ is the volumetric stress; and $\overline{G}$ and $\overline{K}$ are the effective shear and bulk moduli for undamaged material and are expressed as:

$$\overline{G} = \frac{\overline{E}}{2\left(1+\overline{\nu}\right)}, \qquad \overline{K} = \frac{\overline{E}}{3\left(1-2\overline{\nu}\right)} \tag{3.7}$$

where $\overline{E}$, $\overline{\nu}$, $\overline{J}$ and $\overline{B}$ are the Young's modulus, the Poisson's ratio, the shear compliance, and the bulk compliance in the effective configuration, respectively. Applying the Schapery's model in Eq. (3.3), the deviatoric and volumetric components of the total strain tensor are given by:

$$e_{ij}^{ve,t} = \frac{1}{2} g_0^t \overline{J}_0 \overline{S}_{ij}^t + \frac{1}{2} g_1^t \int_0^t \Delta \overline{J}^{\left(\psi^t - \psi^\tau\right)} \frac{d\left(g_2^\tau \overline{S}_{ij}^\tau\right)}{d\tau} d\tau \tag{3.8}$$

$$\varepsilon_{kk}^{ve,t} = \frac{1}{3} g_0^t \overline{B}_0 \overline{\sigma}_{kk}^t + \frac{1}{3} g_1^t \int_0^t \Delta \overline{B}^{\left(\psi^t - \psi^\tau\right)} \frac{d\left(g_2^\tau \overline{\sigma}_{kk}^t\right)}{d\tau} d\tau \tag{3.9}$$

where $\overline{J}_0$ and $\overline{B}_0$ are the instantaneous effective elastic shear and bulk compliances, respectively.

Assuming that Poisson's ratio in the effective configuration $\overline{\nu}$ is time-independent and using Prony series in Eq. (3.5), the deviatoric and volumetric components of the total strain tensor can be presented in terms of the hereditary integral formulation as follows:

$$\begin{aligned} e_{ij}^{ve,t} = {} & \frac{1}{2}\left[g_0^t \overline{J}_0 + g_1^t g_2^t \sum_{n=1}^{N} \overline{J}_n - g_1^t g_2^t \sum_{n=1}^{N} \overline{J}_n \frac{1-\exp\left(-\lambda_n \Delta\psi^t\right)}{\lambda_n \Delta\psi^t} \right] \overline{S}_{ij}^t \\ & - \frac{1}{2} g_1^t \sum_{n=1}^{N} \overline{J}_n \left[\exp\left(-\lambda_n \Delta\psi^t\right) q_{ij,n}^{t-\Delta t} - g_2^{t-\Delta t} \frac{1-\exp\left(-\lambda_n \Delta\psi^t\right)}{\lambda_n \Delta\psi^t} \overline{S}_{ij}^{t-\Delta t} \right] \end{aligned} \tag{3.10}$$

$$\varepsilon_{kk}^{ve,t} = \frac{1}{3}\left[g_0^t \bar{B}_0 + g_1^t g_2^t \sum_{n=1}^{N} \bar{B}_n - g_1^t g_2^t \sum_{n=1}^{N} \bar{B}_n \frac{1-\exp\left(-\lambda_n \Delta\psi^t\right)}{\lambda_n \Delta\psi^t} \right] \bar{\sigma}_{kk}^t$$
$$-\frac{1}{3} g_1^t \sum_{n=1}^{N} \bar{B}_n \left[\exp\left(-\lambda_n \Delta\psi^t\right) q_{kk,n}^{t-\Delta t} - g_2^{t-\Delta t} \frac{1-\exp\left(-\lambda_n \Delta\psi^t\right)}{\lambda_n \Delta\psi^t} \bar{\sigma}_{kk}^{t-\Delta t} \right] \tag{3.11}$$

where Δt is the time increment, $q_{ij,n}$ and $q_{kk,n}$ are the deviatoric and volumetric hereditary integrals associated with each Prony series term n, respectively.

III.4 Thermo-viscoplasticity

From Eq. (3.1), the total strain rate $\dot{\varepsilon}_{ij}$ is expressed as:

$$\dot{\varepsilon}_{ij} = \dot{\varepsilon}_{ij}^{ve} + \dot{\varepsilon}_{ij}^{vp} \tag{3.12}$$

where $\dot{\varepsilon}_{ij}^{ve}$ is the viscoelastic strain rate and $\dot{\varepsilon}_{ij}^{vp}$ is the viscoplastic strain rate. Perzyna [5] proposed the viscoplastic flow rule, as follows:

$$\dot{\varepsilon}_{ij}^{vp} = \Gamma^{vp} \left\langle \Phi\left(f\right) \right\rangle^N \frac{\partial g}{\partial \bar{\sigma}_{ij}} \tag{3.13}$$

where g is the plastic potential function, N is the viscoplastic rate sensitivity exponent, and Γ^{vp} is the viscoplastic viscosity parameter such that $1/\Gamma^{vp}$ represents the viscoplasticity relaxation time, which is assumed to be a function of a time-temperature shift factor a_T such that:

$$\Gamma^{vp} = \frac{\Gamma_0^{vp}}{a_T} \tag{3.14}$$

where Γ_0^{vp} is the viscoplastic viscosity at the reference temperature. The function Φ in Eq. (3.13) is the overstress function expressed in terms of the yield function f, such that:

$$\Phi(f) = \frac{f}{\sigma_y^0} \tag{3.15}$$

where $\langle\ \rangle$ is the Macaulay brackets defined by $\langle x \rangle = (\|x\| + x)/2$ and σ_y^0 is a yield stress quantity.

In this work, the modified Drucker-Prager yield functions, presented in Masad et al. [17], is adopted and given by:

$$f = \bar{\tau} - \alpha \bar{I}_1 - \kappa(p) \leq 0 \tag{3.16}$$

where α is a material parameter related to the material's internal friction, $\bar{I}_1$ is the first stress invariant, p is the effective viscoplastic strain, and $\kappa(p)$ is an isotropic hardening function associated with the cohesive characteristics of the material and expressed as [53]:

$$\kappa = \kappa_0 + \kappa_1 \left\{1 - \exp\left[-\kappa_2 (p)\right]\right\} \tag{3.17}$$

where κ_0, κ_1, and κ_2 are material parameters, which define the initial yield stress, the saturated yield stress, and the strain hardening rate, respectively. In addition, $\bar{\tau}$ is the deviatoric effective shear stress modified to distinguish between the asphaltic material behavior under compression and extension loading conditions and can be expressed as follows [54]:

$$\bar{\tau} = \frac{\sqrt{3\bar{J}_2}}{2}\left[1 + \frac{1}{d} + \left(1 - \frac{1}{d}\right)\frac{3\bar{J}_3}{\sqrt{3\bar{J}_2^3}}\right] \tag{3.18}$$

where $\bar{J}_2 = \bar{S}_{ij}\bar{S}_{ij}/2$ and $\bar{J}_3 = (1/2)\bar{S}_{ij}\bar{S}_{jk}\bar{S}_{ki}$ are the second and third deviatoric stress invariants, respectively, and d is a material parameter representing the ratio of the yield stress in uniaxial tension to the one in uniaxial compression.

However, because the use of an associative flow rule (i.e., $g = f$) tends to overestimate the dilation compared with experimental measurements [17, 18], α in Eq. (3.16) is replaced with β to define the plastic potential function in Eq. (3.19) for a non-associative viscoplastic flow rule; β controls the dilation or contraction behavior of the material.

$$g = \bar{\tau} - \beta \bar{I}_1 \tag{3.19}$$

The effective viscoplastic strain in Eqs. (3.16) and (3.17) can be expressed as [55]:

$$\dot{\varepsilon}_e^{vp} = A^{-1}\sqrt{\dot{\varepsilon}_{ij}^{vp}\dot{\varepsilon}_{ij}^{vp}} \tag{3.20}$$

where $A = \sqrt{1 + 2\left(\dfrac{0.5 + \beta/3}{1 - \beta/3}\right)^2}$. From Eq. (20), $\partial g/\partial \bar{\sigma}_{ij}$ in Eq. (3.13) is written as:

$$\frac{\partial g}{\partial \bar{\sigma}_{ij}} = \frac{\partial \bar{\tau}}{\partial \bar{\sigma}_{ij}} - \frac{1}{3}\beta\delta_{ij} \tag{3.21}$$

where $\partial \bar{\tau}/\partial \bar{\sigma}_{ij}$ is given by

$$\frac{\partial \bar{\tau}}{\partial \bar{\sigma}_{ij}} = \frac{1}{2}\left[\frac{\dfrac{\partial \bar{J}_2}{\partial \bar{\sigma}_{ij}}}{2\sqrt{\bar{J}_2}}\left(1 + \frac{1}{d}\right) + \left(\frac{\dfrac{\partial \bar{J}_3}{\partial \bar{\sigma}_{ij}}\bar{J}_2 - \dfrac{\partial \bar{J}_2}{\partial \bar{\sigma}_{ij}}\bar{J}_3}{\bar{J}_2^2}\right)\left(1 - \frac{1}{d}\right)\right] \tag{3.22}$$

where $\partial \bar{J}_2/\partial \bar{\sigma}_{ij} = 3\bar{S}_{ij}$, and $\partial \bar{J}_3/\partial \bar{\sigma}_{ij} = (27/2)\bar{S}_{ik}\bar{S}_{kj} - 3\bar{J}_2\delta_{ij}$.

III.5 Thermo-viscodamage Theory

The damage evolution $\dot{\phi}$ can be a function of the following variables:

$$\dot{\phi} = F\left[\bar{\sigma}_{ij}(t), \bar{\sigma}_{kk}(t), \varepsilon_{ij}(t), \dot{\varepsilon}_{ij}(t), \phi(t)\right] \tag{3.23}$$

In this study, an exponential type of the damage evolution law, proposed by Darabi et al. [24], is modified and given by

$$\dot{\phi} = \Gamma^{vd}\left(\frac{\bar{Y}}{Y_0}\right)^q \left(\varepsilon_{eff}^{Tot}\right)^k (1-\phi)^2 \tag{3.24}$$

where Γ^{vd} is a damage viscosity parameter, Y_0 is the reference damage force, q and k are a material parameter, and ε_{eff}^{Tot} is the effective total strain presented by

$$\varepsilon_{eff}^{Tot} = \sqrt{\varepsilon_{ij}\varepsilon_{ij}} \tag{3.25}$$

In addition, the damage viscosity parameter Γ^{ϕ} is assumed to be temperature-dependent as follows:

$$\Gamma^{vd} = \frac{\Gamma_0^{vd}}{a_T} \tag{3.26}$$

where Γ_0^{vd} is the reference damage viscosity parameter; q is the stress-dependency parameter; and $\bar{Y}$ is the damage driving force in the effective undamaged configuration, which can be assumed to have the following form that includes the effects of damage under compressive and extension loading conditions:

$$\bar{Y} = \bar{\tau}^{vd} - \alpha \bar{I}_1 \tag{3.27}$$

where $\bar{\tau}^{vd}$ is given by

$$\overline{\tau}^{vd} = \frac{\sqrt{3\overline{J}_2}}{2}\left[1+\frac{1}{d^{vd}}+\left(1-\frac{1}{d^{vd}}\right)\frac{3\overline{J}_3}{\sqrt{3\overline{J}_2^3}}\right] \tag{3.28}$$

Substituting Eqs. (3.26) and (3.27) into Eq. (3.24) gives the following thermo-viscodamage evolution law:

$$\dot{\phi} = \frac{\Gamma_0^{vd}}{a_T}\left[\frac{\overline{\tau}^{vd}-\alpha\overline{I}_1}{Y_0}\right]^q (1-\phi)^2 \left(\varepsilon_{eff}^{Tot}\right)^k \tag{3.29}$$

III.6 Numerical Implementation

The numerical integration for the nonlinear viscoelastic, viscoplastic, and viscodamaged model are described in this section. One can obtain the values at the end of the time increment (t) from the values of stress and internal values at the previous step ($t-\Delta t$), having the given strain increment, $\Delta\varepsilon_{ij} = \varepsilon_{ij}^{t+\Delta t} - \varepsilon_{ij}^{t}$. The total strain tensor in Eq. (3.1), the effective viscoplastic in Eq. (3.20), and the effective stress tensor in Eq. (3.2) can be decomposed as follows:

$$\varepsilon_{ij}^{t} = \varepsilon_{ij}^{nve,t} + \varepsilon_{ij}^{vp,t} = \varepsilon_{ij}^{t-\Delta t} + \Delta\varepsilon_{ij}^{t} = \varepsilon_{ij}^{nve,t-\Delta t} + \varepsilon_{ij}^{vp,t-\Delta t} + \Delta\varepsilon_{ij}^{nve,t} + \Delta\varepsilon_{ij}^{vp,t} \tag{3.30}$$

$$\varepsilon_{e}^{vp,t} = \varepsilon_{e}^{vp,t-\Delta t} + \Delta\varepsilon_{e}^{vp,t} \tag{3.31}$$

$$\overline{\sigma}_{ij}^{t} = \overline{\sigma}_{ij}^{t-\Delta t} + \Delta\overline{\sigma}_{ij}^{t} \tag{3.32}$$

The viscoelastic bulk and deviatoric strain increments can be derived from Eqs. (3.10) and (3.11) as follows [7]:

$$\begin{aligned}
\Delta e_{ij}^{nve,t} &= e_{ij}^{nve,t} - e_{ij}^{nve,t-\Delta t} \\
&= \overline{J}^{t} S_{ij}^{t} - \overline{J}^{t-\Delta t} S_{ij}^{t-\Delta t} - \frac{1}{2}\sum_{n=1}^{N}\overline{J}_n\left[g_1^t \exp\left(-\lambda_n \Delta\psi^t\right) - g_1^{t-\Delta t}\right] q_{ij,n}^{t-\Delta t} \\
&\quad - \frac{1}{2} g_2^{t-\Delta t}\sum_{n=1}^{N}\overline{J}_n\left\{g_1^{t-\Delta t}\left[\frac{1-\exp\left(-\lambda_n\Delta\psi^{t-\Delta t}\right)}{\lambda_n\Delta\psi^{t-\Delta t}}\right] - g_1^{t}\left[\frac{1-\exp\left(-\lambda_n\Delta\psi^{t}\right)}{\lambda_n\Delta\psi^{t}}\right]\right\}\overline{S}_{ij}^{t-\Delta t}
\end{aligned} \tag{3.33}$$

$$\begin{aligned}\Delta\varepsilon_{kk}^{nve,t} &= \varepsilon_{kk}^{nve,t} - \varepsilon_{kk}^{nve,t-\Delta t} \\ &= \overline{B}^{t}\overline{\sigma}_{kk}^{t} - \overline{B}^{t-\Delta t}\overline{\sigma}_{kk}^{t-\Delta t} - \frac{1}{3}\sum_{n=1}^{N}\overline{B}_n\left[g_1^t\exp\left(-\lambda_n\Delta\psi^t\right) - g_1^{t-\Delta t}\right]q_{kk,n}^{t-\Delta t} \\ &\quad -\frac{1}{3}g_2^{t-\Delta t}\sum_{n=1}^{N}\overline{B}_n\left\{g_1^{t-\Delta t}\left[\frac{1-\exp\left(-\lambda_n\Delta\psi^{t-\Delta t}\right)}{\lambda_n\Delta\psi^{t-\Delta t}}\right] - g_1^{t}\left[\frac{1-\exp\left(-\lambda_n\Delta\psi^{t}\right)}{\lambda_n\Delta\psi^{t}}\right]\right\}\overline{\sigma}_{kk}^{t-\Delta t}\end{aligned} \tag{3.34}$$

The hereditary integrals at the previous time step (i.e., $q_{ij,n}^{t-\Delta t}$ and $q_{kk,n}^{t-\Delta t}$) can be applied to obtain the hereditary integrals at the end of the increment (i.e., $q_{ij,n}^{t}$ and $q_{kk,n}^{t}$), which are expressed as [6]:

$$q_{ij,n}^{t} = \exp\left(-\lambda_n\Delta\psi^t\right)q_{ij,n}^{t-\Delta t} + \left(g_2^t\overline{S}_{ij}^{t} - g_2^{t-\Delta t}\overline{S}_{ij}^{t-\Delta t}\right)\frac{1-\exp\left(-\lambda_n\Delta\psi^t\right)}{\lambda_n\Delta\psi^t} \tag{3.35}$$

$$q_{kk,n}^{t} = \exp\left(-\lambda_n\Delta\psi^t\right)q_{kk,n}^{t-\Delta t} + \left(g_2^t\overline{\sigma}_{kk}^{t} - g_2^{t-\Delta t}\overline{\sigma}_{kk}^{t-\Delta t}\right)\frac{1-\exp\left(-\lambda_n\Delta\psi^t\right)}{\lambda_n\Delta\psi^t} \tag{3.36}$$

The increment of the viscoplastic strain in Eq. (3.13) can be expressed as:

$$\Delta\varepsilon_{ij}^{vp,t} = \Gamma^{vp}\left\langle\Phi\left(f\right)\right\rangle\frac{\partial g}{\partial\overline{\sigma}_{ij}}\Delta t \tag{3.37}$$

where $\Delta t\Gamma^{vp}\left\langle\Phi\left(f\right)\right\rangle$ can be defined as the viscoplastic multiplier $\Delta\gamma^{vp,t}$ and is presented as

$$\Delta\gamma^{vp,t} = \Delta t\Gamma^{vp}\left\langle\Phi\left(f\right)\right\rangle = \Delta t\Gamma^{vp}\left[\frac{f\left(\overline{\sigma}_{ij}^{t},\varepsilon_e^{vp,t}\right)}{\sigma_y^0}\right]^N \tag{3.38}$$

Substituting Eqs. (3.37) and (3.38) into Eq. (3.20) gives the effective viscoplastic strain increment, which is rewritten as:

$$\Delta\varepsilon_e^{vp,t} = \frac{\Delta\gamma^{vp,t}}{\sqrt{1+2\left(\dfrac{0.5+\beta/3}{1-\beta/3}\right)^2}}\sqrt{\frac{\partial g}{\partial\bar{\sigma}_{ij}}\frac{\partial g}{\partial\bar{\sigma}_{ij}}} \tag{3.39}$$

At the beginning of the coupled nonlinear viscoelastic and viscoplastic implementation, the deviatoric and volumetric increments of the trial stress can be presented as [7]:

$$\Delta\bar{S}_{ij}^{t,tr} = \frac{1}{\bar{J}^{t,tr}}\left\{\Delta e_{ij}^{t} + \frac{1}{2}g_1^{t,tr}\sum_{n=1}^{N}\bar{J}_n\left[\exp\left(-\lambda_n\Delta\psi^t\right)-1\right]q_{ij,n}^{t-\Delta t}\right\} \tag{3.40}$$

$$\Delta\bar{\sigma}_{kk}^{t,tr} = \frac{1}{\bar{B}^{t,tr}}\left\{\Delta\varepsilon_{kk}^{t} + \frac{1}{3}g_1^{t,tr}\sum_{n=1}^{N}\bar{B}_n\left[\exp\left(-\lambda_n\Delta\psi^t\right)-1\right]q_{kk,n}^{t-\Delta t}\right\} \tag{3.41}$$

A dynamic (rate-dependent) yield surface function χ can be defined from Eqs. (3.13), (3.15), and (3.16) as a consistency condition for rate-dependent plasticity (viscoplasticity) and is expressed as:

$$\chi = \bar{\tau} - \alpha\bar{I}_1 - \kappa\left(\varepsilon_e^{vp}\right) - \sigma_y^0\left(\frac{\dot{\gamma}^{vp}}{\Gamma^{vp}}\right)^{1/N} \le 0 \tag{3.42}$$

where χ satisfies the Kuhn-Tucker loading-unloading conditions:

$$\chi \le 0; \quad \dot{\gamma}^{vp} \ge 0; \quad \dot{\gamma}^{vp}\chi = 0; \quad \dot{\chi} = 0 \tag{3.43}$$

One can define a trial dynamic yield surface function from Eq. (43) as

$$\chi = \bar{\tau}^{tr} - \alpha\bar{I}_1^{tr} - \kappa\left(\varepsilon_e^{vp,t-\Delta t}\right) - \sigma_y^0\left(\frac{\Delta\gamma^{vp,t-\Delta t}}{\Delta t\Gamma^{vp}}\right)^{1/N} \tag{3.44}$$

In order to calculate $\varepsilon_e^{vp,t}$ in Eq. (3.44), it is necessary to calculate iteratively $\Delta\gamma^{vp,t}$ by the Newton-Raphson scheme. Once $\Delta\gamma^{vp,t}$ is obtained, $\Delta\varepsilon^{vp,t}$ can be calculated from Eq.

(3.37). To use the local Newton-Raphson scheme, $\partial\chi/\partial\Delta\gamma^{vp}$ is required and expressed as:

$$\frac{\partial\chi}{\partial\Delta\gamma^{vp}} = -\frac{\partial\kappa}{\partial\Delta\varepsilon_e^{vp}}\frac{\partial\Delta\varepsilon_e^{vp}}{\partial\Delta\gamma^{vp}} - \frac{\sigma_y^0}{\Delta\gamma^{vp}N}\left(\frac{\Delta\gamma^{vp}}{\Delta t\Gamma^{vp}}\right)^{1/N} \tag{3.45}$$

The viscoplastic multiplier at the (k+1) iteration is then calculated by

$$\left(\Delta\gamma^{vp,t}\right)^{k+1} = \left(\Delta\gamma^{vp,t}\right)^{k} - \left[\left(\frac{\partial\chi}{\partial\Delta\gamma^{vp,t}}\right)^{k}\right]^{-1}\chi^{k} \tag{3.46}$$

The current effective stress is obtained by the recursive-iterative algorithm with the local Newton-Raphson scheme and the updated values of the nonlinear viscoelastic and viscoplastic strain increments are calculated by the minimizing the residual total strain, defined as:

$$R_{ij}^{t} = \Delta\varepsilon_{ij}^{nve,t} + \Delta\varepsilon_{ij}^{vp,t} - \Delta\varepsilon_{ij}^{t} \tag{3.47}$$

The effective (undamaged) stress increment at the (k+1) iteration is calculated by

$$\left(\Delta\bar{\sigma}_{ij}^{t}\right)^{k+1} = \left(\Delta\bar{\sigma}_{ij}^{t}\right)^{k} - \left[\left(\frac{\partial R_{ij}^{t}}{\partial\bar{\sigma}_{kl}^{t}}\right)^{k}\right]^{-1}\left(R_{kl}^{t}\right)^{k} \tag{3.48}$$

where $\partial R_{ij}^{t}/\partial\bar{\sigma}_{kl}$ gives the consistent tangent compliance needed for speeding convergence and can be expressed as:

$$\frac{\partial R_{ij}^{t}}{\partial\bar{\sigma}_{kl}} = \frac{\partial\Delta\varepsilon_{ij}^{nve,t}}{\partial\bar{\sigma}_{kl}} + \frac{\partial\Delta\varepsilon_{ij}^{vp,t}}{\partial\bar{\sigma}_{kl}} \tag{3.49}$$

where $\partial\Delta\varepsilon_{ij}^{nve,t}/\partial\bar{\sigma}_{kl}$ is the nonlinear viscoelastic tangent compliance derived in Huang et al. [7]. On the other hand, the viscoplastic tangent compliance $\partial\Delta\varepsilon_{ij}^{vp,t}/\partial\bar{\sigma}_{kl}$ is derived from Eqs. (3.37), (3.38), and (3.16), and can be presented as:

$$\begin{aligned}\frac{\partial\Delta\varepsilon_{ij}^{vp,t}}{\partial\bar{\sigma}_{kl}} &= \frac{\partial g}{\partial\bar{\sigma}_{ij}}\frac{\partial\Delta\gamma^{vp,t}}{\partial\bar{\sigma}_{kl}} + \Delta\gamma^{vp,t}\frac{\partial^2 g}{\partial\bar{\sigma}_{ij}\partial\bar{\sigma}_{kl}} \\ &= \frac{\Delta t\Gamma N}{\sigma_y^0}\left(\frac{f}{\sigma_y^0}\right)^{N-1}\frac{\partial g}{\partial\bar{\sigma}_{ij}}\frac{\partial f}{\partial\bar{\sigma}_{kl}} + \Delta t\Gamma\left(\frac{f}{\sigma_y^0}\right)^{N}\frac{\partial^2 g}{\partial\bar{\sigma}_{ij}\partial\bar{\sigma}_{kl}}\end{aligned} \tag{3.50}$$

where $\partial^2 g/\partial\bar{\sigma}_{ij}\bar{\sigma}_{kl}$ is given by:

$$\begin{aligned}\frac{\partial^2 g}{\partial\bar{\sigma}_{ij}\bar{\sigma}_{kl}} &= \frac{3}{2}\left(\delta_{ik}\delta_{jl} - \frac{1}{3}\delta_{ij}\delta_{kl}\right)\left[\frac{1+1/d}{2\sqrt{\bar{J}_2}} - \frac{\bar{J}_3\left(1-1/d\right)}{\bar{J}_2^2}\right] \\ &+ \frac{3}{2}\left[\frac{-\dfrac{\partial\bar{J}_2}{\partial\bar{\sigma}_{ij}}\left(1+1/d\right)}{4\sqrt{\bar{J}_2^3}} + \left(1-1/d\right)\left(\frac{2\bar{J}_3}{\bar{J}_2^3}\frac{\partial\bar{J}_2}{\partial\bar{\sigma}_{ij}} - \frac{1}{\bar{J}_2^2}\frac{\partial\bar{J}_3}{\partial\bar{\sigma}_{ij}}\right)\right]\bar{S}_{kl} \\ &+ \frac{\left(1-1/d\right)}{2\bar{J}_2^2}\left[\frac{27\left(\delta_{ik}\bar{S}_{lj} + \delta_{jl}\bar{S}_{ik}\right)}{2} - 9\left(\delta_{kl}\bar{S}_{ij} + \delta_{ij}\bar{S}_{kl}\right)\right] \\ &- \frac{3}{2}\left(\frac{9\bar{S}_{km}\bar{S}_{ml}}{2} - \bar{J}_2\bar{S}_{kl}\right)\left[\frac{\left(1-1/d\right)\dfrac{\partial\bar{J}_2}{\partial\bar{\sigma}_{ij}}}{\bar{J}_2^2}\right]\end{aligned} \tag{3.51}$$

A flow chart for the brief procedure is illustrated in Figure III-1. See Darabi et al. [24] for the flowchart for the whole implementation. The aforementioned numerical algorithm is implemented in the well-known commercial finite element software Abaqus [11] via the user material subroutine (UMAT) and is used in the following to conduct the

finite element simulations. The detail procedure to identify the material parameters for this model will be described in chapter VI.

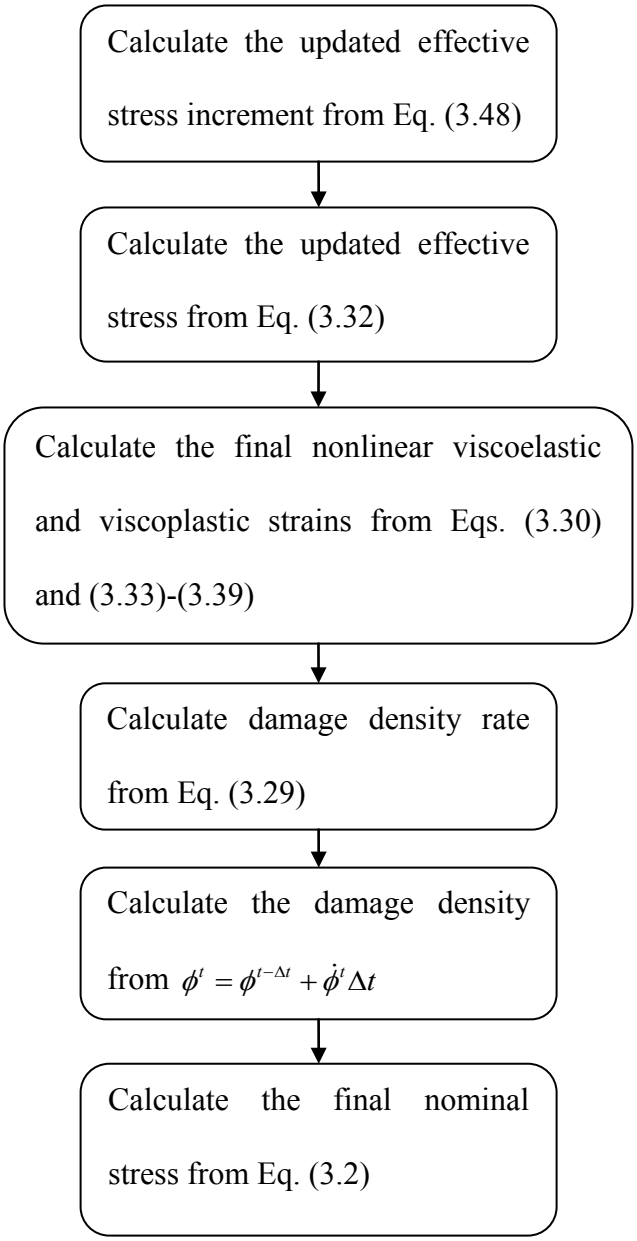

Figure III-1. The flow chart for the brief procedure.

III.7 Conclusions

The thermo-viscoelastic, thermo-viscoplastic, and thermo-viscodamage constitutive model presented in this chapter has many capabilities that make it applicable to describing the time-, rate-, and temperature dependent behavior of asphalt concrete. The model couples damage with the viscoelastic and viscoplastic responses. In addition, a unique feature of this model is the ability to select using some components of it depending on the prevailing conditions. For example, one can choose to use the damage viscoelastic response for modeling the fatigue behavior at low or intermediate temperature at which permanent deformation might be negligible.

The model is implemented numerically in the finite element package Abaqus. As such, it can be readily used to describe the response of asphalt mixture under various multi-axial stress histories and boundary conditions. This constitutive model is used to predict the response of the mixture matrix of FAM using a variety of 2D and 3D microstructures in this dissertation.

CHAPTER IV

2D MICROMECHANICAL MODELING OF ASPHALT CONCRETE*

IV.1 Introduction

In this chapter, 2D microstructural finite element computational modeling of asphalt concrete using RVE is conducted in order to obtain the overall macroscopic thermo-mechanical response of asphaltic concrete in terms of key microstructural features such as aggregate shape, distribution, volume fraction, and ITZ strength. Moreover, the simulations are conducted under different loading conditions such as uniaxial tension, compression, and cyclic loading up to failure. The effects of strain rate and temperature on the evolution of micro-damage patters are also investigated. This is achieved through employing a thermodynamic-based constitutive model described in chapter III.

This chapter also includes the work on the development of RVEs based on images by X-ray computer tomography of asphalt concrete specimen and used to investigate the effects of strain rate and temperature on the stress-strain and repeated creep-recovery behaviors up to complete fracture. It is noted that the text, figures, and tables in this chapter had been published in Abu Al-Rub et al. [50].

IV.2 Parametric Study with Various Asphalt Concrete Microstructural Morphology

In order to investigate the effects of the change in aggregate shapes, distribution, volume fraction, strength of the ITZ, a detailed parametric study is performed. The commercial finite element analysis software Abaqus [11] is used along with the coded utility subroutine UMAT. A 4-node bilinear plane strain quadrilateral element (CPE4) is used in the simulations. As shown in Figure IV-1, the 100 mm×100 mm RVE is simulated as a 2D plane strain meso-scale asphalt concrete model. The size of the RVE is based on detailed studies by Dessouky et al. [33] and Kim et al. [3] who investigated the proper size for the RVE for asphalt concrete using spatial distribution of the microstructure and multiscale modeling, respectively. Different and more realistic microstructural morphologies other than that shown in Figure 1 are also generated and will be described subsequently. The modulus of elasticity and Poisson's ratio for aggregates used here are 25 GPa and 0.25, respectively, [33]. The material parameters associated with the thermo-viscoelastic, thermo-viscoplastic, and the thermo-viscodamage constitutive equations are summarized in Table IV-1. The mastic (binder with fine particles) is assumed to be incompressible with a Poisson's ratio of 0.49. These parameters have been identified by Abu Al-Rub et al. [56] for viscoelasticity and viscoplasticity and by Darabi et al. [23] for viscodamage for a specific type of asphalt concrete. These material parameters are adapted to describe the typical thermo-mechanical response of asphalt concrete.

The focus of this study is on the influence of the material parameters listed in Table IV-1 and the influence of different microstructural parameters and loading conditions on the overall thermo-mechanical response of asphalt mixtures. For the simulations

conducted in this section, a temperature of 20°C and a tensile strain rate of 5×10^{-4}/ second are considered. Therefore, the conclusions inferred from the simulations in this section are only valid for these loading conditions. More realistic case scenarios are considered in Section IV.3.

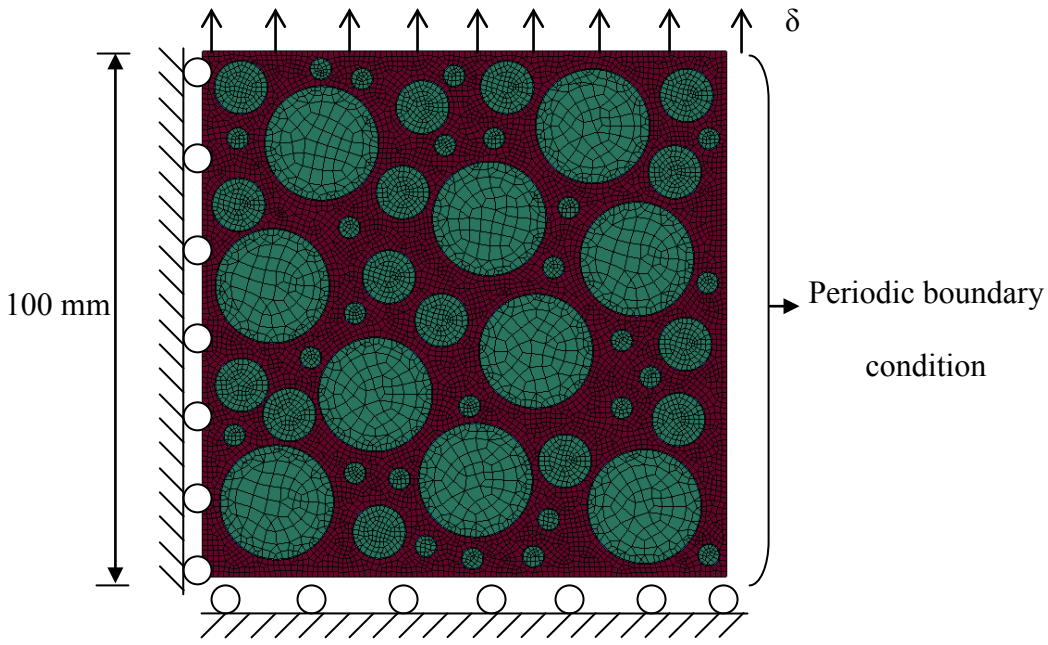

Figure IV-1. The 2-D microstructure asphalt concrete model with 50% aggregate volume fraction showing the dimensions, boundary conditions, loading, and finite element mesh.

Table IV-1. List of material parameters at T=20 °C [23].

Viscoelastic model parameters						
n		λ_n (Sec^{-1})		D_n (MPa^{-1})	D_0 (MPa^{-1})	
1		10		1.98×10^{-4}		
2		1		1.48×10^{-3}		
3		0.1		6.56×10^{-4}	3.5×10^{-3}	
4		0.01		1.43×10^{-3}		
5		0.001		2.47×10^{-3}		
Viscoplastic model parameters						
α	β	Γ_0^{vp} (Sec^{-1})	N	k_0 (kPa)	k_1 (kPa)	k_2
0.3	0.15	5×10^{-4}	3.63	35	610	215
Nonlinear viscoelastic parameter						
a_T		g_0		g_1		g_2
1.0		1		1.194		0.837
Viscodamage model parameter						
Γ_0^{φ} (Sec^{-1})		Y_0 (kPa)		q		k
4×10^{-5}		700		5		30

IV.2.1 The Effect of Aggregate Shape

In order to investigate the effect of aggregate shape, several RVEs with five different aggregate shapes are created: tetragonal, pentagonal, hexagonal, circular, and irregular aggregate shapes (see Figure IV-2). The irregular aggregate shape used in this analysis is described in Masad et al. [57]. The areas of aggregates (coarse, middle, and fine) with different aggregate shapes (except the irregular aggregate shape) are kept the same (i.e., for example, the area of a middle size tetragonal aggregate is equal to the area of a

middle size circular aggregate). The aggregate volume fraction in all RVEs in Figure IV-2 is 50%.

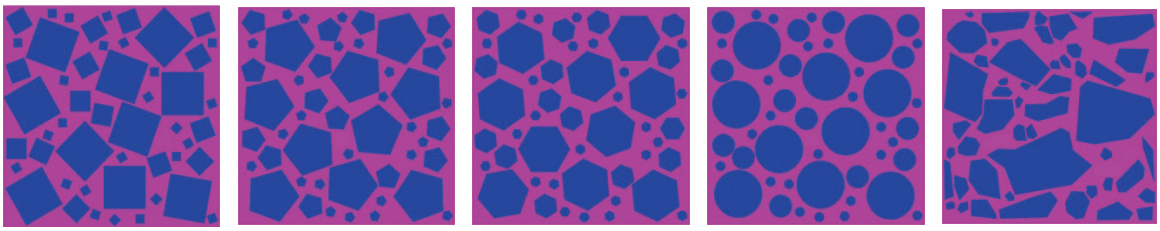

(a) (b) (c) (d) (e)

Figure IV-2. Asphalt concrete RVEs with different aggregate shapes: (a) tetragonal, (b) pentagonal, (c) hexagonal, (d) circular, and (e) irregular. Aggregate volume fraction is 50%.

The stress-strain responses for the RVEs in Figure IV-2 are shown in Figure IV-3, and the damage density distributions at different strain levels for the all aggregate shapes are shown in Figure IV-4 to Figure IV-8. These figures show that aggregate shape has some influence, but not significant, on the ultimate strength, damage initiation, and propagation. Figure IV-3 shows that tetragonal aggregate shape results in the largest ultimate strength, but comparable ultimate strengths are obtained for the others. Moreover, one can see from Figure IV-4 to Figure IV-8 that there is little difference among the damage density distributions at different strain levels, especially at failure. The relatively small influence of aggregate shape on strength and damage is attributed to the fact that the simulations are conducted under tensile stresses. It is known that the influence of aggregate shape on asphalt concrete response is more evident under compressive loading stresses [18]. Therefore, in tension using different aggregate shapes

by fixing their distribution does not affect the overall mechanical response significantly. Therefore, the focus of the next section is on investigating the influence of aggregate distribution which seems to be the key for controlling the mechanical behavior of asphaltic mixtures under extension loading conditions.

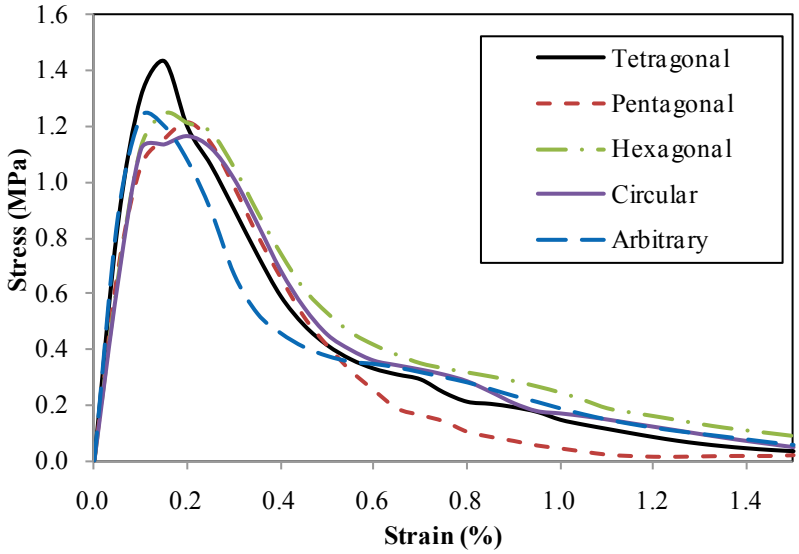

Figure IV-3. Stress-strain diagrams for asphalt concrete models with various aggregate shapes.

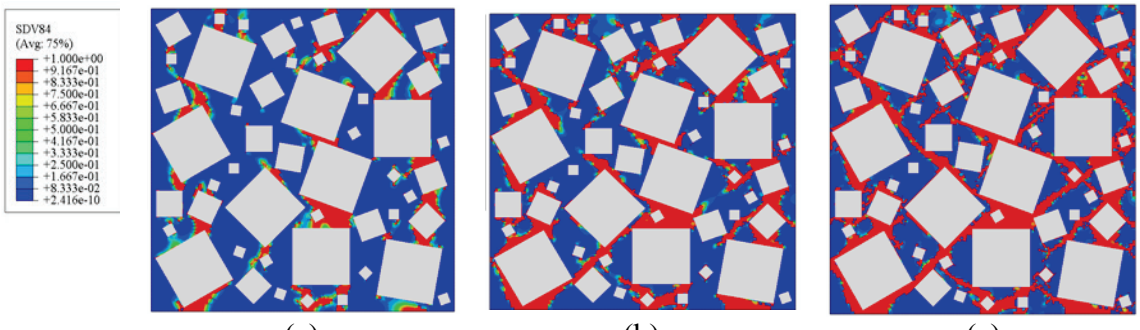

(a) (b) (c)

Figure IV-4. Damage density distribution of asphalt concrete model with tetragonal aggregate shape at: (a) strain=0.2%, (b) strain=0.4%, and (c) failure.

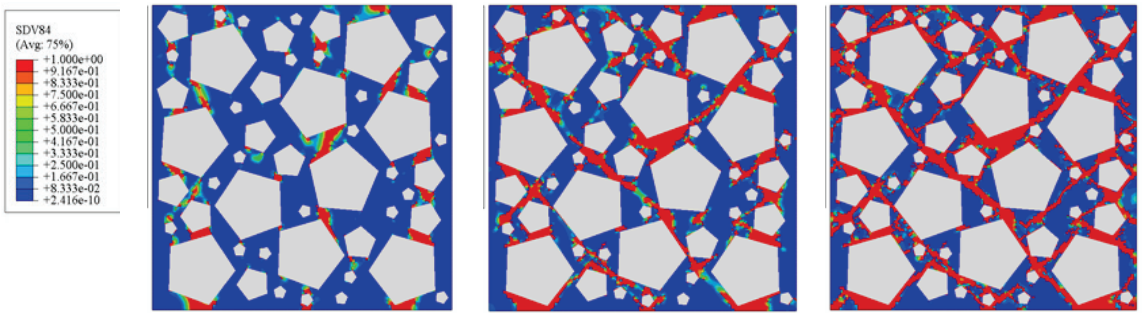

(a) (b) (c)

Figure IV-5. Damage density distribution of asphalt concrete model with pentagonal aggregate shape at: (a) strain=0.2%, (b) strain=0.4%, and (c) failure.

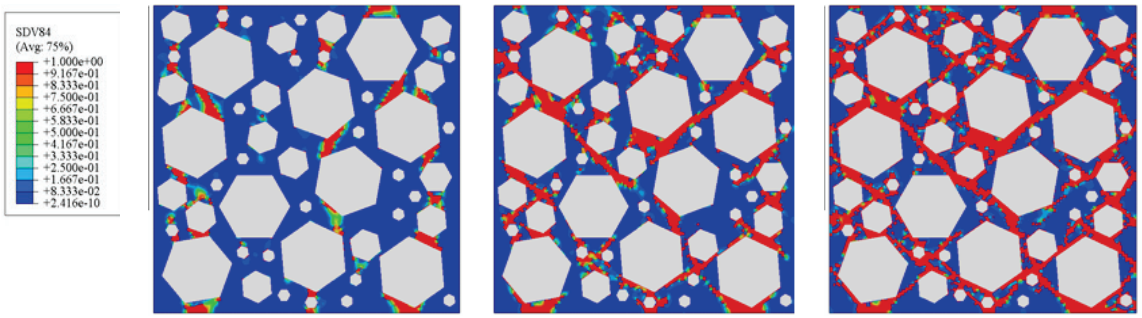

(a) (b) (c)

Figure IV-6. Damage density distribution of asphalt concrete model with hexagonal aggregate shape at: (a) strain=0.2%, (b) strain=0.4%, and (c) failure.

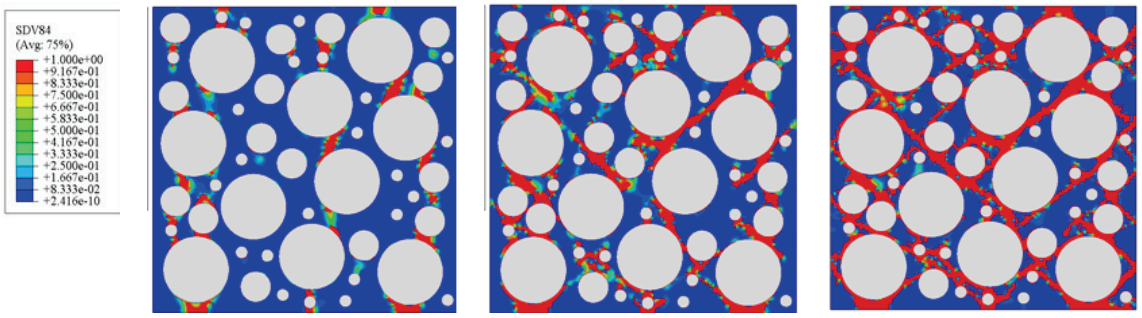

(a) (b) (c)

Figure IV-7. Damage density distribution of asphalt concrete model with circular aggregate shape at: (a) strain=0.2%, (b) strain=0.4%, and (c) failure.

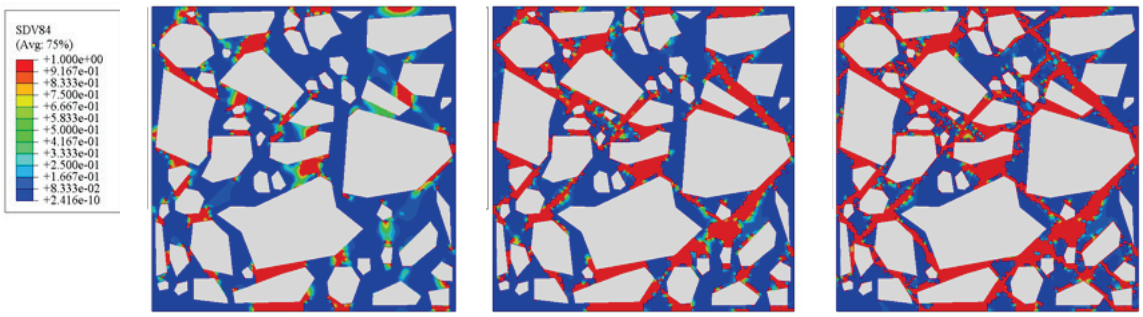

(a) (b) (c)

Figure IV-8. Damage density distribution of asphalt concrete model with arbitrary aggregate shape at: (a) strain=0.2%, (b) strain=0.4%, and (c) failure.

IV.2.2 The Effect of Aggregate Distribution

Four RVEs with different distributions of the irregular aggregate shape are shown in Figure IV-9. The aggregate volume fraction used is 50%. The stress-strain responses of the four RVEs are presented in Figure IV-10, and the corresponding damage density distributions at failure are shown in Figure IV-11. It can be seen from Figure IV-10 and Figure IV-11 that the aggregate distribution strongly affects the stress-strain behavior and damage evolution in asphalt mixtures. The ultimate strengths of distributions II and III are higher than those for distributions I and IV because coarse aggregates in distributions II and III are located in the damage path and prevent damage from propagating. Therefore, damage initiation and propagation under tensile stresses are strongly affected by aggregate distribution as compared to aggregate shape. However, it is noteworthy that aggregate distribution is related to microstructural enhanced anisotropy such that different distributions give rise to different anisotropy and consequently different mechanical behavior. Moreover, the effect of distribution might

be less or more significant depending on the loading conditions (e.g. biaxial, triaxial, shear, etc).

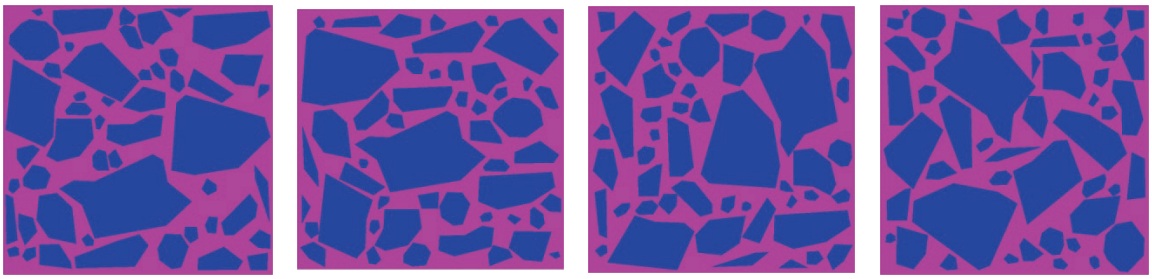

(a) (b) (c) (d)

Figure IV-9. Various asphalt aggregate distribution models (50% aggregate volume fraction): (a) Distribution I, (b) Distribution II, (c) Distribution III, and (d) Distribution IV.

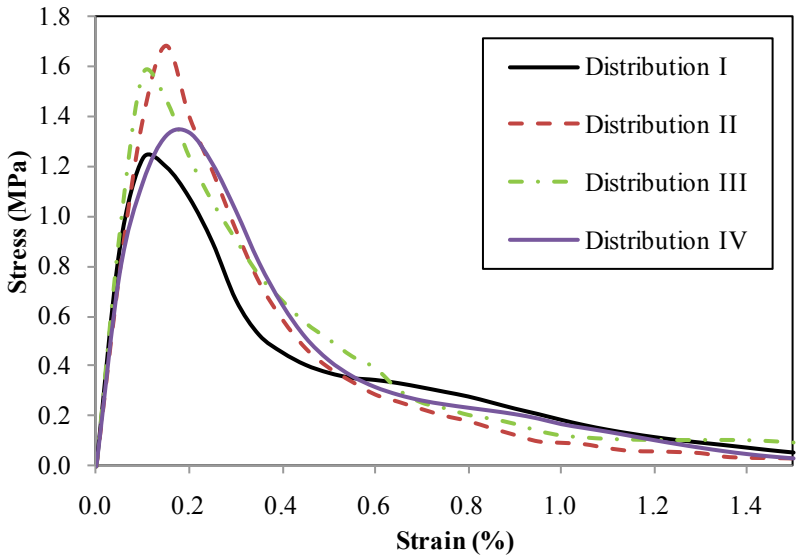

Figure IV-10. Stress-strain diagrams for various aggregate distributions (50% aggregate volume fraction).

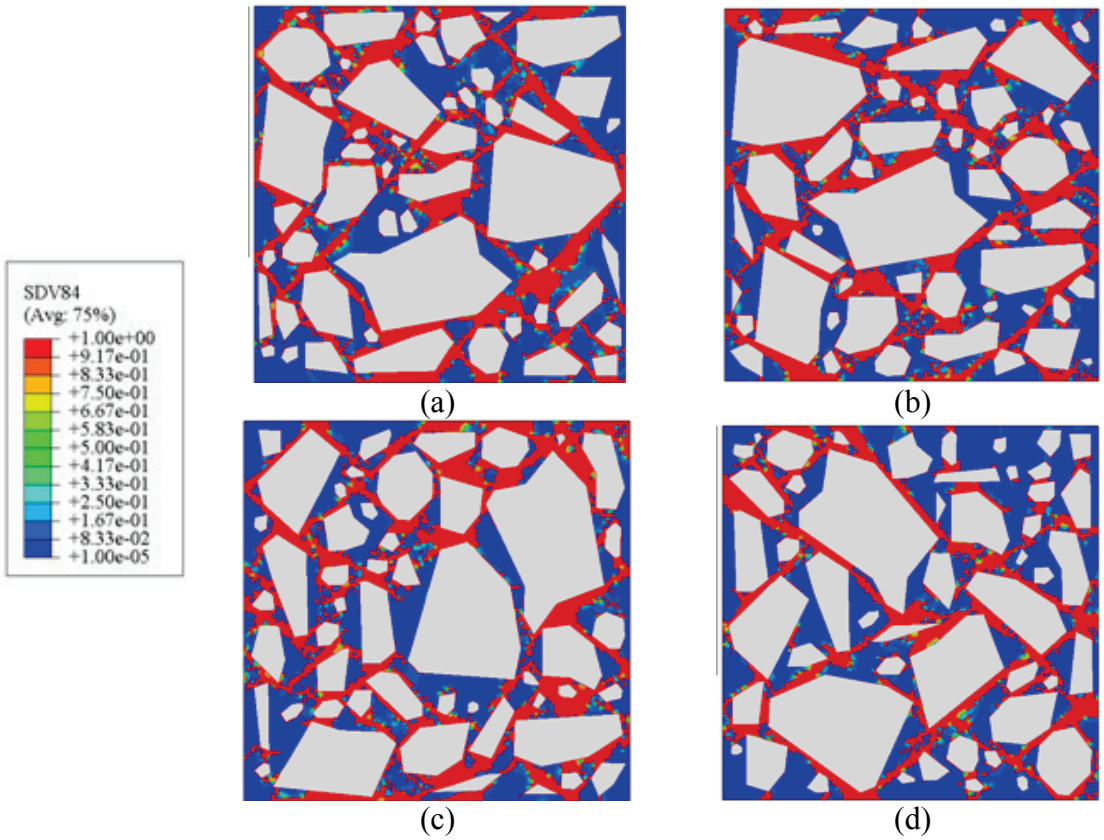

Figure IV-11. Damage density distribution of asphalt concrete models (50% aggregate volume fraction): (a) Distribution I, (b) Distribution II, (c) Distribution III, and (d) Distribution IV.

IV.2.3 The Effect of Aggregate Volume Fraction

Five different aggregate volume fractions are created as shown in Figure IV-12. The stress-strain responses of the five RVEs are shown in Figure IV-13, and the corresponding damage density distributions at failure are shown in Figure IV-14. Although 10% and 20% volume fractions are not realistic for asphalt mixtures, they are included to see the relative effect of the mastic as compared to the asphalt mixture behavior. Note from Figure IV-13 that, as expected, the initial stiffness increases as the

aggregate volume fraction increases. However, there is no clear trend for the increase in the ultimate tensile strength as a function of aggregate volume fraction. This depends on the distribution of the aggregates as concluded from the previous section; different distributions yield different responses. The RVE with the least volume fraction (10%) yields the highest strength and highest strain at failure. This observation indicates that highest ultimate strength at 10% volume fraction may be due to the small amount of discontinuities or stress concentrators at the aggregates' surfaces that trigger damage initiation, whereas the corresponding highest strain to failure can be attributed to higher volume fraction of the mastic which can sustain larger strains. The overall damaged area increases as the aggregate volume fraction increases, but it is more localized in case of smaller volume fractions. Therefore, various aggregate volume fractions influence the damage initiation and propagation differently due to the various aggregate volume fractions that result in different aggregate distributions.

(a) (b) (c) (d) (e)

Figure IV-12. Asphalt concrete RVEs with arbitrary aggregate shape and with various aggregate volume fractions: (a) 10%, (b) 20%, (c) 30%, (d) 40%, and (e) 50%.

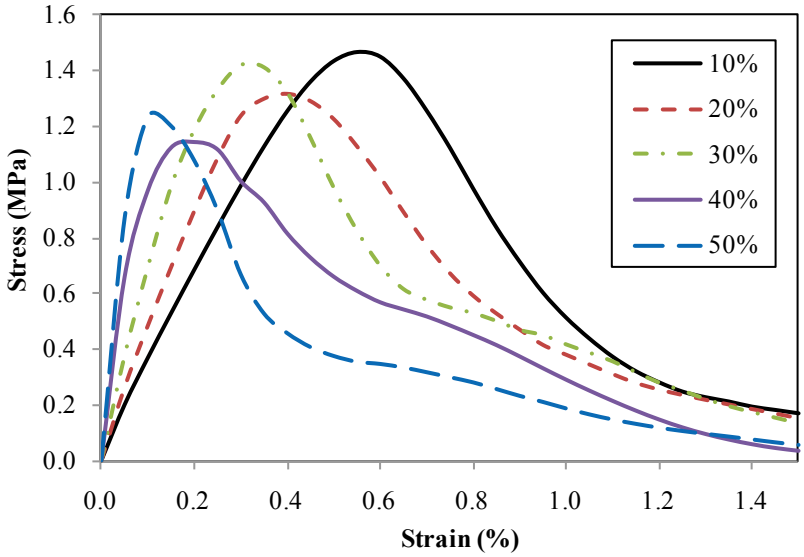

Figure IV-13. Stress-strain diagrams for arbitrary aggregate shape model with various aggregate volume fractions.

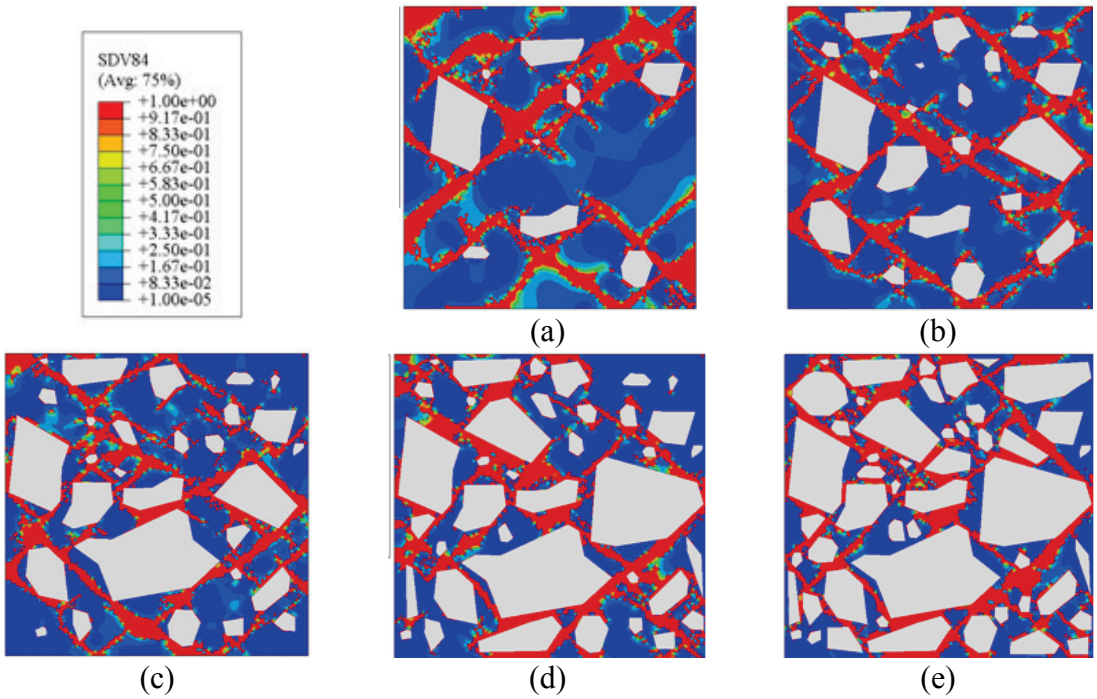

Figure IV-14. Damage density distribution of asphalt concrete models with various volume fractions (arbitrary aggregate shape): (a) 10%, (b) 20%, (c) 30%, (d) 40%, and (e) 50%.

IV.2.4 The Effect of the Strength for ITZ

The ITZ represents the interface between the aggregate and the matrix. The properties of the ITZ depend on many factors such as the surface energy of aggregate and binder, binder wettability, and aggregate texture. Therefore, it is a challenge to identify the characteristics of the ITZ. Such characteristics might be identified by special experimental techniques such as the nanoindentation test, phyio-chemical measurements of surface energy, and measurements of aggregate texture. Here, the ITZ is assumed to have a similar behavior (i.e. viscoelastic, viscoplastic, and viscodamage) to the mastic matrix. However, in order to investigate the effect of the ITZ on the overall mechanical response of the asphalt mixture shown in Figure IV-14 (e), the compliances D_n, listed in Table IV-1, are changed by a constant percentage. The compliances of the ITZ vary from 25% to 200% of the compliances presented in Table IV-1 [see Figure IV-15 (a)]. Compliances less than those of the mastic mean a stronger ITZ, whereas compliances greater than those of the mastic imply a weaker ITZ as compared to the surrounding matrix. The corresponding stress-strain diagrams are shown in Figure IV-15 (b), and the damage density distributions at failure are presented in Figure IV-16. It is obvious that the viscoelastic behavior of the ITZ slightly affects the overall response of the asphalt concrete. As shown in Figure IV-15 (c), the RVE with the lowest compliance has the highest ultimate strength because the model with lower compliance can resist more loading. Moreover, as shown from Figure 16 the damage distribution of the RVEs at failure are very similar. However, variations in other mechanical properties such as

varying the damage parameters for the ITZ may affect the overall response of asphalt concrete.

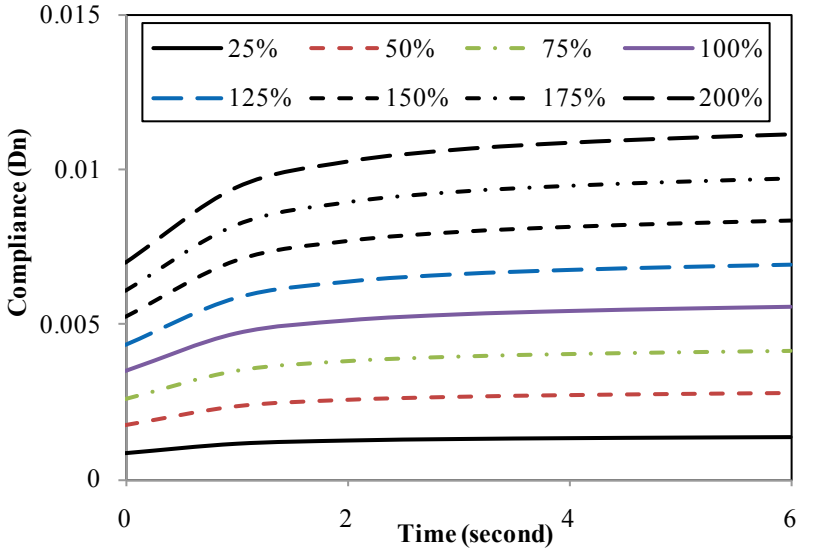

(a)

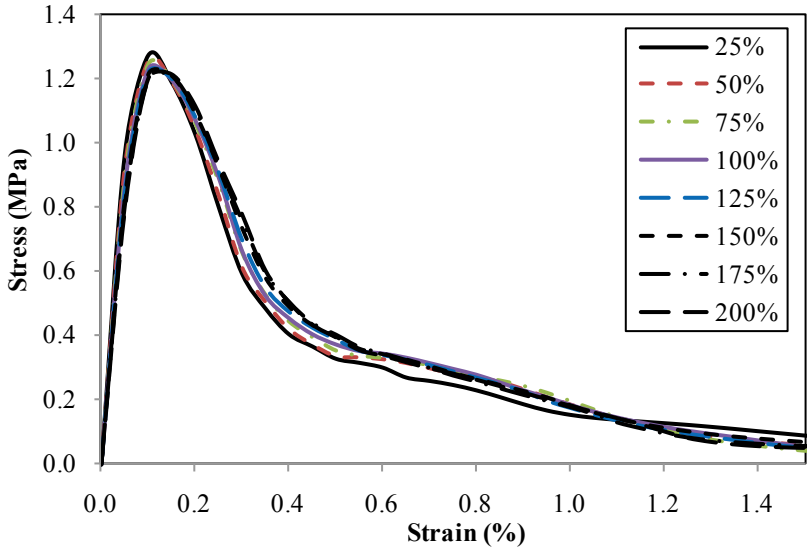

(b)

Figure IV-15. (a) Compliance-time plots for various D_n for ITZ, (b) stress-strain diagrams for various D_n for ITZ, and (c) ultimate strengths for various Dn for ITZ (arbitrary aggregate shape model with 50% aggregate volume fraction).

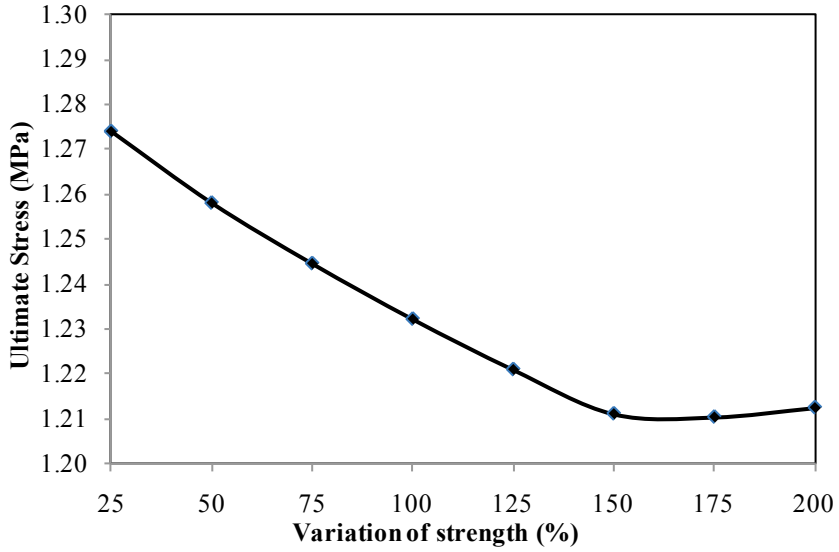

(c)

Figure IV-15 Continued.

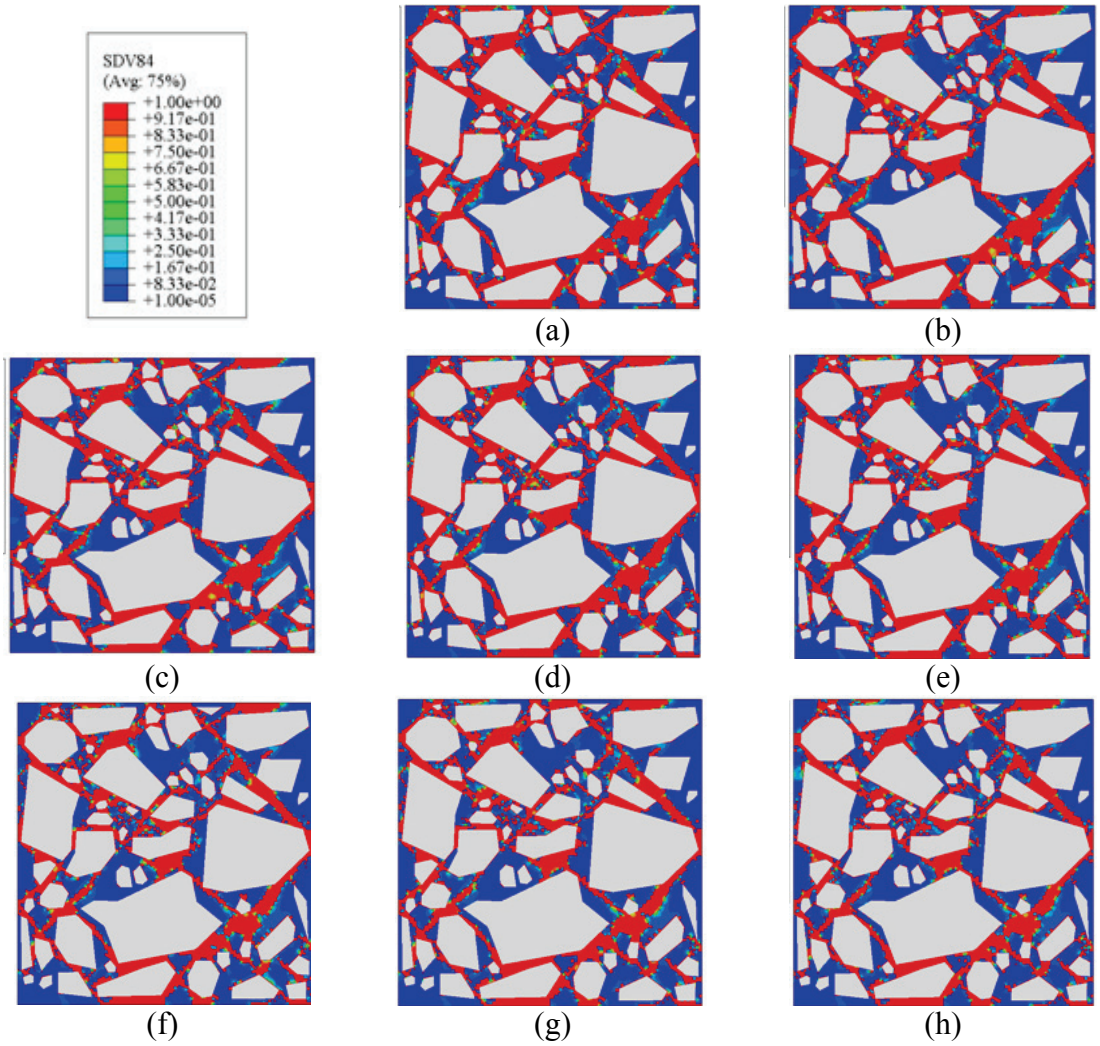

Figure IV-16. Damage density distribution of asphalt concrete models with various D_n for ITZ (50% aggregate volume fraction): (a) 25%, (b) 50%, (c) 75%, (d) 100%, (e) 125%, (f) 150%, (g) 175%, and (h) 200%.

IV.3 2D Image-based Micromechanical Modeling

A more realistic 2D RVE representation of asphalt concrete microstructure is generated by using an X-ray CT image form [57]. This microstructure is used here in order to investigate the effects of loading conditions (tensile, compressive, repeated loading), strain rate, and temperature on the overall mechanical response of asphalt concrete. The RVE has a size of 200 mm × 200 mm as shown in Figure IV-17. The mesh and boundary conditions are shown in Figure IV-17 (c). For simplicity and limited computational cost, very fine aggregates are neglected in the analysis that resulted in Figure IV-17 (b). The aggregate volume fraction of the generated asphalt concrete model is about 50%. This RVE of asphalt concrete had three phases: aggregate, ITZ, and matrix. In this analysis, the ITZ and the mastic are assumed to have the same mechanical properties. The modulus of elasticity and Poisson's ratio for the aggregate are assumed to be 25 GPa and 0.25, respectively [33], whereas those for matrix and ITZ are as listed in Table IV-1 and Table IV-2.

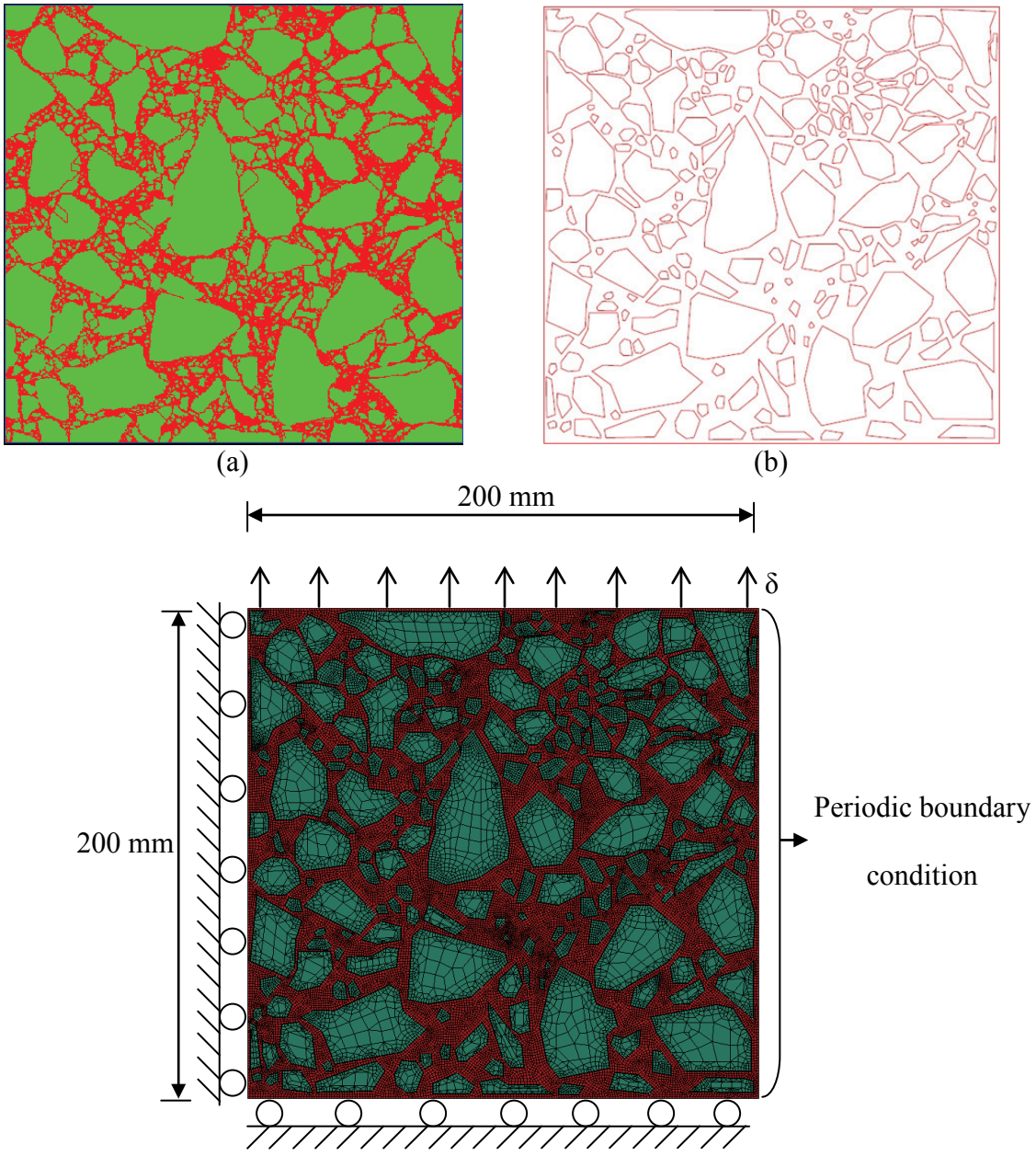

Figure IV-17. (a) X-ray image of an asphalt concrete [57], (b) idealized asphalt concrete, and (c) RVE of asphalt concrete showing geometry, finite element mesh, and boundary conditions.

Table IV-2. Model parameters at various temperatures [23].

	T=10 ºC	*T=20 ºC*	*T=40 ºC*
g_0	0.43	1.0	5.7
g_1	0.908	1.194	0.576
g_2	1.017	0.837	1.920
a_T	7.0	1.0	0.008

IV.3.1 The Effect of Strain Rate

Generally, asphalt concrete is known as a highly rate sensitive material. In order to investigate the effect of strain rate on the mechanical properties of asphalt concrete, four different tensile and compressive strain rates are applied to the RVE as shown in Figure IV-17 (c). The resulting stress-strain diagrams representing tensile and compressive uniaxial behavior are shown in Figure IV-18. The damage density distributions at failure are presented in Figure IV-19 and Figure IV-20 for tensile and compressive loadings, respectively. It is apparent from Figure IV-18 that the constitutive model used in this research can predict the impact of loading rate on the initial stiffness, the ultimate strength, and strain to failure of the material. Furthermore, the model can predict the different behavior of the asphalt mixture when subjected to tensile or compressive modes of loading, where it is noted that the material is stronger in compression. Yielding in tension also starts much earlier than in compression. Furthermore, from Figure IV-19 and Figure IV-20, it is apparent that the damage density increases as the rate of loading increases. However, the damage nucleation and propagation slightly differs between

tensile and compressive modes of loading. The damage distribution is more localized in tension than that in compression.

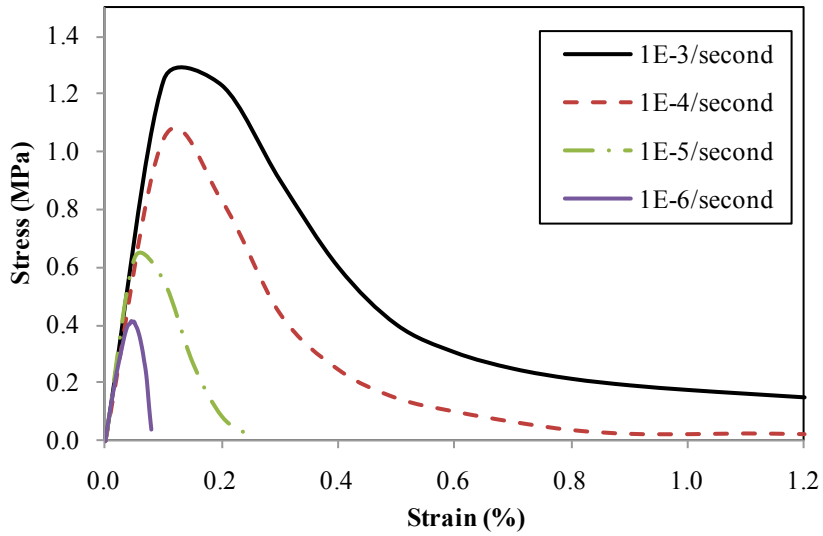

(a)

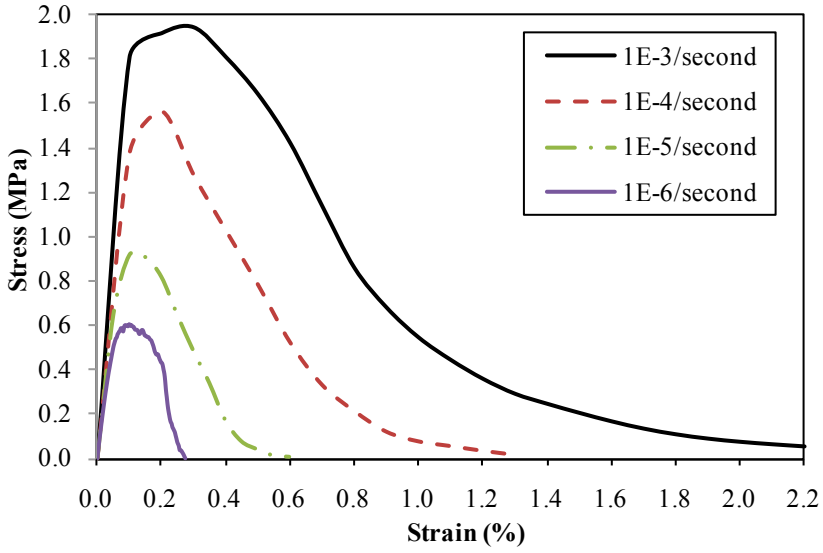

(b)

Figure IV-18. Stress-strain diagrams with different strain rates (50% aggregate volume fraction and T=20 °C): (a) tension and (b) compression.

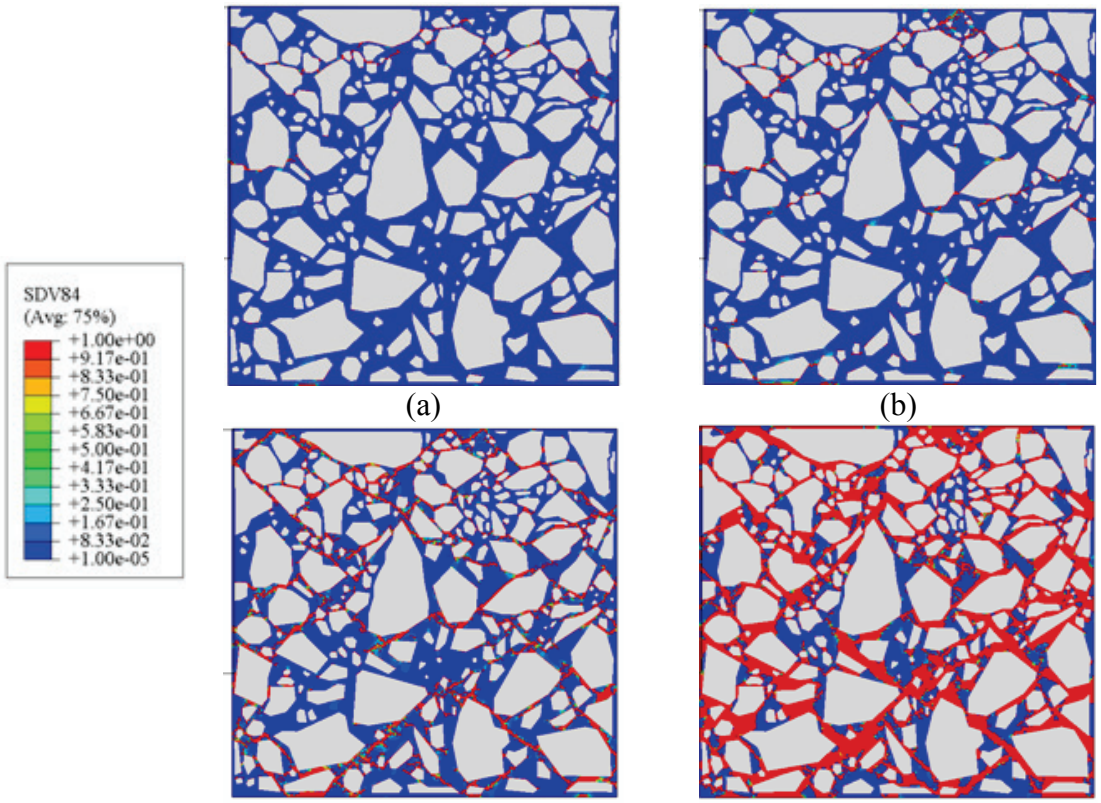

Figure IV-19. Damage density distribution of asphalt concrete models with tensile strain rates (50% aggregate volume fraction and T=20 °C): (a) 10^{-6}/second, (b) 10^{-5}/second, (c) 10^{-4}/second, and (d) 10^{-3}/second.

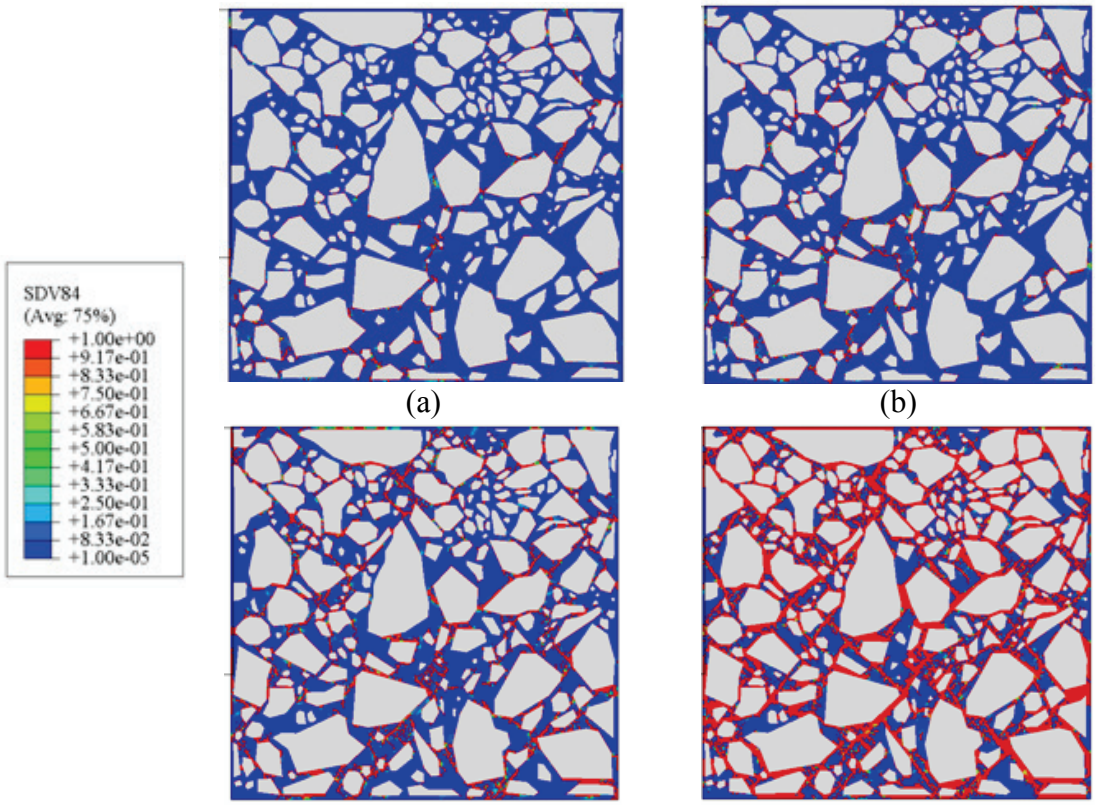

Figure IV-20. Damage density distribution of asphalt concrete models with compressive strain rates (50% aggregate volume fraction and T=20 °C): (a) 10^{-6}/second, (b) 10^{-5}/second, (c) 10^{-4}/second, and (d) 10^{-3}/second.

IV.3.2 The Effect of Temperature

The time and temperature sensitivity of asphalt concrete requires a thorough evaluation of both as well as the convolution of the effects of each. Three temperatures were simulated in the RVE under tension: 10 ºC, 20 ºC, and 40 ºC. The material constants in

Table IV-1 represent those identified at reference temperature (i.e. at 20 ºC), while the temperature-dependent material parameters are summarized in Table IV-2 [see Eqs. (3.3), (3.4), and (3.14)]. The stress-strain responses at the three temperatures are shown in Figure IV-21, and the corresponding damage density distributions at 0.2% strain are presented in Figure IV-22. One can note the strong dependence of the overall mechanical response of asphalt concrete on temperature in Figure IV-21, where weaker responses are obtained as temperature increases. The asphalt concrete RVE subjected to higher temperatures has a much lower ultimate strength. Moreover, at specific strain level, damage increases as temperature decreases, as shown in Figure IV-22. This is because the material becomes more brittle and more prone to more damage as temperature decreases.

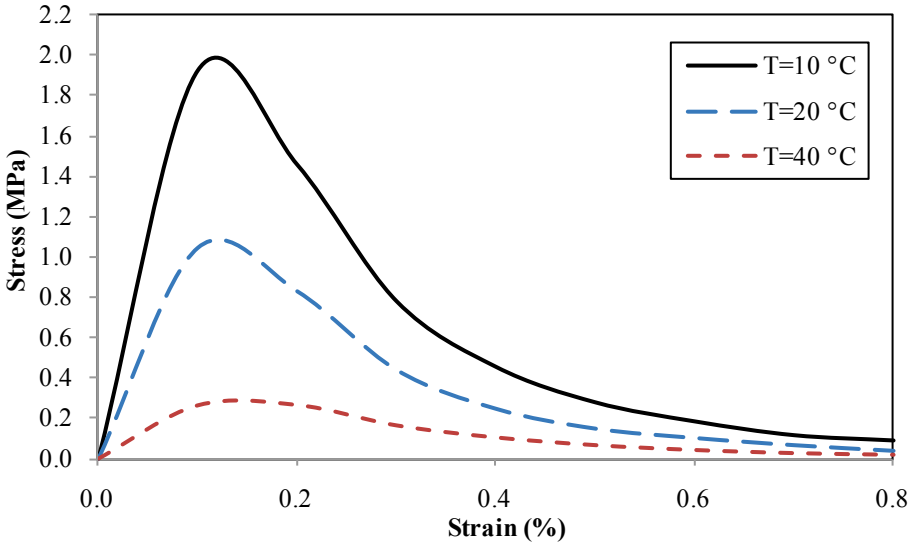

Figure IV-21. Stress-strain diagram with different temperatures and tensile strain rate 10^{-4}/second (50% aggregate volume fraction).

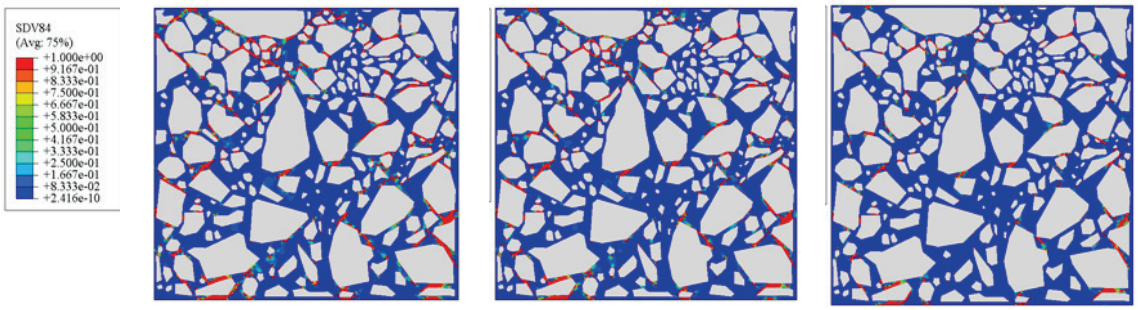

(a) (b) (c)

Figure IV-22. Damage density distribution of asphalt concrete models with various temperatures at 0.2% strain (50% aggregate volume fraction and tensile strain rate 10^{-4}/second): (a) T=10 °C, (b) T=20 °C, and (c) T=40 °C.

IV.3.3 The Effect of Loading Type

Generally, asphalt concrete mixtures are subjected to cyclic traffic loading. Therefore, in order to investigate the continuous loading and unloading that occurs during trafficking of pavements, a repeated compressive creep-recovery test was simulated at temperature of 20 ºC. The creep-recovery loading is shown in Figure IV-23 (a). The loading duration for creep and recovery were 100 and 50 seconds, respectively. The corresponding strain-time response and damage density distribution at different loading cycles are shown in Figure IV-23 (b) and Figure IV-24, respectively. Figure IV-23 (b) shows the development of primary, secondary, and tertiary creep and failure. The progression of damage evolution with increasing loading-unloading cycles is shown in Figure IV-24, where it is shown that damage density increases with the number of loading cycles. In addition, the level of strain at failure of the RVE under repeated loading is less for a similar magnitude of load but applied at a constant loading rate, which means that the capacity of asphalt concrete can be overestimated by the constant loading test.

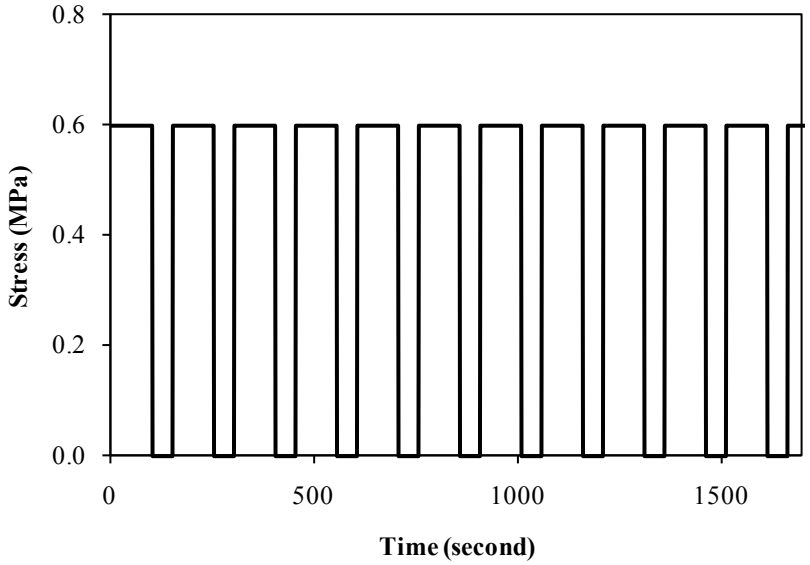

(a)

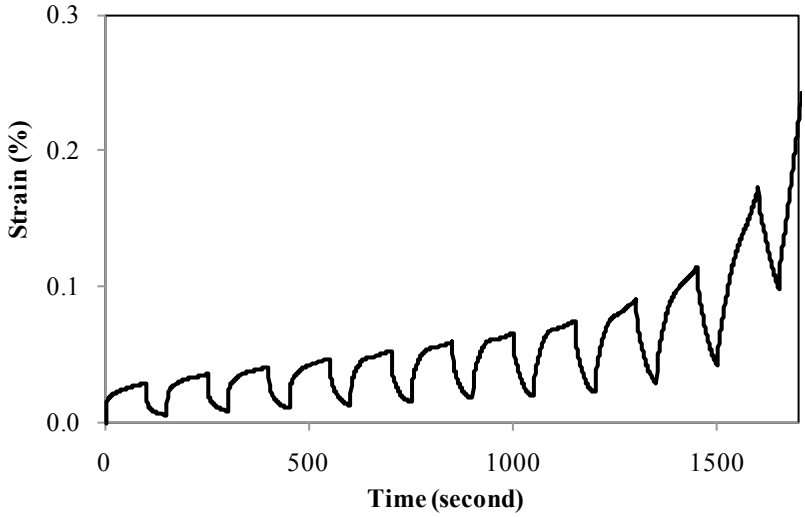

(b)

Figure IV-23. Repeated creep-recovery compressive test for T=20 °C: (a) stress-time diagram and (b) strain-time diagram.

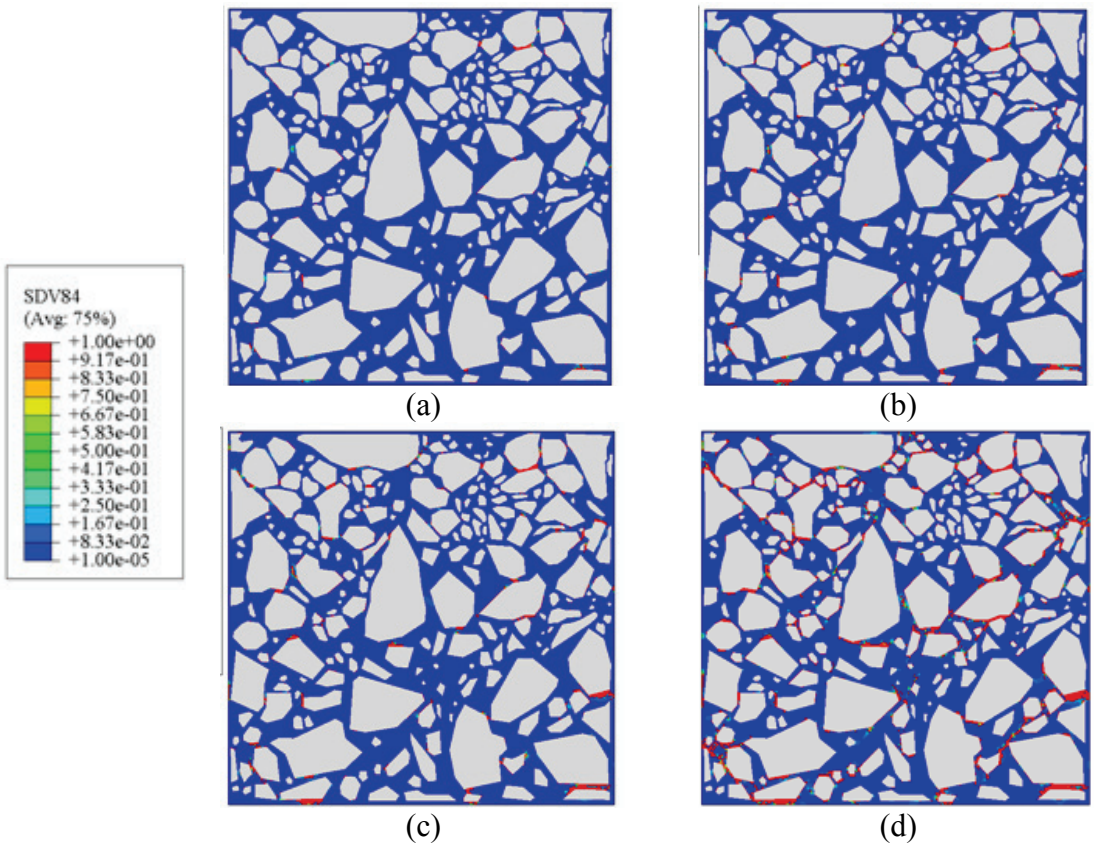

Figure IV-24. Damage density distribution of repeated creep-recovery compressive test for T=20 °C at: (a) 400 seconds, (b) 800 seconds, (c) 1200 seconds, and (d) failure.

IV.4 Conclusions

The effects of aggregate shape, aggregate distribution, aggregate volume fraction, the strength of the ITZ, strain rate, and temperature are important to consider when modeling the behavior of asphalt mixtures. For the first time a comprehensive coupled thermo-viscoelastic, thermo-viscoplastic, and thermo-viscodamage model was used to help determine the impact of these important variables using the image-based 2D finite element microstructures. The microstructures have three phases: aggregate, matrix (i.e., binder with fine aggregates), and the ITZ. The matrix and the ITZ were considered as

thermo-viscoelastic, thermo-viscoplastic, and thermo-viscodamaged materials while the aggregate is considered an elastic material. Based on the case scenarios simulated in this chapter, the following conclusions are inferred:

- The current constitutive model and 2D computational framework allows one to easily investigate the effects of different microstructural morphologies and different loading conditions on the behavior of asphalt concrete. The proposed framework is computationally stable and robust. The current computational framework can be easily used in guiding the design of microstructures in asphalt mixtures. The 2D microstructures can be improved by proper selection of mixture constituents and by developing improved volumetrics through good mixture design practices. The constitutive model becomes a tool to assist in this effort.
- It was found that the aggregate shape has a slight effect on the overall mechanical response of asphalt concrete under tensile loading conditions.
- Aggregates distribution has a significant effect on the mechanical response of asphalt mixture because of the significant difference in damage nucleation sites and damage propagation.
- An increase in aggregate volume fraction makes the mixture less ductile. The implemented model successfully incorporates the strong effects of strain rate and temperature of the thermo-mechanical response of asphalt concrete mixtures. Moreover, the model can distinguish between the asphalt concrete behavior in compression and extension loading conditions.

- The strength and brittleness of asphalt concrete increases as temperatures decreases which impacts the nature of distress and damage evolution that occurs in asphalt mixtures at different ends of the temperature spectrum. This is obviously well known, but it is important to note the sensitivity of this model to the impact of temperature.
- The model presented in this chapter can predict the different stages of creep and recovery up to the point of failure. The model described in this chapter has considerable promise as a 2D microstructural computational framework for predicting the overall thermo-mechanical response of asphalt mixtures based on the nature of the microstructure. More detailed studies of this approach are presented in the next chapter as are efforts to develop 3D models.

CHAPTER V

3D MICROSTRUCTURAL MODELING OF ASPHALT CONCRETE*

V.1 Introduction

This chapter presents a 3D image-based microstructural computational modeling framework to predict thermo-viscoelastic, thermo-viscoplastic, and thermo-viscodamage response of asphalt concrete. X-ray CT is used to scan dense-graded asphalt concrete (DGA) to obtain slices planar images from which the 3D microstructure is reconstructed. Image processing techniques are used to enhance the quality of images in terms of phase identification and separation of particles. This microstructure is divided to two phases: aggregates and matrix. The aggregate phase is modeled as an elastic material and the matrix phase is modeled as a thermo-viscoelastic, thermo-viscoplastic, and thermo-damage material. Stress-strain response, damage propagation, and the distributions of the viscoelastic and viscoplastic strains are predicted by performing virtual uniaxial and repeated creep-recovery tests of the developed 3D model of asphalt concrete. The effects of loading rate, temperature, and loading type on the thermo-mechanical response of asphalt concrete are investigated. In addition, the microscopic and macroscopic responses of the DGA are compared with those of stone matrix asphalt (SMA). The results demonstrated that SMA can sustain higher strain levels at the microscopic level

---

* Reprinted with permission from "Three-dimensional microstructural modeling of asphalt concrete using a unified viscoelastic–viscoplastic–viscodamage model" by Taesun You, Rashid Abu Al-Rub, Masoud Darabi, Eyad Masad, and Dallas Little, 2012. Construction and Building Materials, 28, 531-548, Copyright 2012 by Elsevier.

and higher macroscopic ultimate strength. The damage in SMA was more localized than the DGA. The microstructure-based framework presented in this paper can be used to offer insight on the influence of the distribution and properties of microscopic constituents on the macroscopic behavior of asphalt concrete. It is noted that the text, figures, and tables in this chapter had been published in You et. al. [58].

V.2 3D Image-based Microstructural Modeling

This section describes the steps that were followed to generate the 3D microstructure of asphalt concrete.

- **Step: 1 Preparing Specimens of Asphalt Concrete**

  Cylindrical specimens of two types of asphalt concrete were prepared: DGA and SMA. The diameter and height of DGA are 101.6 mm (4 inch) and 152.4 mm (6 inch), respectively, whereas the specimen of SMA has 50 mm diameter and 75 mm height.

- **Step 2: Obtaining CT images**

  The X-ray CT system in the Advanced Characterization of Infrastructure Materials (ACIM) laboratory at Texas A&M University (Figure V-1) was used to scan DGA and SMA specimens. Its maximum resolution is 0.17 mm/pixel in all directions [59]. By using the X-ray CT, 753 planar images for DGA and 40 images for SMA were obtained (i.e., the resolutions used to scan DGA and SMA are 0.20 mm/pixel and 1.0 mm/pixel, respectively).

- **Step 3: Processing CT images**

Scanned CT images of asphalt mixtures have different grayscale intensities between 0 and 255, where denser materials such as aggregates have higher intensity, shown as brighter color [See Figure V-2 (a)]. The 2D CT images have three phases: aggregates, mastic (binder with fine aggregates), and air voids. In this study, however, air voids and mastic are considered as one phase called a matrix. A variety of digital image filters and 3D convolution technique in commercial software Avizo [60] were applied to clearly distinguish the two phases (aggregate and matrix phases) in the grayscale images [60].

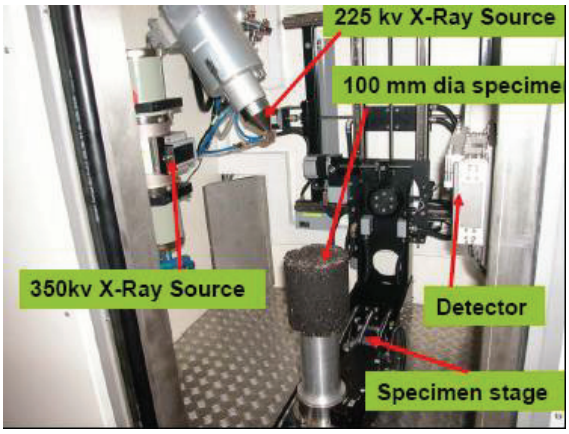

Figure V-1. X-ray CT system at Texas A&M University [59].

The processed grayscale image, shown in Figure V-2 (b), was converted to a binary image, where each pixel is represented as 0 or 1 (i.e., black or white). Thresholding, an image segmentation technique, was used to convert the grayscale image to a binary image, as shown in Figure V-2 (c). In this study, a thresholding level of 90 was used. This means that the part of the grayscale image with

intensities between 90 and 255 would be identified as aggregate phase, and the parts of the image with an intensity less than 90 would be identified as matrix [Figure V-2 (d)].

By connecting each aggregate particle in slices of the processed binary image using Avizo [60], the 3D aggregate phase could be extracted. In the DGA microstructure only aggregates greater than 1.30 mm were considered as the aggregate phase, whereas the minimum size of aggregate was 2.34 mm in the SMA microstructure. It should be noted that fine aggregates in the processed images could not be considered in the 3D microstructure due to high computational costs. For more details about image processing methods see Avizo User's Guide [60].

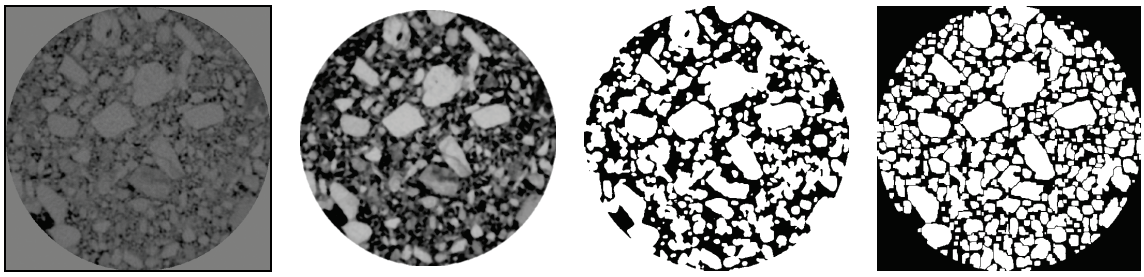

(a) (b) (c) (d)

Figure V-2. Images of dense-graded asphalt concrete: (a) original X-ray CT (grayscale) image, (b) processed grayscale image, (c) converted binary image, and (d) processed binary image.

- **Step 4: Constructing finite element model**

Once the aggregate phase, shown in Figure V-3 (a) and (c), was determined, the matrix phase could be obtained by subtracting aggregate phase from cylindrical solid. The two phases were assumed to be perfectly bonded by merging those in Abaqus [11] as it is very hard to identify interfacial properties experimentally. In this study, numerous four-node 3D linear tetrahedron elements were used in meshing 3D microstructures: 1.9 million elements for the microstructure of DGA and 1.7 million elements for the microstructure of SMA, as shown in Figure V-3 (b) and (d). The entire bottom of the model was constrained from moving in the axial direction and the load applied at the top.

It is noteworthy that direct aggregate to aggregate contact is neglected in the current study as little knowledge exists about the accurate conditions of such a contact. However, in this study, the existence of a thin mastic film is assumed between each aggregate and the other, which simulates to some extent the adsorption of aggregate to some of the asphalt binder phase. This asphalt film allows one to simulate a viscoelastic contact condition between different aggregates. More fundamental research is needed to investigate the accurate aggregate-aggregate contact conditions. However, the minimum thickness of the binder between the adjacent separated aggregates decided the minimum element size in the generated finite element model. Using a very small binder thickness for separating the contacted aggregates may significantly increase the computational time. Therefore, one should decide on the optimum thickness for separating the aggregates to balance the desired accuracy and the available computational power. This

will also be dependent on the resolution of the obtained X-ray CT images and the employed image software. In this study, 1 mm for the microstructure of SMA and 2 mm for the microstructure of DGA are assumed as the binder layer thickness to separate aggregates from each others that led to reasonable simulation times. In other words, the minimum element sizes for meshing are 1 mm for the microstructure of SMA and 2 mm for the microstructure of DGA.

3D microstructural simulations were conducted using the supercomputer HYDRA in the supercomputing facility at Texas A&M University. HYDRA is an IBM p575 massive parallel supercomputer having cumulative capacity of 640 processors and 1632 GB of memory. The average CPU running time for a simulation is around 60 hours for the microstructure of DGA and 40 hours for the microstructure of SMA.

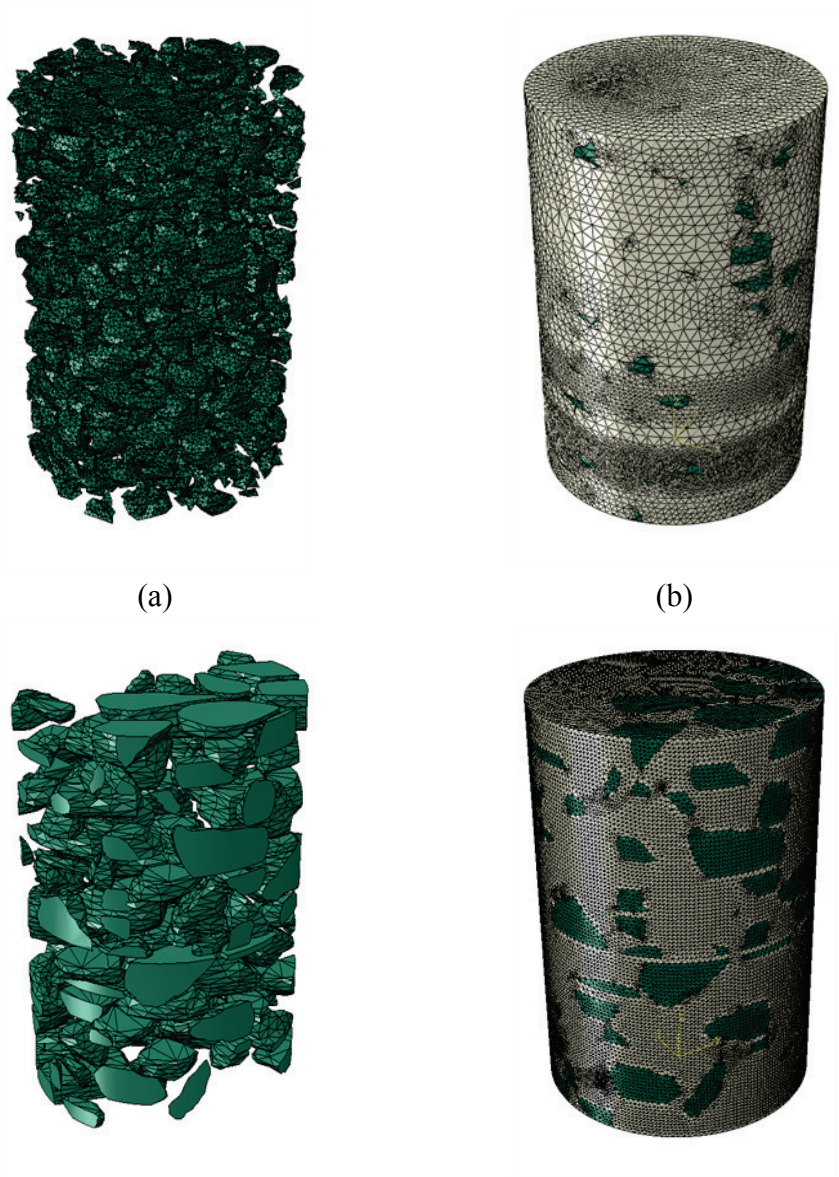

Figure V-3. 3D microstructure: (a) aggregates for Dense-Graded asphalt concrete, (b) finite element meshed model for DGA, (c) aggregates for Stone Matrix Asphalt , and (d) finite element meshed model for SMA.

V.3 Numerical Simulation Using the Microstructure of SMA

It is known that asphalt concrete is rate- and temperature-dependent material. The uniaxial test was simulated to investigate the effects of strain rate and temperature. The modulus of elasticity and Poisson's ratio for the aggregate were assumed to be 25 GPa and 0.25, respectively [33], whereas those for the matrix are as listed in Table IV-1 and Table IV-2. The Poisson's ratio of the mastic (binder with fine aggregates) is assumed to be constant with a value of 0.49. These parameters have been identified by Abu Al-Rub et al. [56] for nonlinear viscoelasticity and viscoplasticity and by Darabi et al. [23] for viscodamage. The focus of this study is on the influence of the material parameters listed in Table IV-1 and the influence of different loading conditions on the overall 3D thermo-mechanical response of asphalt mixtures. The effects of different types of binders and aggregates as well as the distribution of air voids on the overall thermo-mechanical response of asphalt concrete are beyond the scope of this study but are currently being investigated. Such studies require an extensive experimental program to identify the thermo-viscoelastic, thermo-viscoplastic, and thermo-viscodamage behaviors of different asphalt binders and the elastic-damage behavior of different types of aggregates.

V.3.1 The Effect of Strain Rate

In order to investigate the effect of strain rate, three different tensile and compressive strain rates were applied to the 3D cylindrical asphalt concrete, and the resulting stress-strain diagrams for tensile and compressive strain rates at a temperature of 20°C are presented in Figure V-4. The corresponding damage density, viscoelastic strain, and

effective viscoplastic strain distributions in tension and compression are shown in Figure V-6 to Figure V-11. Note that in this work, the negative sign corresponds to tensile stresses and strains, whereas the positive sign corresponds to the compressive stresses and strains. As shown in Figure V-4, the loading rate has a significant effect on the initial stiffness, the ultimate strength, and the strain to failure in both tension and compression. Figure V-4 clearly shows that the asphalt concrete behaves more brittle as the strain rate increases. This observation is in agreement with the behavior of time- and rate-dependent materials where less viscous behavior is usually observed as the loading rate increases. This figure also clearly shows the ability of the current modeling in taking into consideration the different behavior of asphalt concrete under compressive and tensile loading conditions, where the strength of the asphalt concrete in compression is greater than that in tension. Interestingly, Figure V-4 shows that the presented 3D cylindrical microstructure and the constitutive model can be used effectively to predict the effect of the strain rate on the mechanical response of asphalt concrete in both tension and compression. Moreover, the results in Figure V-4 are in close qualitative and quantitative agreement with experimental data on asphalt mixtures at room temperature and under tensile and compressive uniaxial loading [see the experimental data in [23, 25, 49, 56]]. Qualitatively, the behavior is more brittle under tension and more ductile under compression as evidenced in Figure V-4. Quantitatively, the ultimate tensile strength of an asphalt mixture is generally between 75-85% of the corresponding compressive strength [23, 25, 49, 56]. The results in Figure V-4 are within this range.

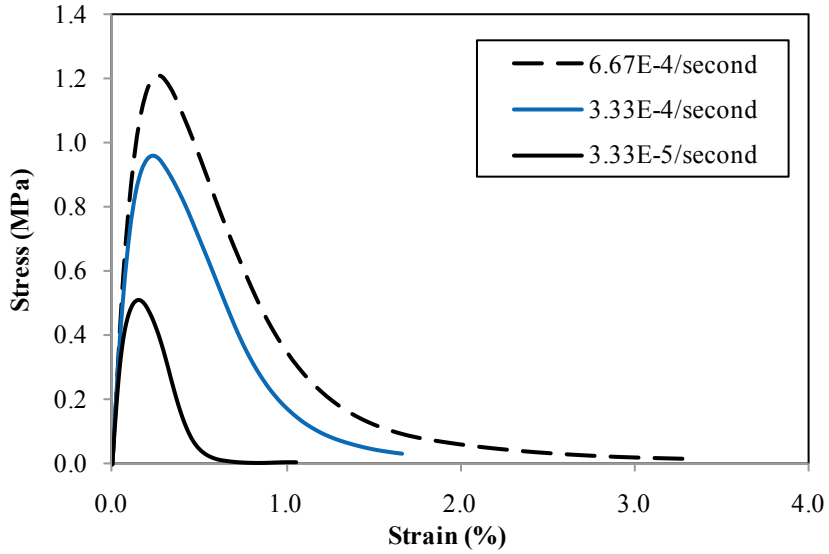

(a)

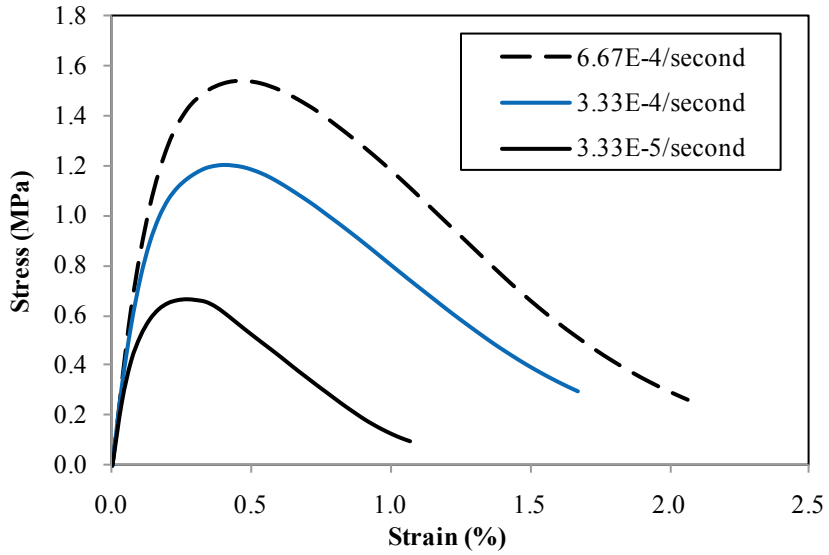

(b)

Figure V-4. Stress-strain diagrams for different strain rates in: (a) tension and (b) compression (T=20 °C).

Figure V-5 shows the damage evolution at different vertical sections of the specimen at 1% strain level when the tensile strain rate is 6.67×10^{-4}/sec. This same figure shows that at 1% strain level, the matrix, which consists mostly of asphalt binder

that bonds the aggregates together, gets damaged and can be considered as the region where the crack nucleation and propagation occurs. It appears that the matrix phase is a critical place for the strain and damage localization because of the significant difference between the mechanical properties of the coarse aggregate phase and the matrix phase. Moreover, Figure V-6 and Figure V-7 show that asphalt concrete subjected to faster loading rate get damaged earlier or at lower strain levels. This observation can be attributed to the time- and rate-dependent response of asphalt concrete. In other words, the induced stresses in the matrix phase can relax faster at slower loading rates which lead to lower stress localization and subsequently slower damage evolution. However, one may argue that although at slower strain rates the induced stresses relax more, the loading time is longer which may cause more damage in the specimen since the damage model is also time-dependent. Therefore, it can be concluded that the degree of the induced damage in the specimen subjected to different strain rates is the result of two competing mechanisms: (a) the relaxation of the stress level which contributes in lowering the damage, and (b) the loading time which contributes in increasing the damage due to the viscodamage behavior of the asphalt concrete. The results in Figure V-6 and Figure V-7 clearly show that the effect of the stress relaxation is more significant for the selected model parameters in Table IV-1 and Table IV-2. As it was expected, a comparison between Figure V-6 and Figure V-7 show that at the same strain levels (e.g., 1%), the specimen in the tensile loading experiences more localized damage density than the specimen subjected to compression.

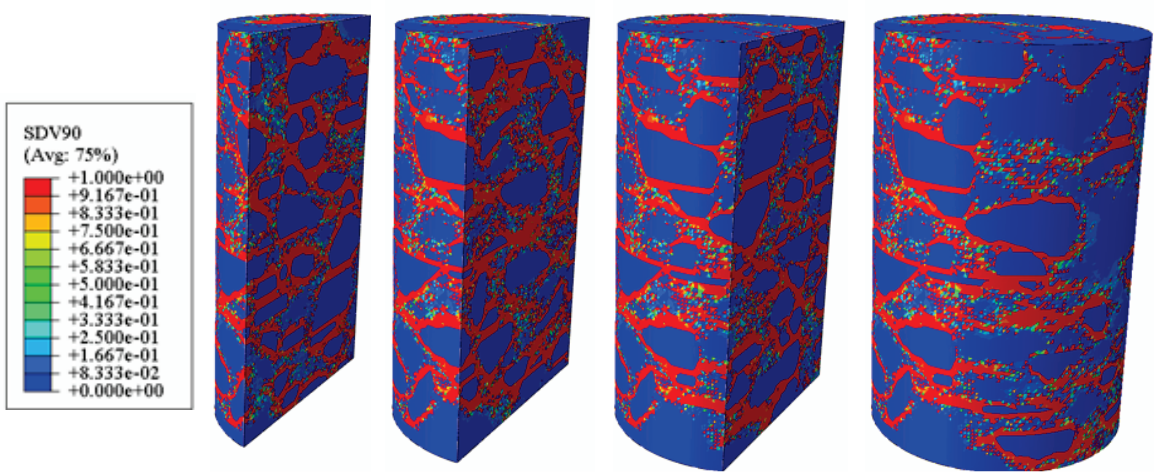

(a) (b) (c) (d)

Figure V-5. Damage density distribution of tensile strain rate 6.67×10^{-4}/second at strain level of 1.0% and temperature T=20 °C: (a) third cut, (b) half cut, (c) two-third cut, and (d) whole specimen.

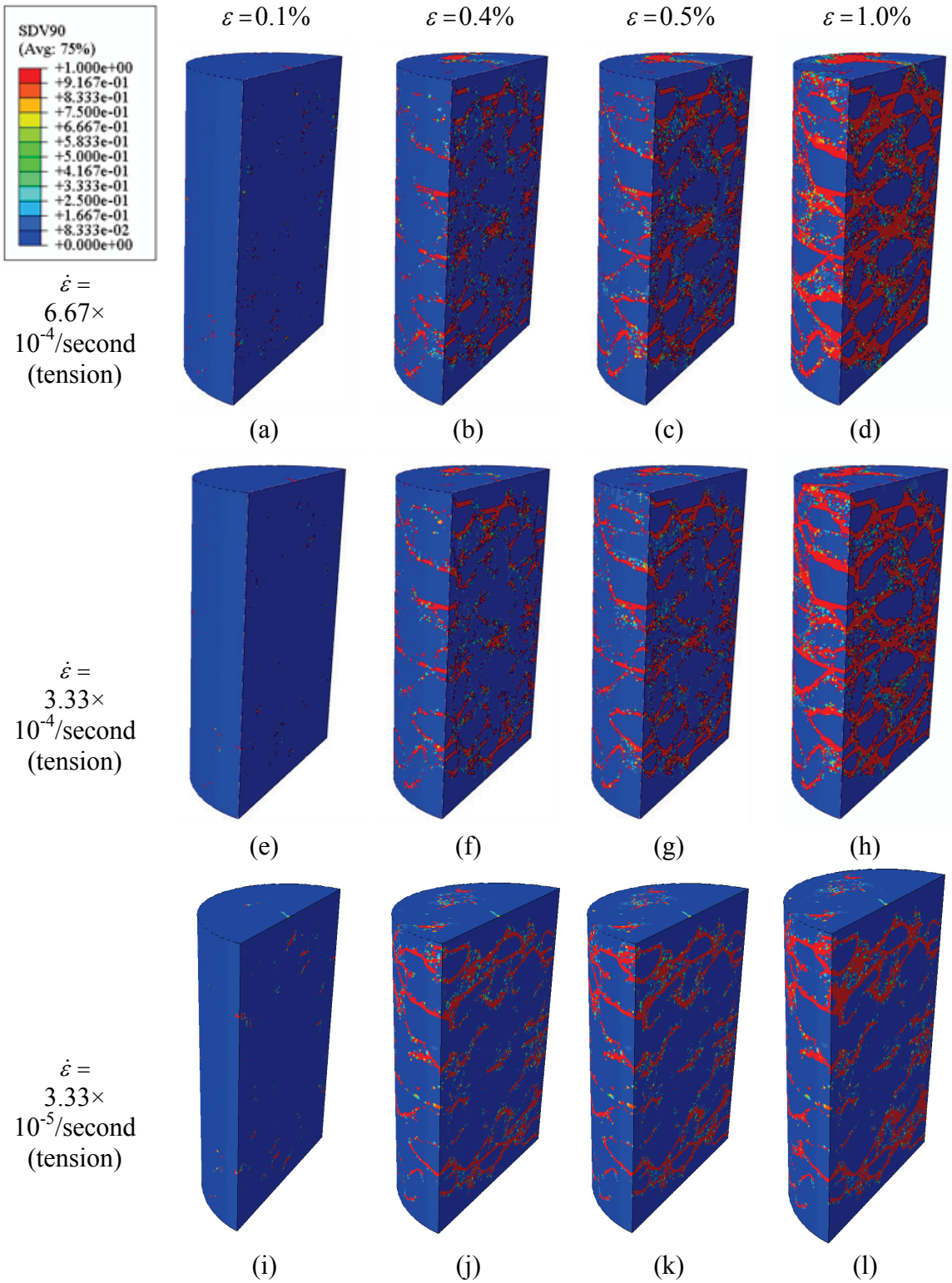

Figure V-6. Damage density distribution at different tensile strain rates and at different strain levels at temperature T=20 °C.

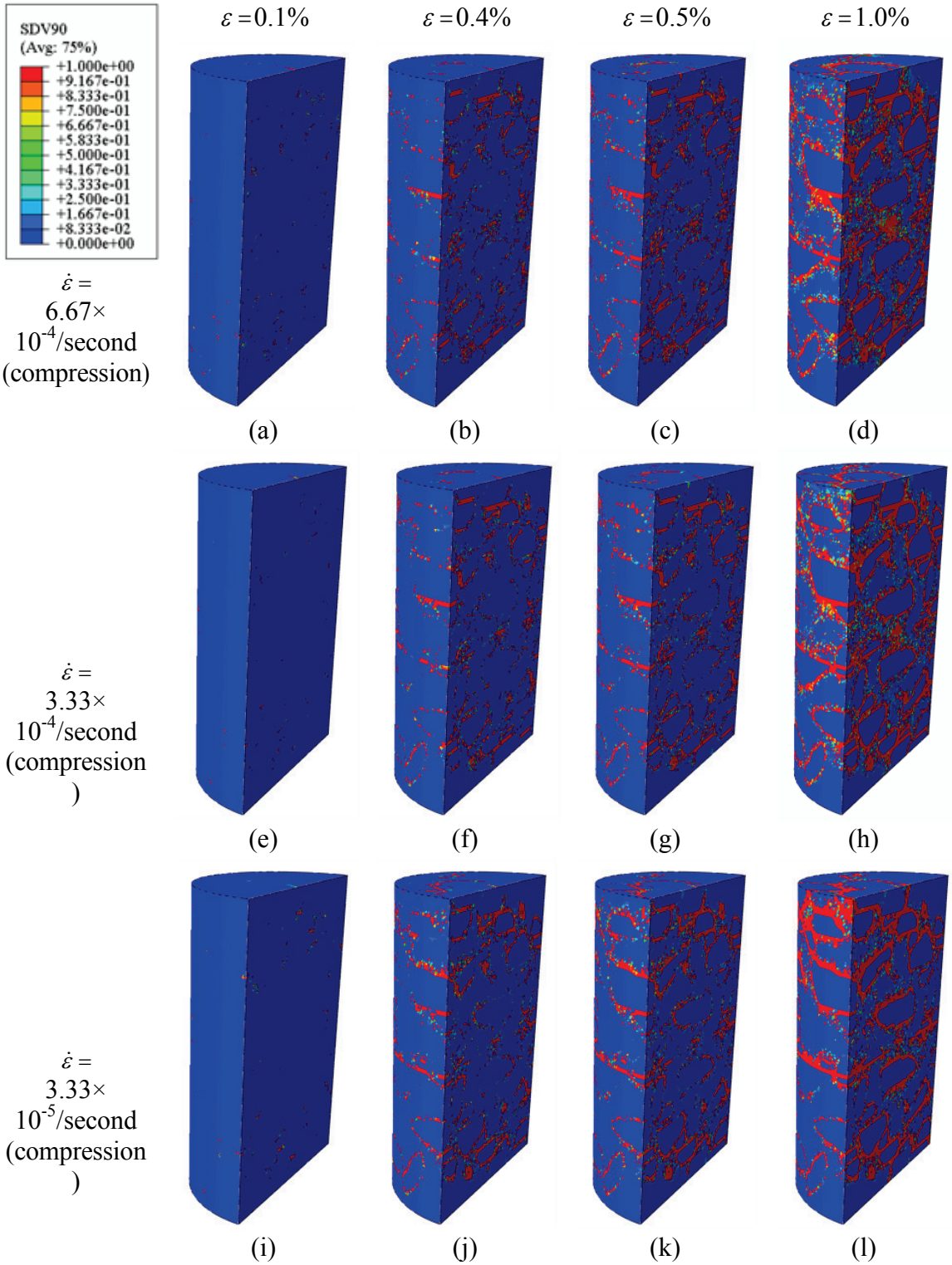

Figure V-7. Damage density distribution at different compressive strain rates and different strain levels at temperature T=20 °C.

As shown in Figure V-8 and Figure V-9, highly heterogeneous viscoelastic strain distribution is seen and is more localized at the interface between the aggregates and the mastic as the strain rate decreases because of the significant difference between the mechanical properties of the aggregate and the matrix. The viscoelastic strain is more uniformly distributed as the rate of loading increases. Also, localized tensile (negative) and compressive (positive) viscoelastic strains are seen due to the constraints imposed by the aggregates on deformation. Note that in order to more clearly see the viscoelastic and viscoplastic strains distributions, the aggregates are removed from Figure V-8 to Figure V-11 since they are elastic.

As shown in Figure V-8 to Figure V-11, more viscoelastic strains are observed at higher loading rates, while the viscoplastic strain, obtained by subtracting viscoelastic strain from total strain, is less in specimens subjected to higher rate of loading. Moreover, at a temperature of 20°C, one can notice that the viscoelastic strain portion of the total imposed strain is higher than the viscoplastic strain. Therefore, the effect of varying the temperature on the stress-strain response and damage, viscoelastic strain, and viscoplastic strain distributions is shown next.

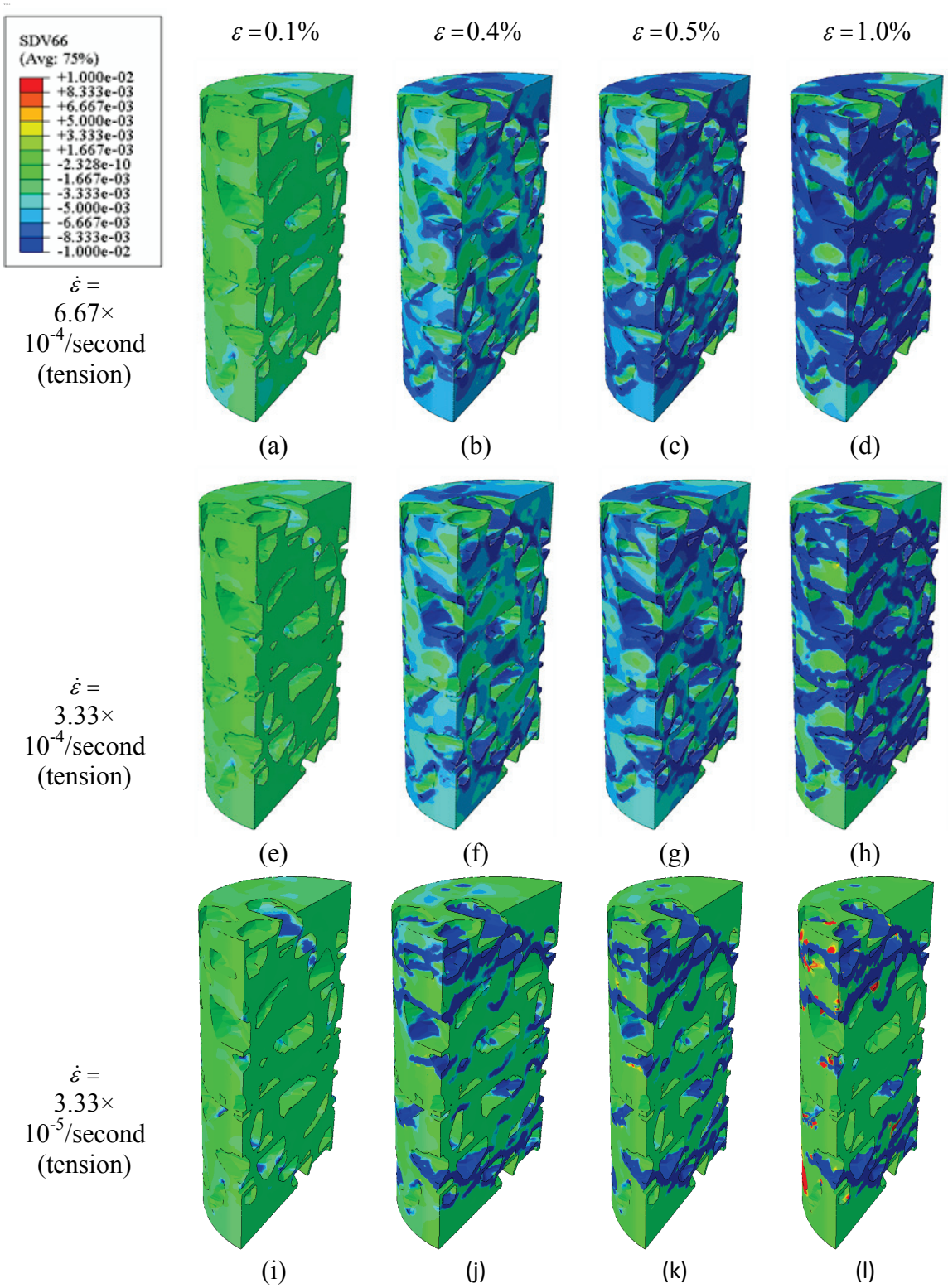

Figure V-8. Viscoelastic strain distribution at different tensile strain rates and different strain levels at temperature T=20 °C.

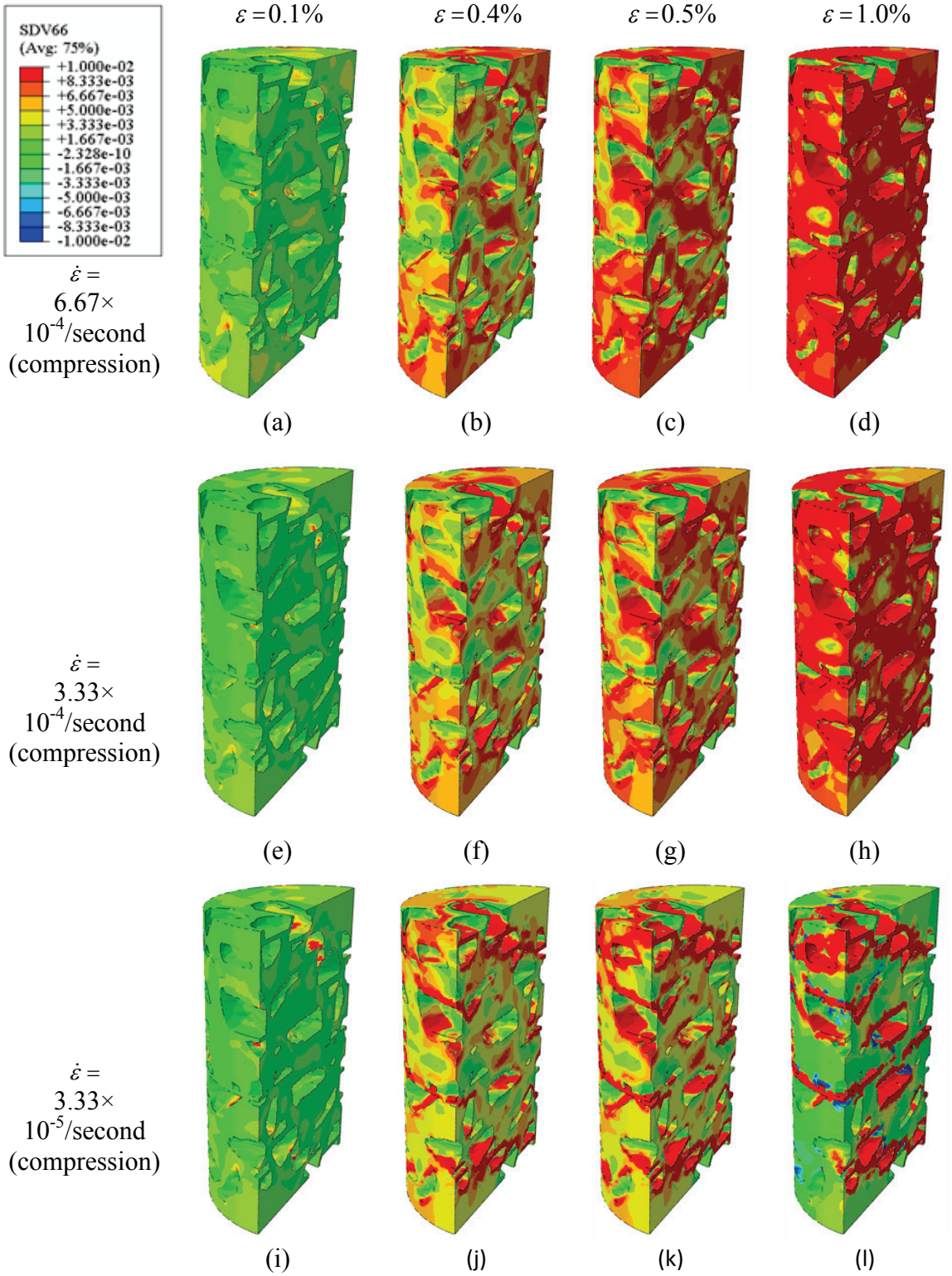

Figure V-9. Viscoelastic strain distribution at different compressive strain rates and different strain levels at temperature T=20 °C.

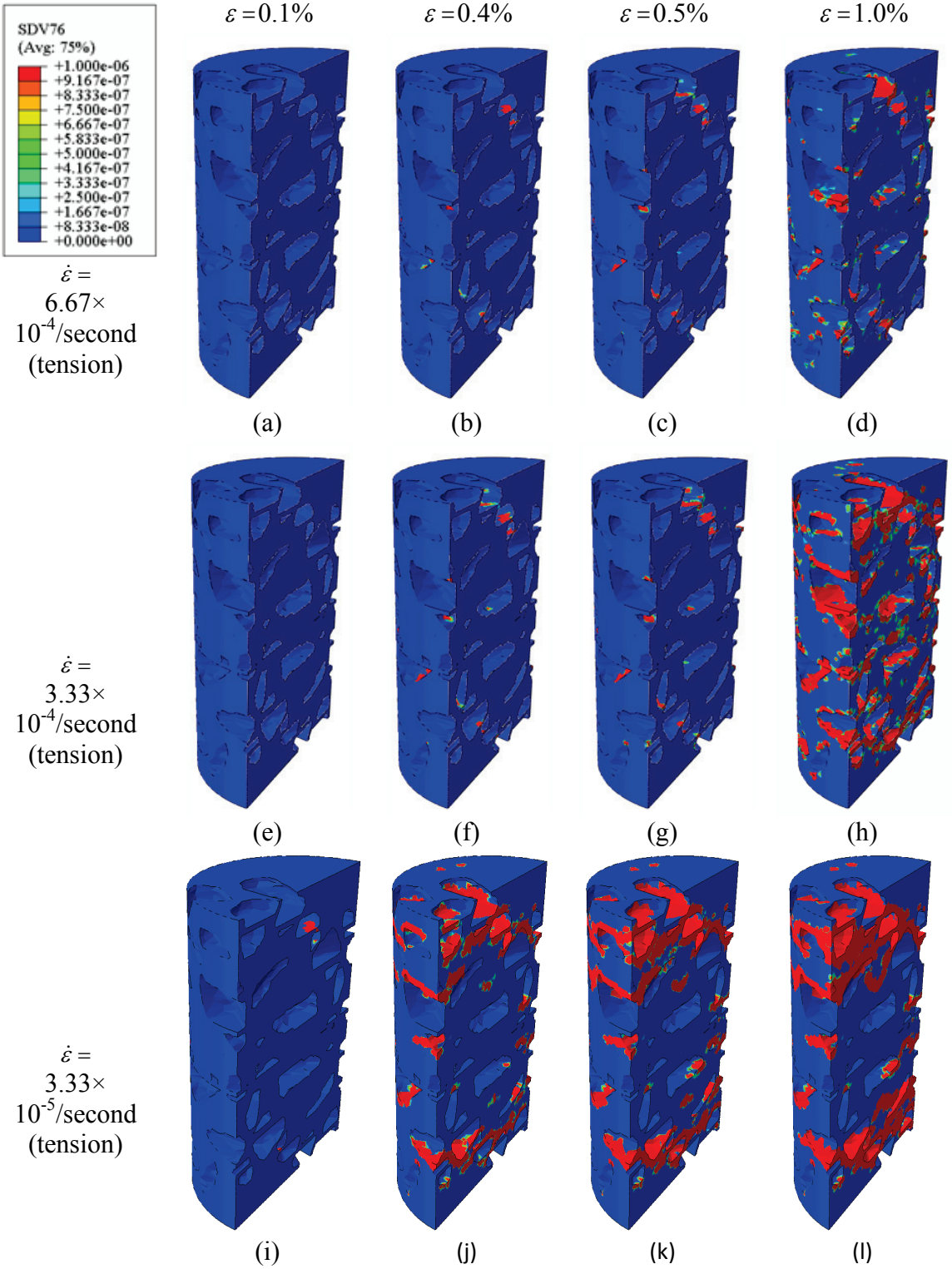

Figure V-10. Effective viscoplastic strain distribution at different tensile strain rates and different strain levels at temperature T=20 °C.

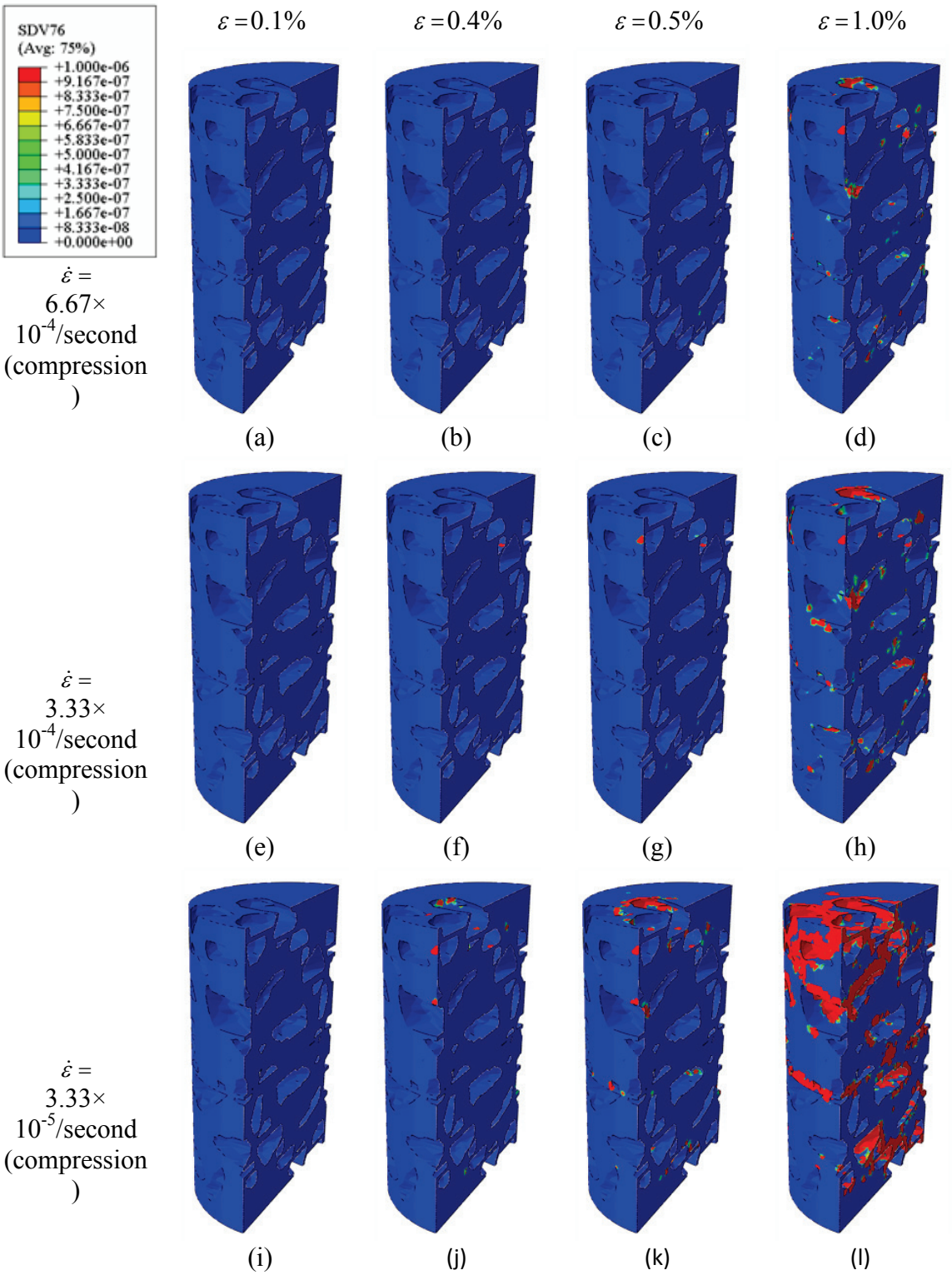

Figure V-11. Effective viscoplastic strain distribution at different compressive strain rates and different strain levels at temperature T=20 °C.

V.3.2 The Effect of Temperature

The responses of the asphalt concrete subjected to compressive uniaxial loading is simulated at three different temperatures (10 ºC, 20 ºC, and 40 ºC) at a strain rate of 3.33×10^{-4}/sec in order to investigate the effect of temperature on the mechanical response of asphalt concrete. The stress-strain responses are presented in Figure V-12. The damage density, viscoelastic strain, and effective viscoplastic strain distributions (at 0.5% and 1.0% strain levels) are shown in Figure V-13 to Figure V-15, respectively. It is apparent that the overall behavior of asphalt concrete strongly depends on temperature, as shown in Figure V-12. This same figure clearly shows that the initial stiffness and the ultimate strength of the asphalt concrete increase as the temperature decreases. However, at a specific strain level, the material is more prone to damage at low temperatures as clearly shown in Figure V-13 where more damage distribution is seen as temperature decreases. Furthermore, Figure V-14 and Figure V-15 show higher values for the viscoelastic strain and lower values for the viscoplastic strain at higher temperatures, respectively. More viscoplastic strain is seen as temperature decreases since the material gets softer (weaker) due to more damage evolution as temperature decreases. The effect of temperature on the creep-recovery response is shown next.

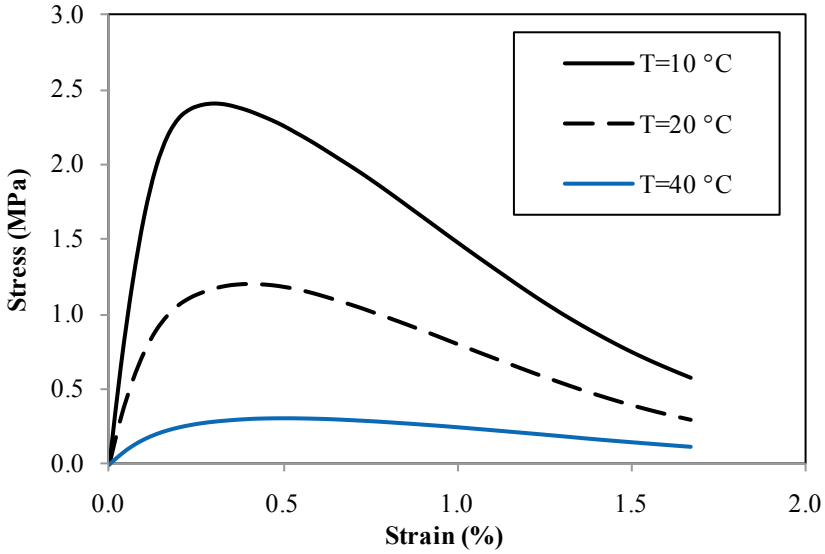

Figure V-12. Stress-strain responses at different temperatures under a compressive strain rate 3.33×10^{-4}/second.

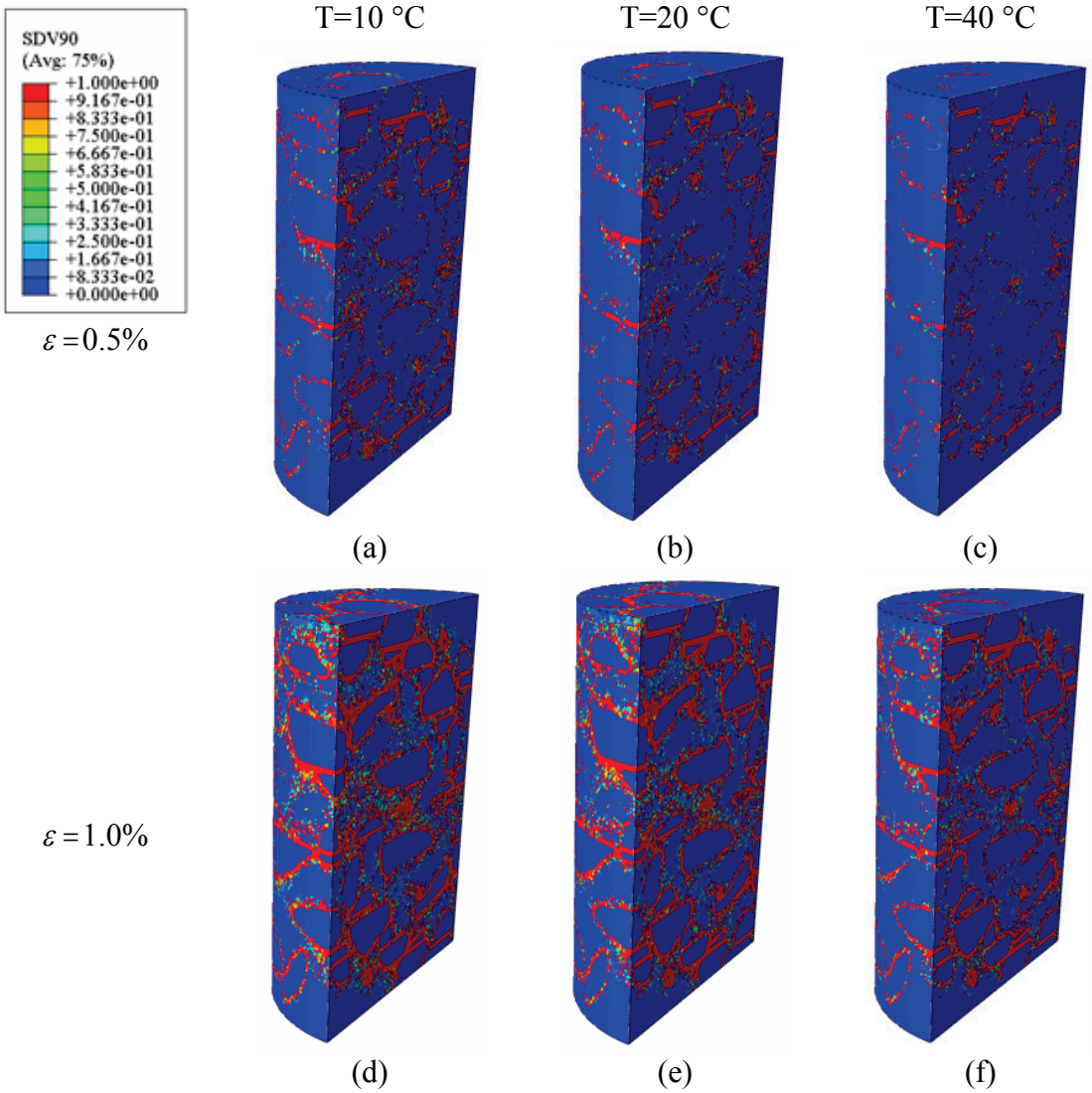

Figure V-13. Damage density distribution at two different strain levels for various temperatures (compressive strain rate 3.33×10^{-4}/second).

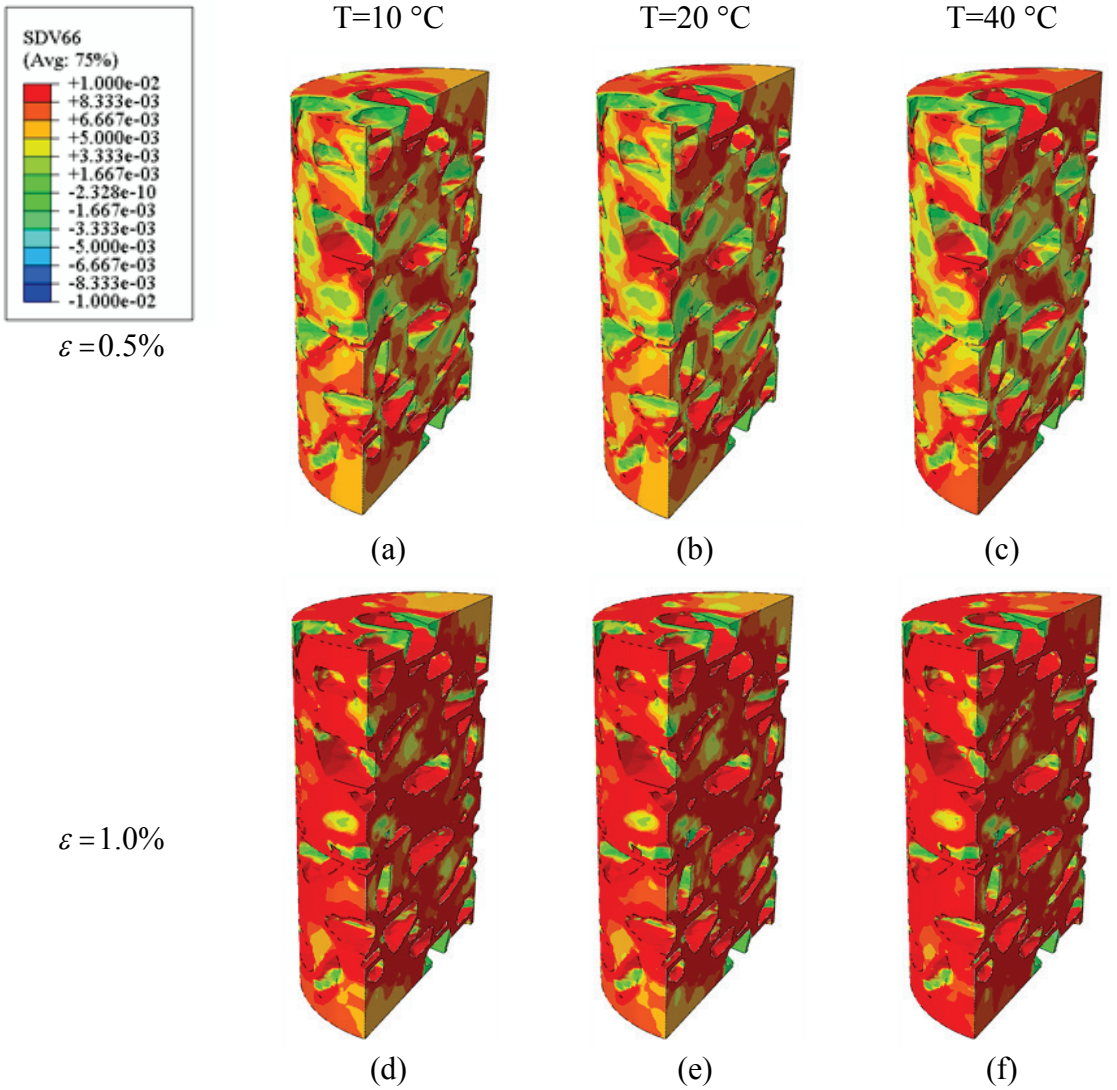

Figure V-14. Viscoelastic strain distribution at two different strain levels for various temperatures (compressive strain rate 3.33×10^{-4}/second).

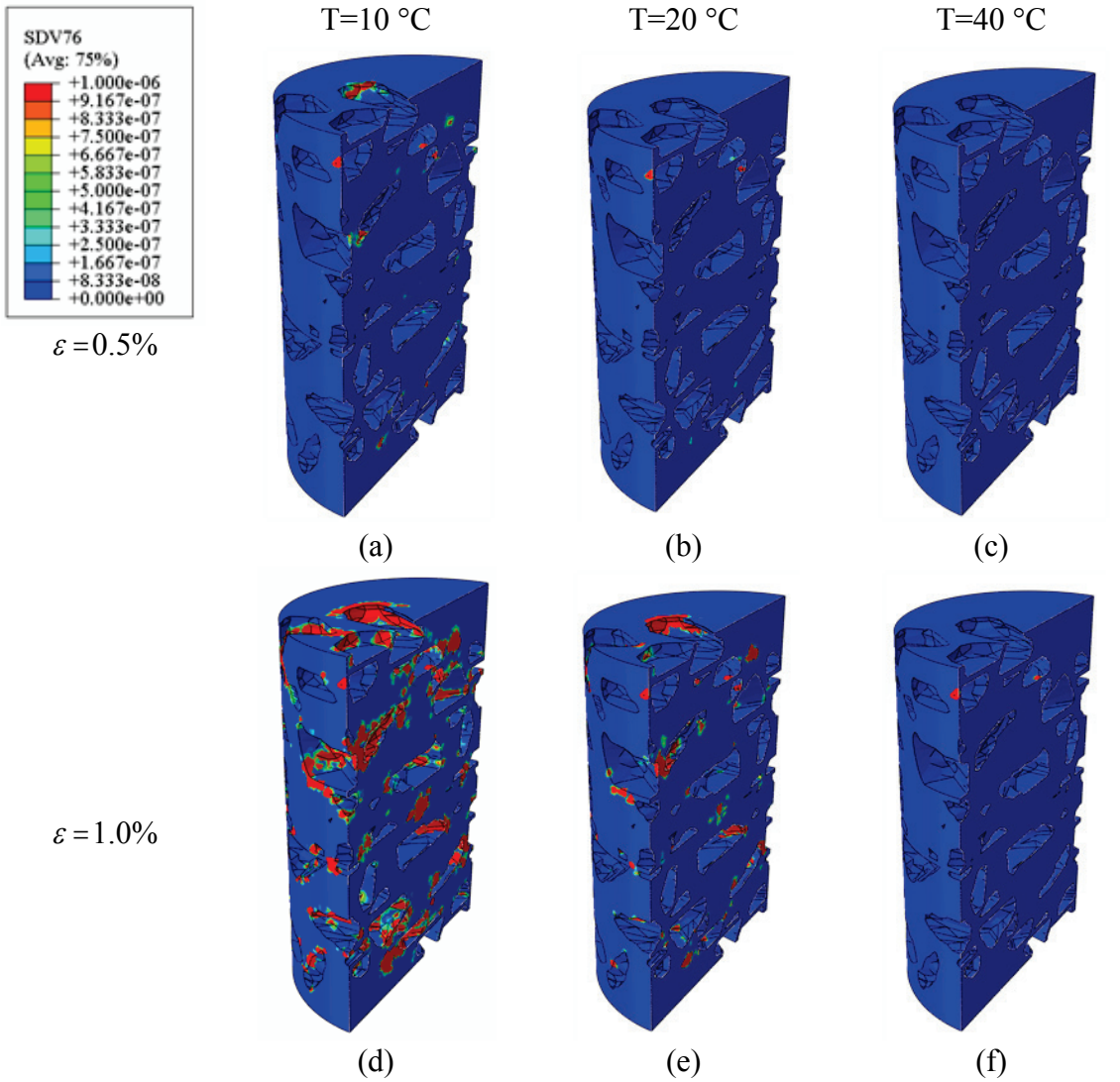

Figure V-15. Effective viscoplastic strain distribution at two different strain levels for various temperatures (compressive strain rate 3.33×10^{-4}/second).

V.3.3 The Effect of Loading Type

Compressive repeated creep-recovery tests were simulated at temperatures of 10 ºC and 20 ºC. This test is more representative to what the asphalt mixture experiences under traffic loading. Figure V-16 (a) and Figure V-17 (a) show the stress input history for the repeated creep-recovery test where the loading and unloading periods are 10 and 2

seconds, respectively. Generally, micro-damage healing occurs in asphalt mixtures during the unloading period [25, 61]; however, micro-damage healing was not considered in the current study and therefore small unloading periods are assumed here. The corresponding strain-time responses are presented in Figure V-16 (b) and Figure V-17 (b). It is apparent that the strain level at 20 ºC and 10 ºC has developed incrementally as shown in Figure V-16 (b) and Figure V-17 (b) where the primary, secondary, and tertiary creep regions can be observed clearly. Moreover, damage density distributions, viscoelastic strain distribution, and effective viscoplastic distribution at different times for 20 ºC and 10 ºC are shown in Figure V-18 to Figure V-23, where it is apparent that the damage evolves as the number of loading cycles increases. Damage initiates earlier at the lower temperature 10 ºC. Figure V-16 (b) and Figure V-17 (b) show that the model is capable of simulating the response associated with creep and fatigue damage since: (a) it shows the gradual accumulation of the damage within the specimen as the number of loading cycle increases; and (b) the strain level at failure for the repeated loading is less than that in uniaxial loading. Figure V-18 to Figure V-23 also show that the damage, viscoelastic strain, and viscoplastic strain initiates at the aggregate-mastic interface and then distributes through the whole specimen.

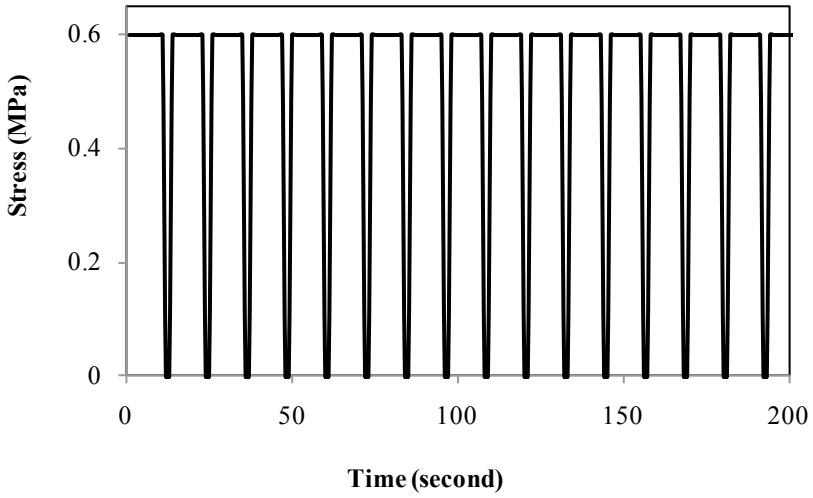

(a)

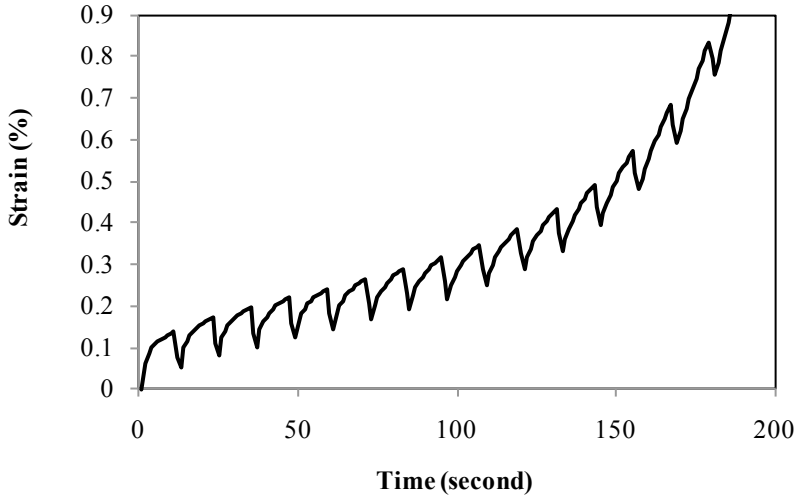

(b)

Figure V-16. Repeated creep-recovery compression test at temperature T=20 °C: (a) applied stress-time diagram and (b) strain-time response.

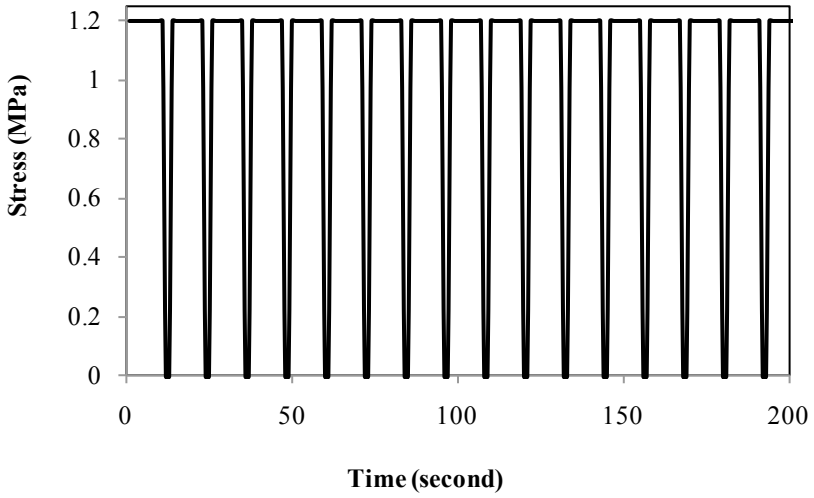

(a)

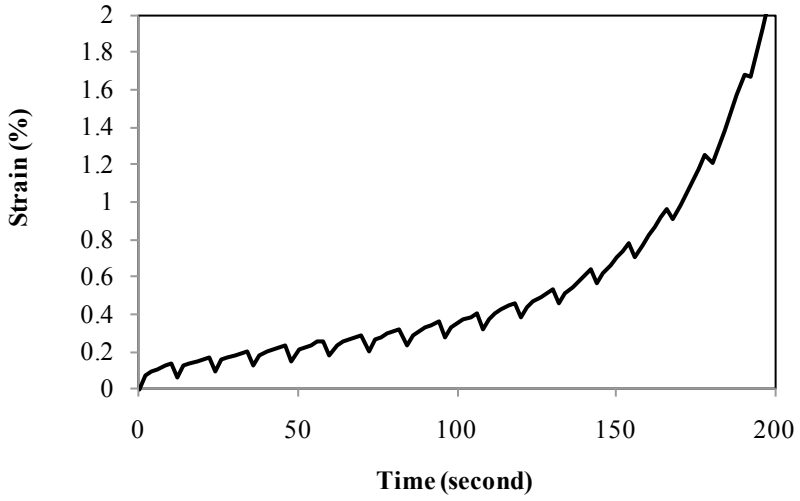

(b)

Figure V-17. Repeated creep-recovery compression test at temperature T=10 °C: (a) applied stress-time diagram and (b) strain-time response.

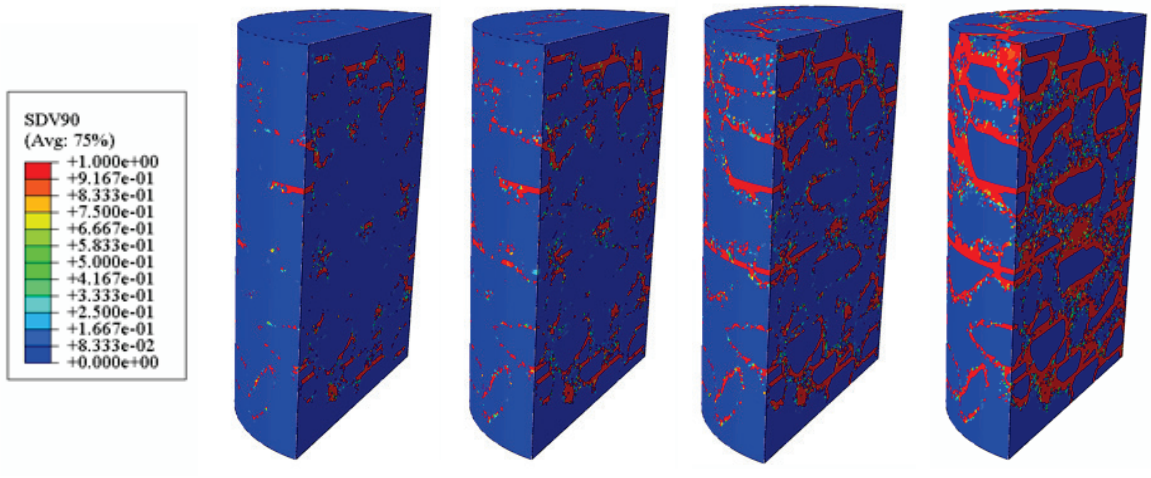

(a) (b) (c) (d)

Figure V-18. Damage density distribution of repeated creep-recovery compressive test at temperature T=20 °C at: (a) 50 seconds (4 cycles), (b) 100 seconds (9 cycles), (c) 150 seconds (13 cycles), and (d) failure (16 cycles).

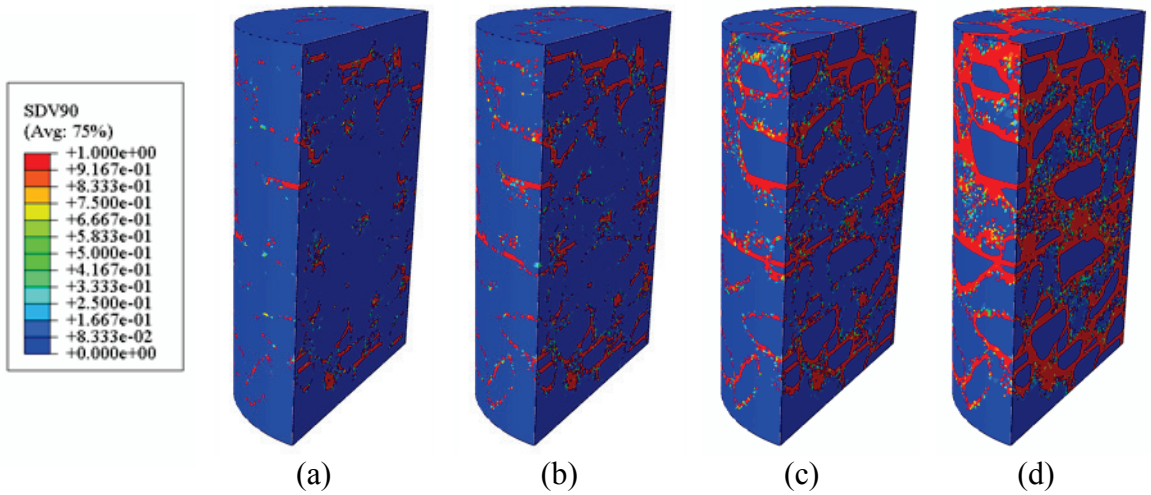

(a) (b) (c) (d)

Figure V-19. Damage density distribution of repeated creep-recovery compressive test at temperature T=10 °C at: (a) 25 seconds (2 cycles), (b) 50 seconds (4 cycles), (c) 75 seconds (7 cycles), and (d) failure (17 cycles).

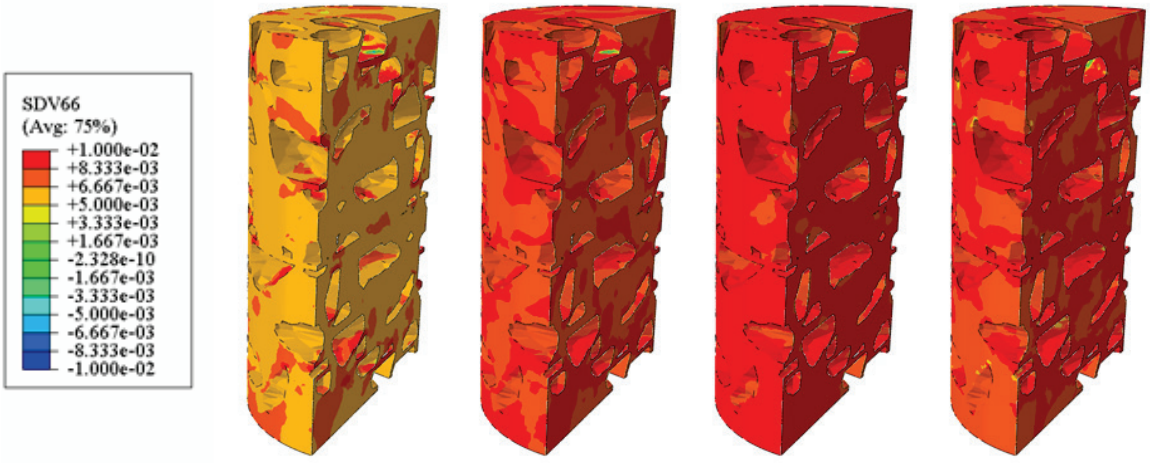

(a) (b) (c) (d)

Figure V-20. Viscoelastic strain distribution of repeated creep-recovery compressive test at temperature T=20 °C at: (a) 50 seconds (4 cycles), (b) 100 seconds (9 cycles), (c) 150 seconds (13 cycles), and (d) failure (16 cycles).

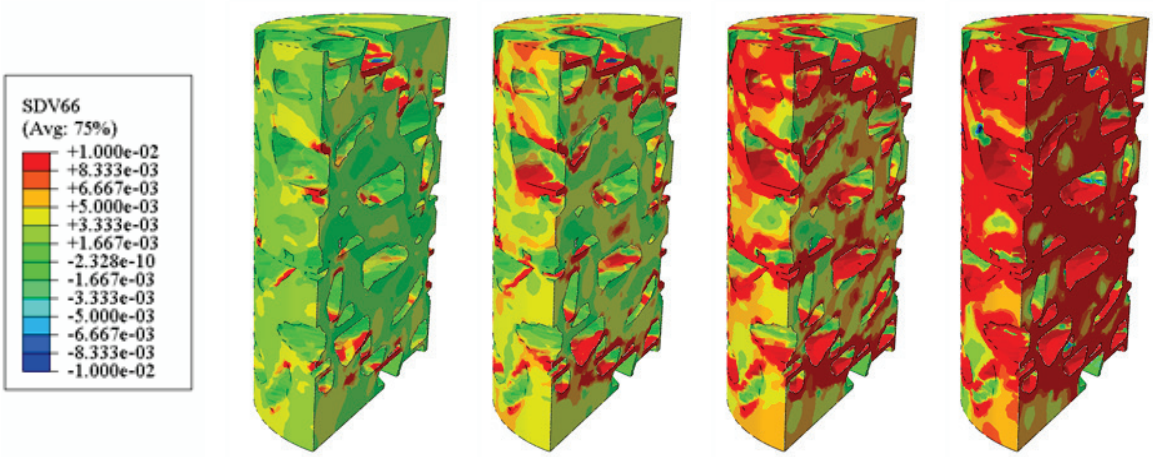

(a) (b) (c) (d)

Figure V-21. Viscoelastic strain distribution of repeated creep-recovery compressive test at temperature T=10 °C at: (a) 25 seconds (2 cycles), (b) 50 seconds (4 cycles), (c) 75 seconds (7 cycles), and (d) failure (17 cycles).

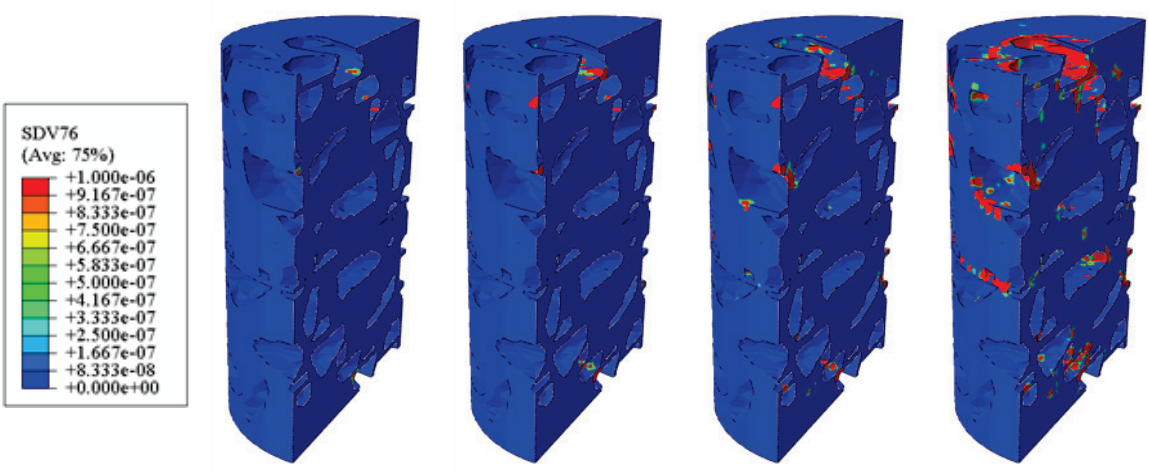

(a) (b) (c) (d)

Figure V-22. Effective viscoplastic strain distribution of repeated creep-recovery compressive test at temperature T=20 °C at: (a) 50 seconds (4 cycles), (b) 100 seconds (9 cycles), (c) 150 seconds (13 cycles), and (d) failure (16 cycles).

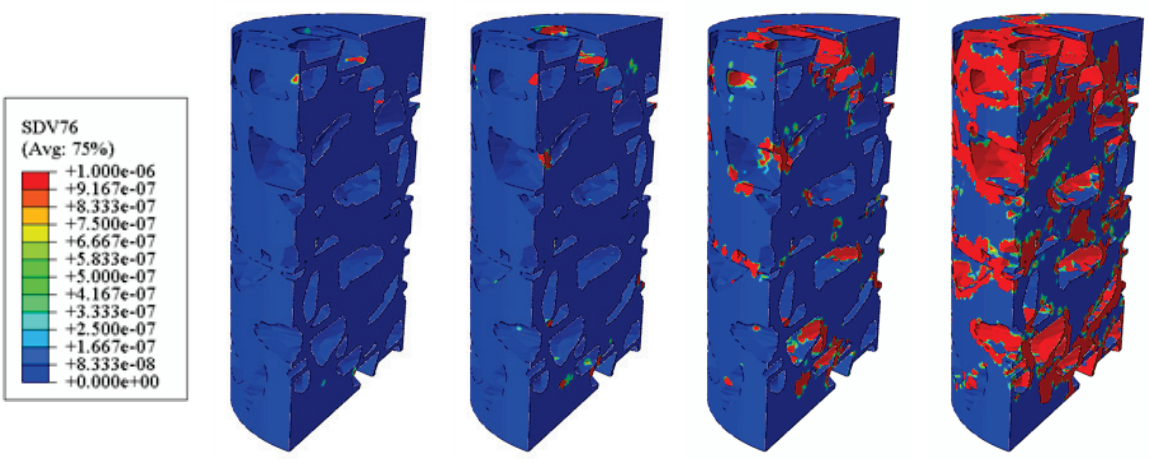

(a) (b) (c) (d)

Figure V-23. Effective viscoplastic strain distribution of repeated creep-recovery compressive test at temperature T=10 °C at: (a) 25 seconds (2 cycles), (b) 50 seconds (4 cycles), (c) 75 seconds (7 cycles), and (d) failure (17 cycles).

V.4 Numerical Simulation Using the Microstructure of Dense-graded Asphalt Concrete

Uniaxial monotonic tests are simulated to investigate temperature- and rate-dependent response of DGA. In addition, simulations of repeated creep-recovery test are performed to investigate damage under cyclic loading. The modulus of elasticity and Poisson's ratio for the aggregate were assumed to be 25 GPa and 0.25, respectively [33]. Moreover, the material parameters for the mastic were as listed in Table IV-1 and Table IV-2, where Abu Al-Rub et al. [56] has identified viscoelastic and viscoplastic parameters and Darabi et al. [23] has identified viscodamage parameters. The Poisson's ratio for the mastic was assumed to be 0.49. Note that in this work, the positive sign corresponds to compressive stress and strains, whereas the negative sign corresponds to tensile stress and strains.

V.4.1 The Effect of Strain Rate

The effect of strain rate was investigated by simulating uniaxial compressive and tensile tests at a temperature of 20 °C. Three different strain rates were used: 1.97×10^{-4}/s, 3.94×10^{-5}/s, and 1.97×10^{-5}/s. The resulting stress-strain diagrams for compressive and strain rates are presented in Figure V-24, where it is clearly shown that the model is capable of capturing the significant effect of strain rate on overall response of DGA under both compressive and tensile loadings. Namely, initial stiffness and ultimate strength increases as strain rate increases because there is not enough time to have viscous response at higher loading rates. It is also shown that the current microstructure combined with the constitutive model used in this study can be used for showing the

difference in mechanical behavior of DGA under compressive and tensile loading conditions, where the strength of DGA in compression is greater than that in tension.

Moreover, damage density, viscoelastic strain, and effective viscoplastic strain distributions for different compressive and tensile strains are presented in Figure V-25 to Figure V-30. Note that the selected strain levels for compressive strain rates are different from those for tensile strain because DGA was failed in less strain level, as shown in Figure V-24, and that all distribution at 0.5% and 0.6% are not shown for 1.97×10^{-5}/s tensile strain rate due to fast failure, where the strain level at failure was 0.4%. It is clearly shown that more damage density is observed as loading rate decreases because the induced stress in the mastic phase can relax slower with faster loading rates. In addition, as shown in Figure V-27 and Figure V-28, viscoelastic strain becomes more uniformly distributed as loading rate gets faster, and higher viscoplastic strain occurs as strain rates decreases.

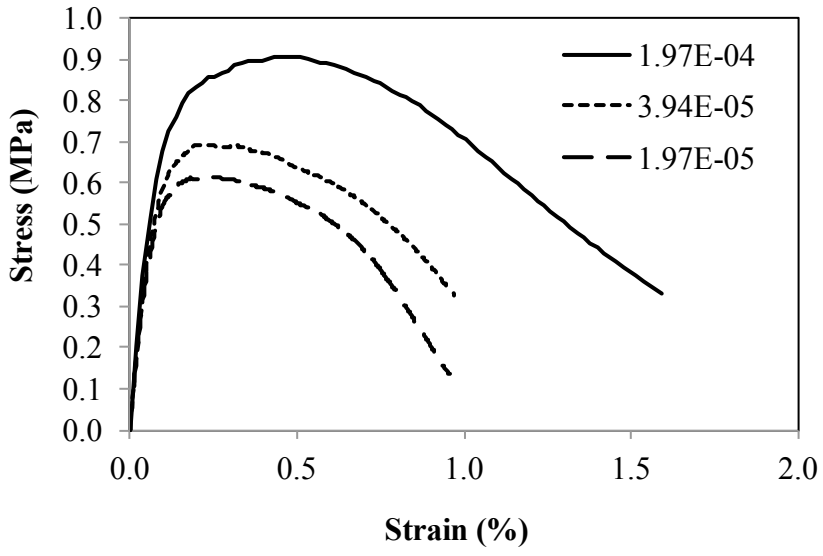

(a)

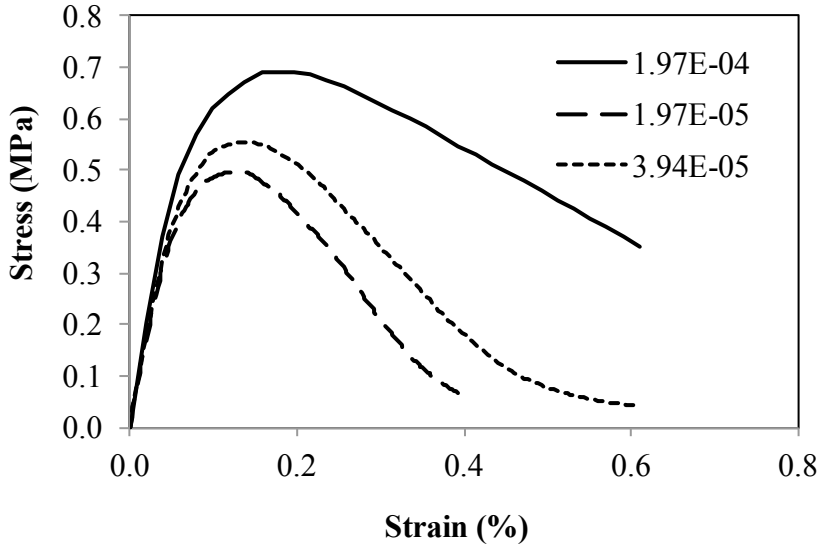

(b)

Figure V-24. Stress-strain responses at different strain rates at a temperature of 20 °C: (a) in compression and (b) tension.

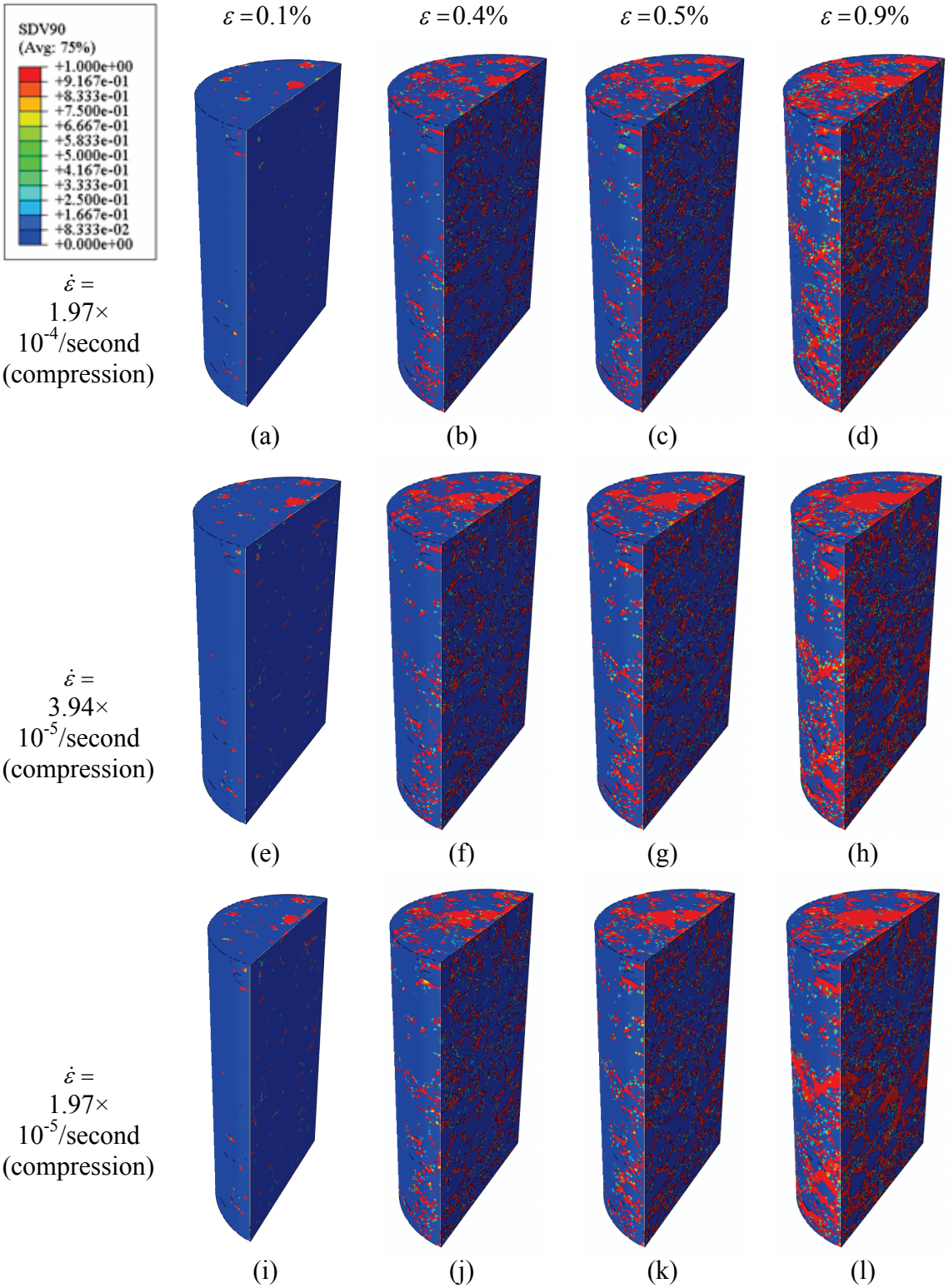

Figure V-25. Damage density distribution at four different strain levels for various compressive strain rates (a temperature of 20 °C).

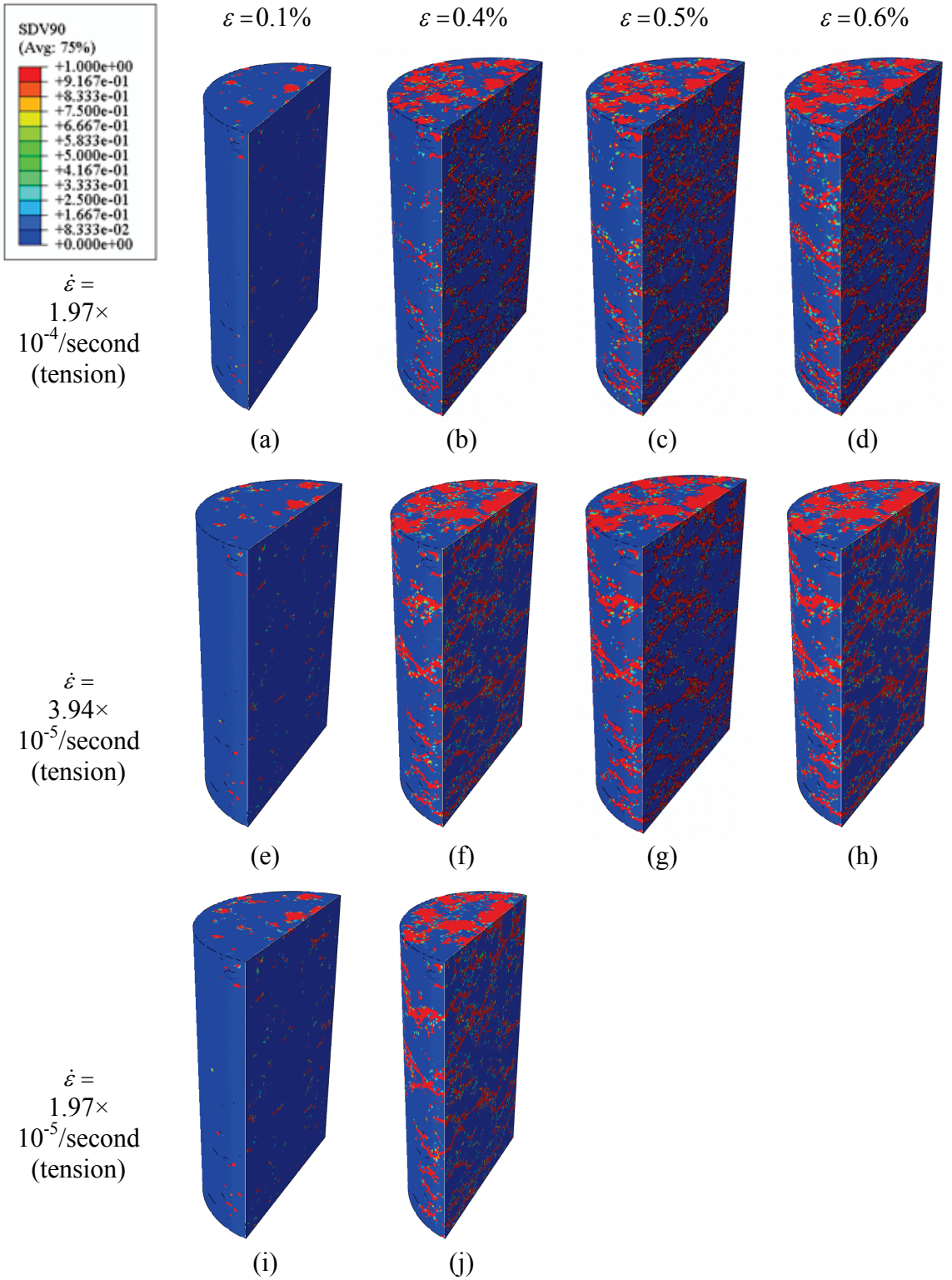

Figure V-26. Damage density distribution at four different strain levels for various tensile strain rates (a temperature of 20 °C).

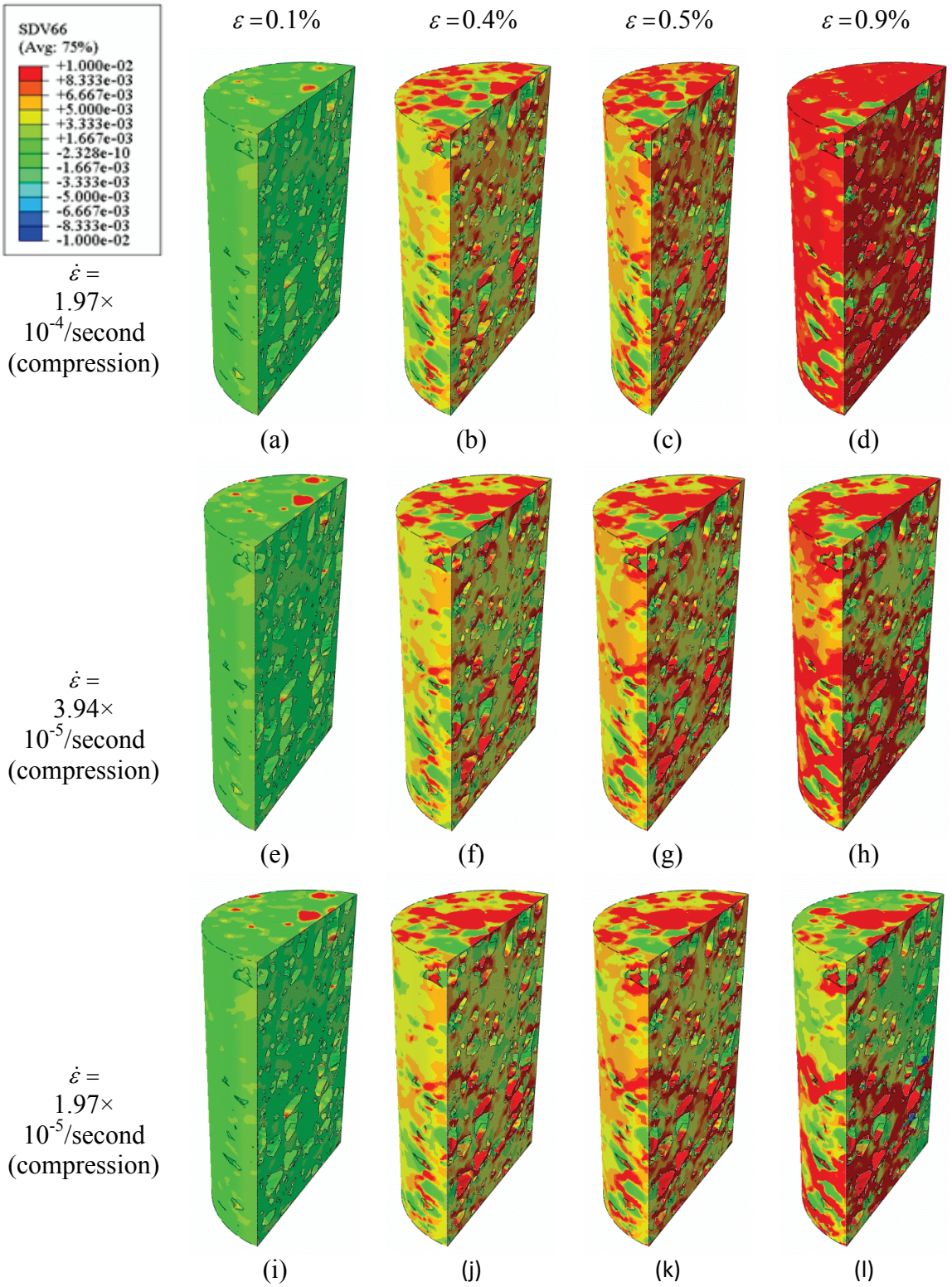

Figure V-27. Viscoelastic strain distribution at four different strain levels for various compressive strain rates (a temperature of 20 °C).

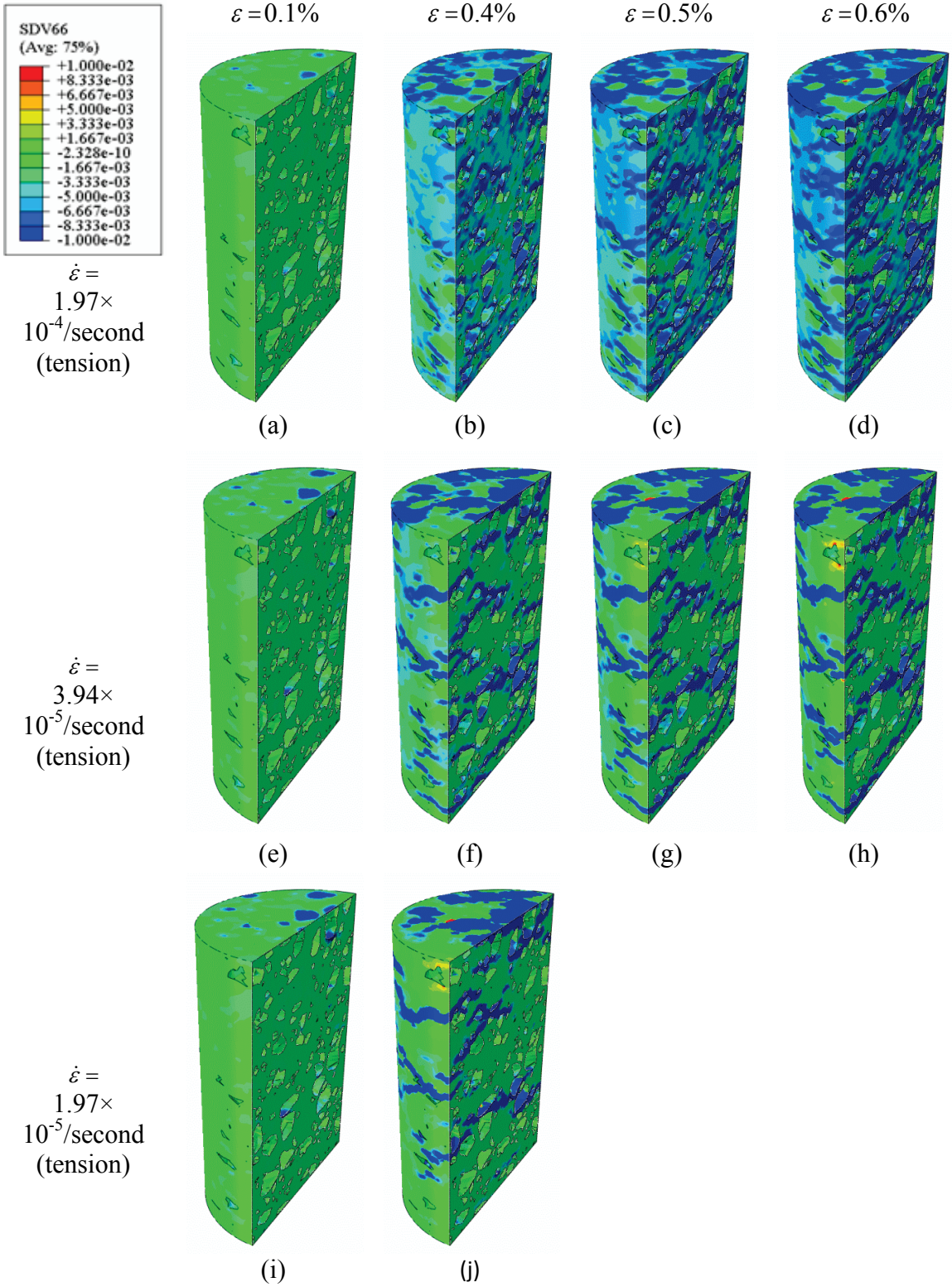

Figure V-28. Viscoelastic strain distribution at four different strain levels for various tensile strain rates (a temperature of 20 °C).

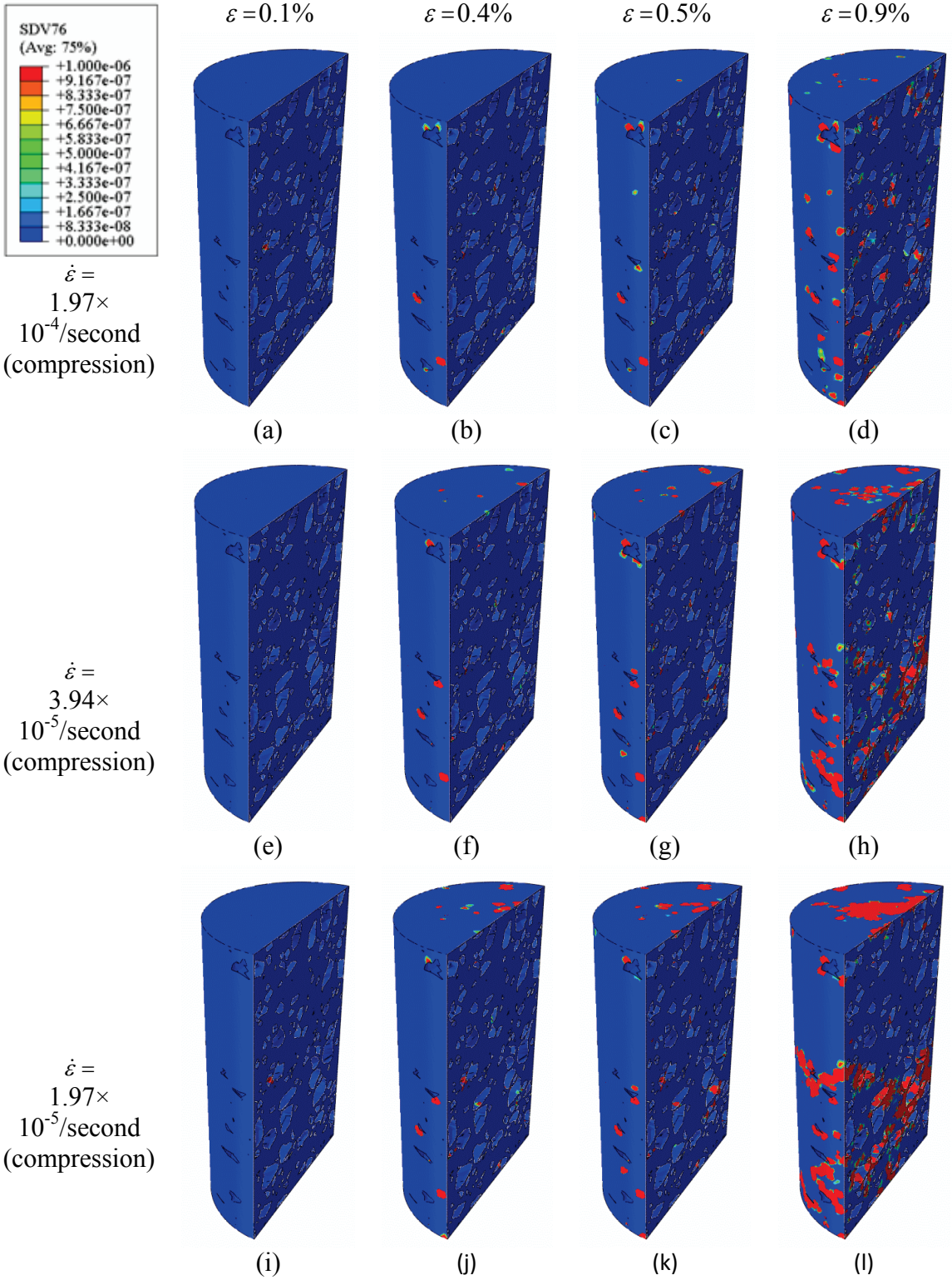

Figure V-29. Effective viscoplastic strain distribution at four different strain levels for various compressive strain rates (a temperature of 20 °C).

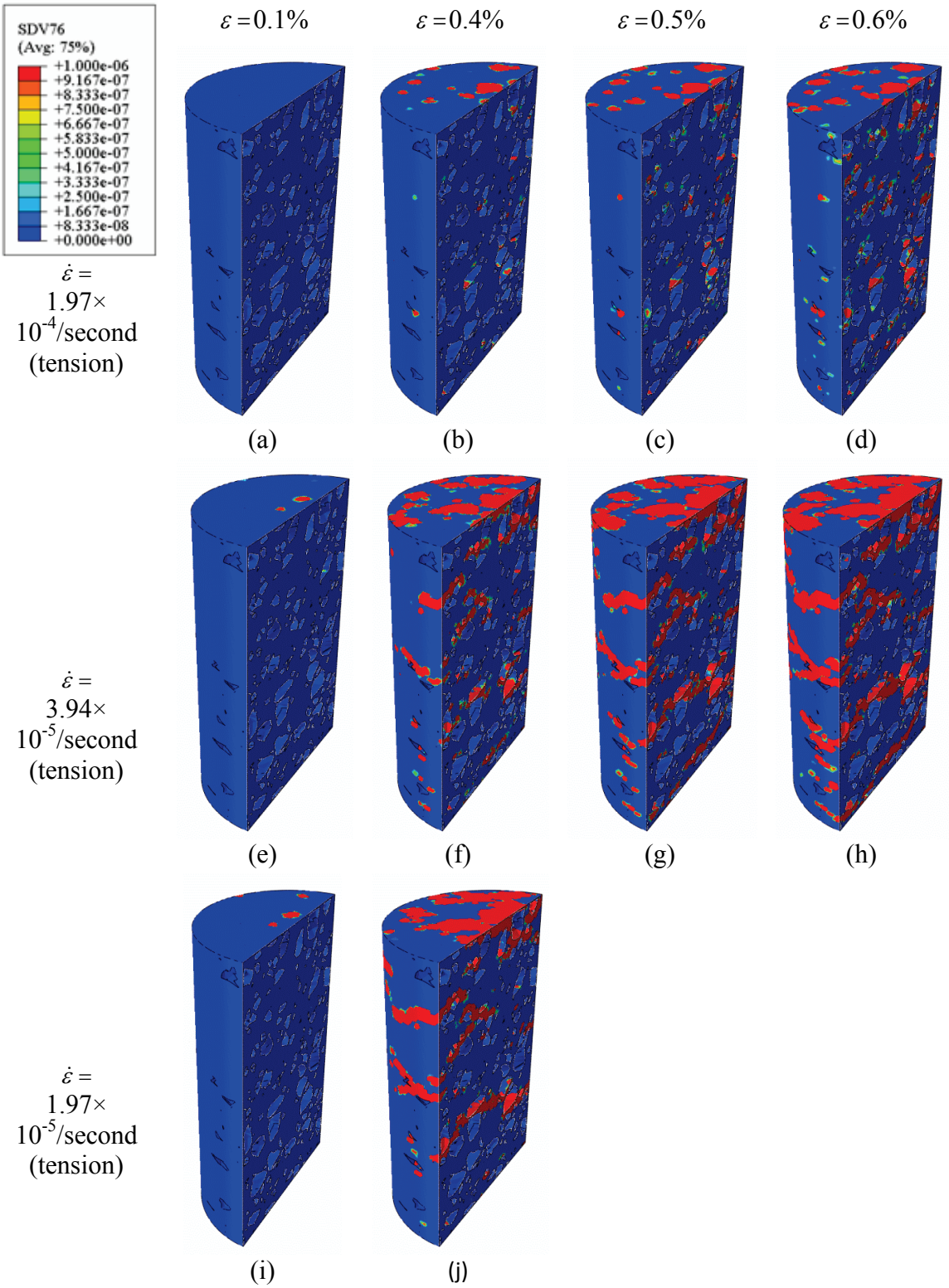

Figure V-30. Effective viscoplastic strain distribution at four different strain levels for various tensile strain rates (a temperature of 20 °C).

V.4.2 The Effect of Temperature

In order to investigate effect of temperatures on the response of DGA, uniaxial compressive tests were simulated at 1.97×10^{-4}/s at three temperatures: 10 °C, 20 °C, and 40 °C. Stress-strain responses are presented in Figure V-31. It is clearly shown that the overall response of DGA strongly depends on temperatures, as shown in Figure V-31. This figure also shows the ability of the current microstructure to consider the overall response of DGA at different temperatures. In particular, Figure V-31 shows that a combination of the current 3D microstructure and the thermo-viscoelastic, thermo-viscoplastic, and thermo-viscodamage constitutive model can be a useful and powerful tool to predict the effect of temperature on the mechanical behavior of DGA. The initial stiffness and ultimate strength decrease as temperature increases. Furthermore, the damage density, viscoelastic strain, and effective viscoplastic strain distributions at fixed strain levels including 0.1%, 0.4%, 0.5%, and 0.9% are shown in Figure V-32 to Figure V-34. Note that the aggregates, which are assumed to be elastic in this study, are removed in Figure V-33 and Figure V-34 to show the viscoelastic and viscoplastic strain distributions more clearly. It is presented that DGA at lower temperature is prone to be more damaged. However, more recoverable strain is shown as temperature increases, whereas less viscoplastic strain occurs in higher temperature because the material gets softer (weaker) due to more damage evolution as temperature decreases. It is noted that the sum of the viscoelastic and viscoplastic strains is equal to the total strain, and the distributions for the viscoelastic and viscoplastic strain at a fixed strain level are shown

in Figure V-34. Thus, it is reasonable that more viscoelastic and less viscoplastic strains at the fixed strain level are shown as temperature increases.

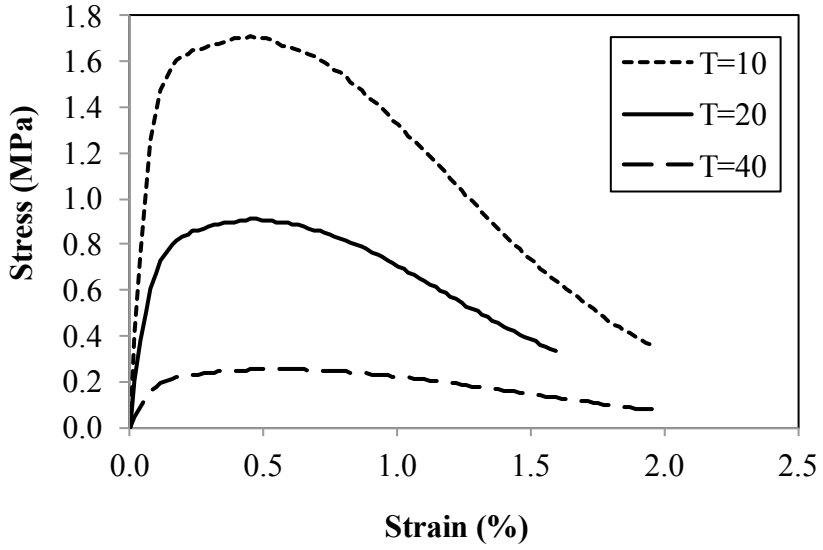

Figure V-31. Stress-strain responses at different temperatures under a compressive strain rate 1.97×10^{-4}/second.

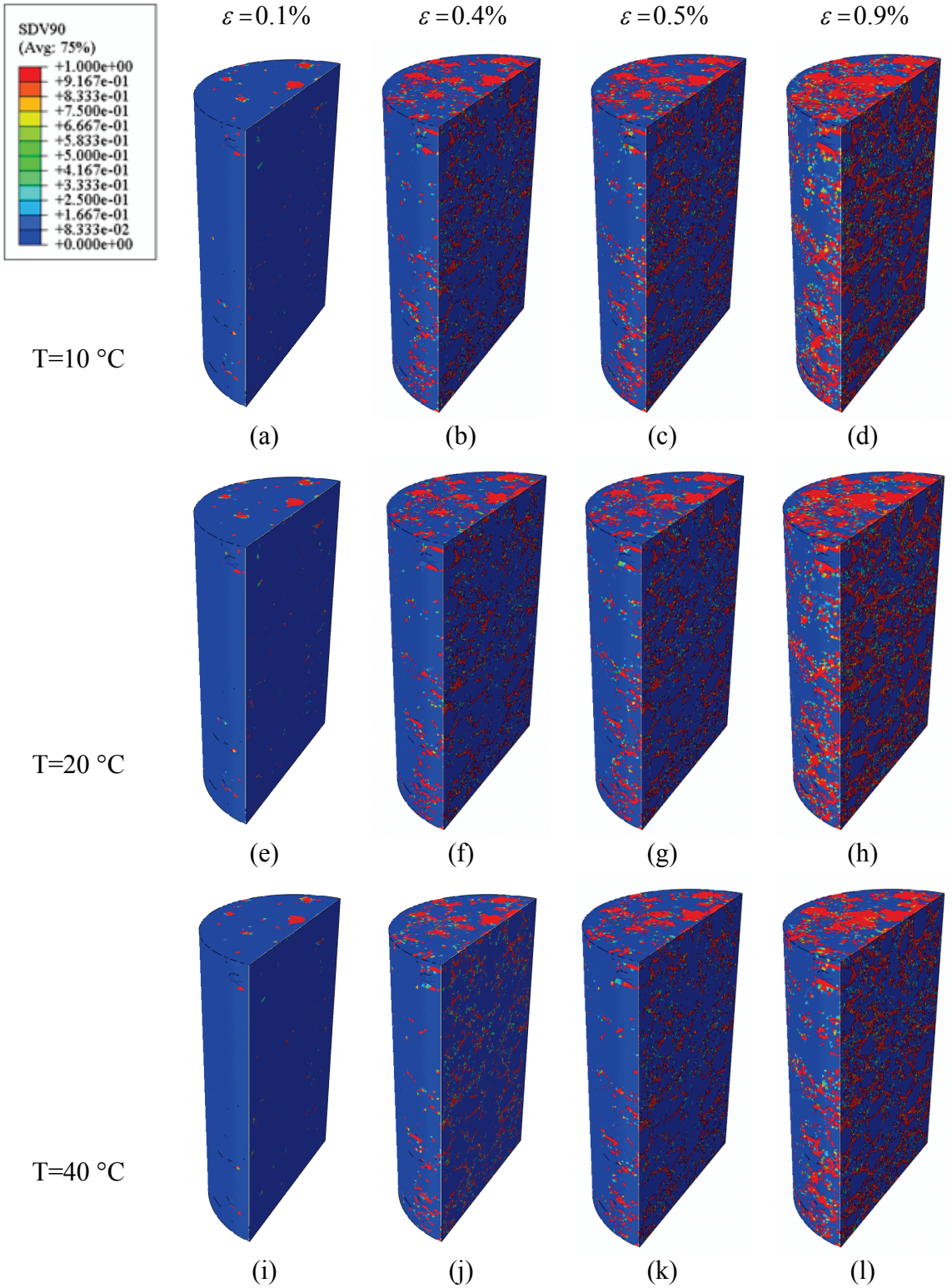

Figure V-32. Damage density distribution at four different strain levels for various temperatures (compressive strain rate 1.97×10^{-4}/second).

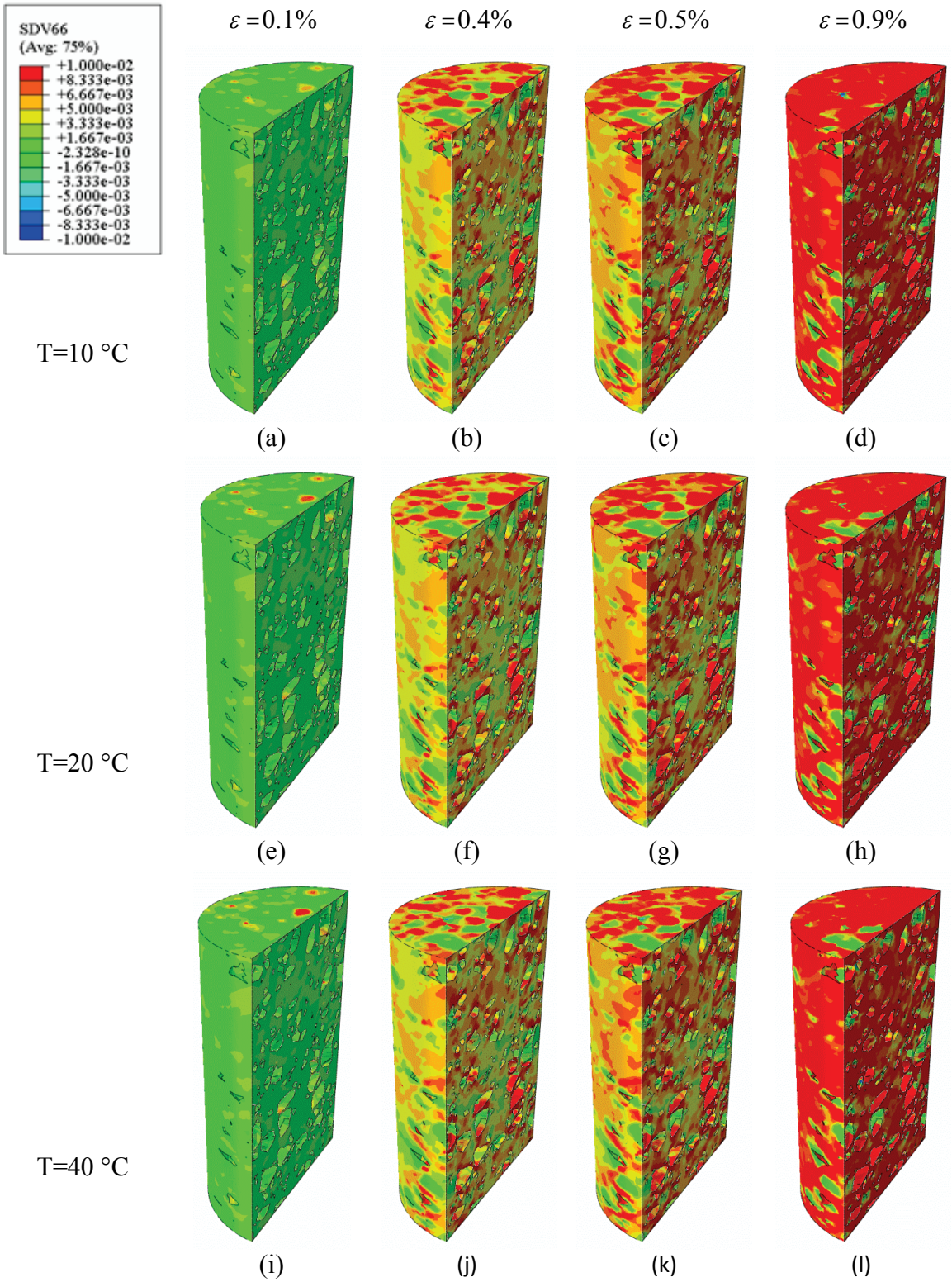

Figure V-33. Viscoelastic strain distribution at four different strain levels for various temperatures (compressive strain rate 1.97×10^{-4}/second).

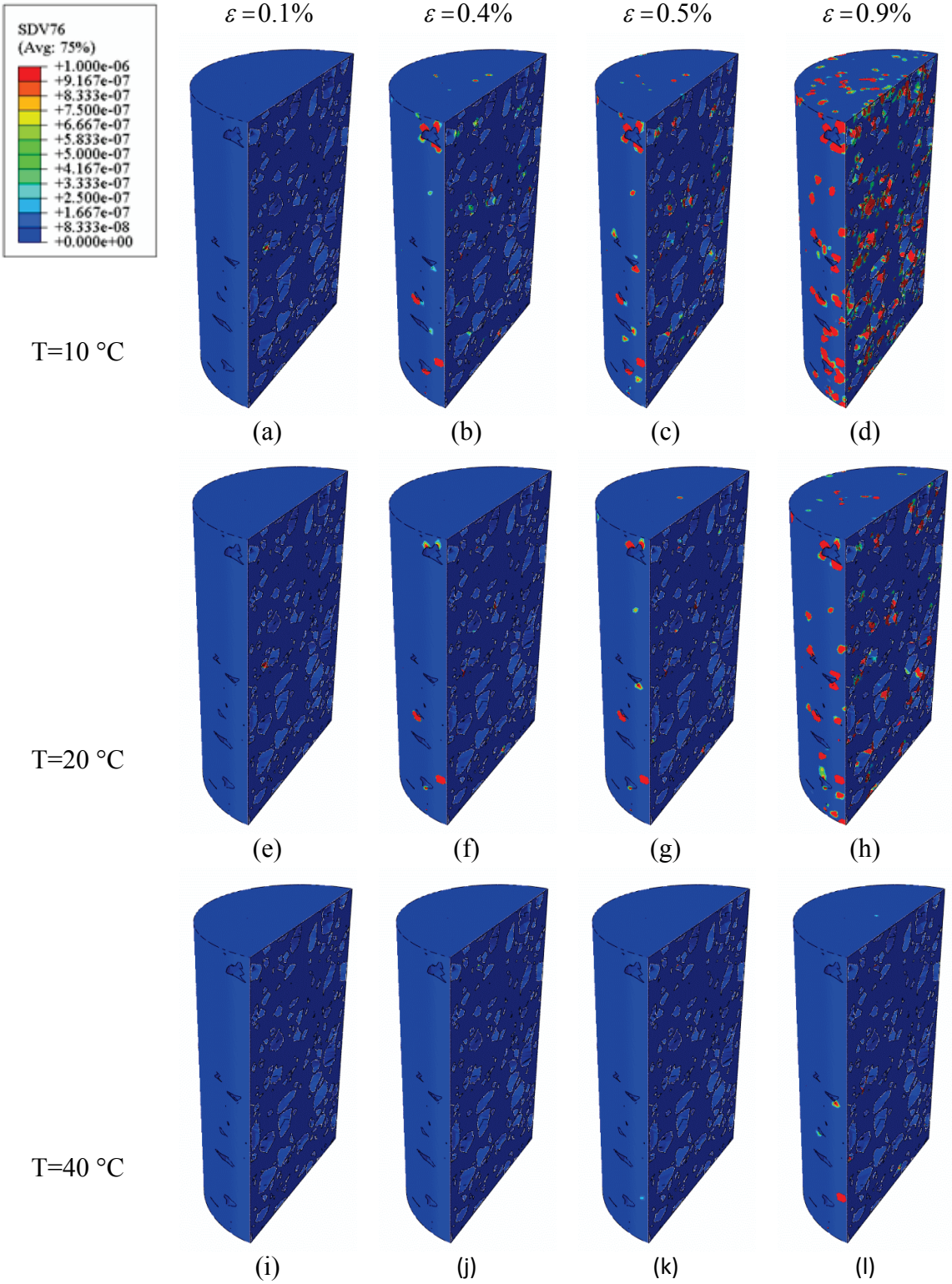

Figure V-34. Effective viscoplastic strain distribution at four different strain levels for various temperatures (compressive strain rate 1.97×10^{-4}/second).

V.4.3 The Effect of Loading Type

Cyclic loading-unloading condition is applied to the microstructure at a temperature of 20 °C. The applied stress has ten seconds of loading time and two seconds of unloading time. The effect of micro-healing during the rest period is not considered in this study [25, 61]. Damage density, viscoelastic strain, and effective viscoplastic strain distributions at different times are shown in Figure V-35. Damage initiates at the interface between aggregates and matrix and evolves as number of cycles increases, as shown in Figure V-35 (a) to (d). The viscoelastic strain distribution, presented in Figure V-35 (e) to (h), also occurs in a region between aggregates and matrix at low number of cycles and then distributes through the whole specimen. On the other hands, the effective viscoplastic strain started and accumulated in the top of the specimen, where loading is applied, and then it distributed through the whole specimen at its failure, as shown in Figure V-35 (i) to (l).

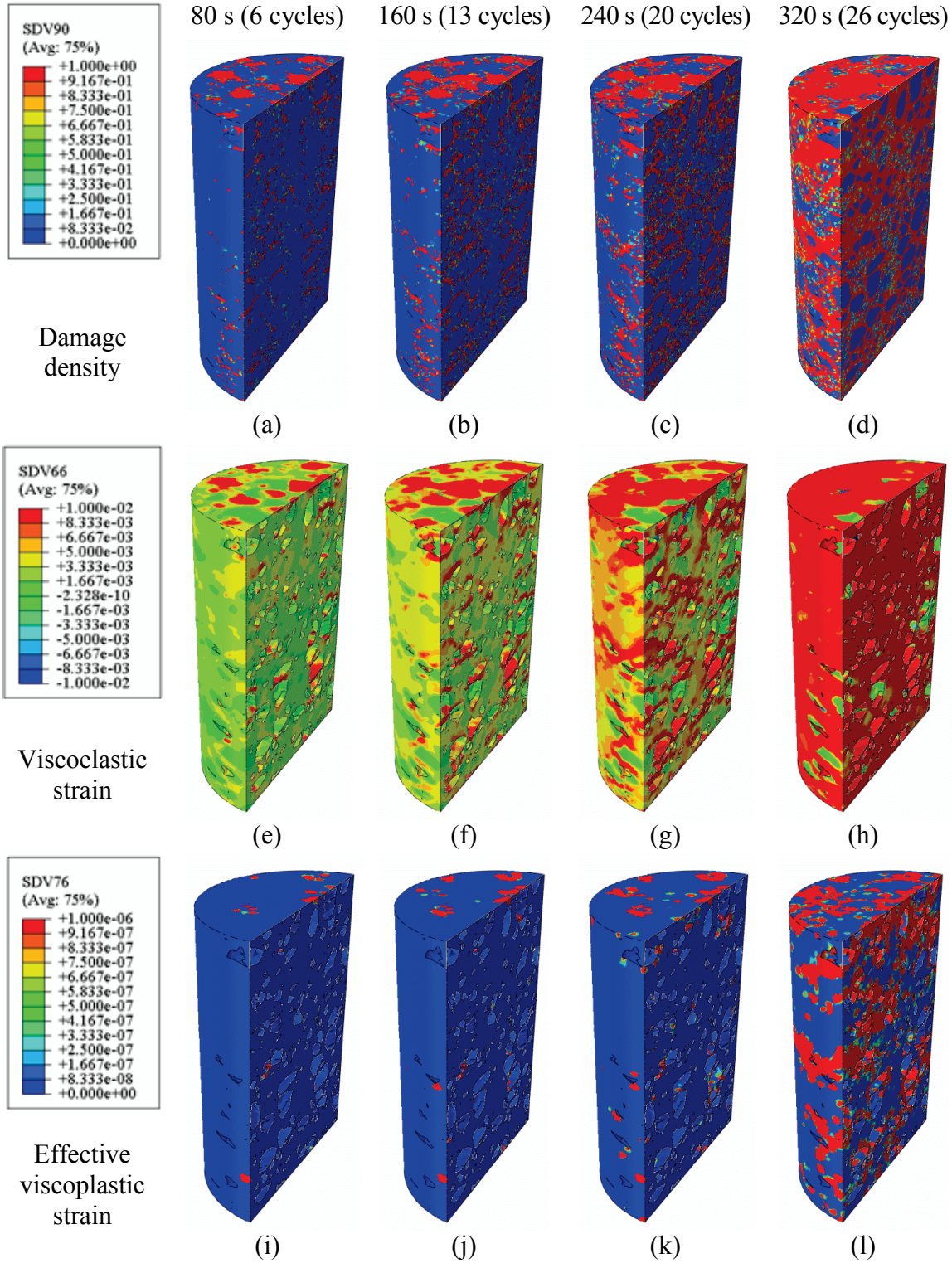

Figure V-35. Damage density, viscoelastic strain, and effective viscoplastic strain distributions of repeated creep-recovery test at different times (a temperature of 20 °C).

V.5 Effect of Mixture Design on Microscopic and Macroscopic Responses

The microscopic and macroscopic responses of the DGA are compared with the SMA. As shown in Figure V-36 to Figure V-38, it is clear that the SMA has a higher ultimate strength than the DGA. In addition, the DGA has more gradual reduction in strength after the point of ultimate strength than the SMA. This could be attributed to the fact that SMA relies primarily on stone-on-stone contacts to resist deformation, which leads to an increase in strength. This result is consistent with findings of previous studies by Gatchalian et al. [24] and Mahmoud et al. [28], which showed that aggregate particles in SMA are subjected to higher stresses than their counterparts in DGA with continuous gradation. These studies have shown that failure in SMA initiates as a result of the loss of shear strength at the particle contacts or because of the fracture of particles. In DGA with continuous gradation, however, failure occurs in the matrix phase surrounding the particles. This difference in the failure mechanism and its location could be the reason for the less ductile response of the SMA mixtures in the post-failure region.

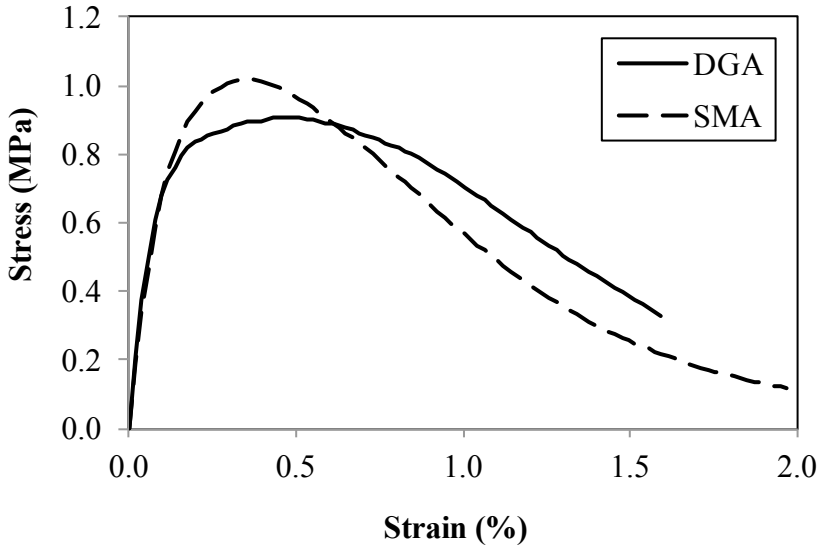

Figure V-36. Stress-strain responses of dense-graded asphalt concrete and stone matrix asphalt at 1.97×10^{-4} compressive strain rates at a temperature of 20 °C.

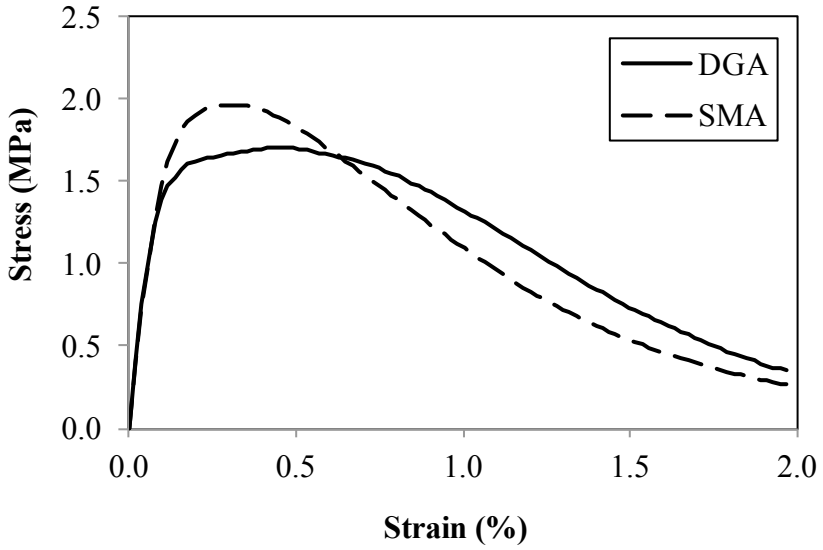

Figure V-37. Stress-strain responses of dense-graded asphalt concrete and stone matrix asphalt at 1.97×10^{-4} compressive strain rates at a temperature of 10 °C.

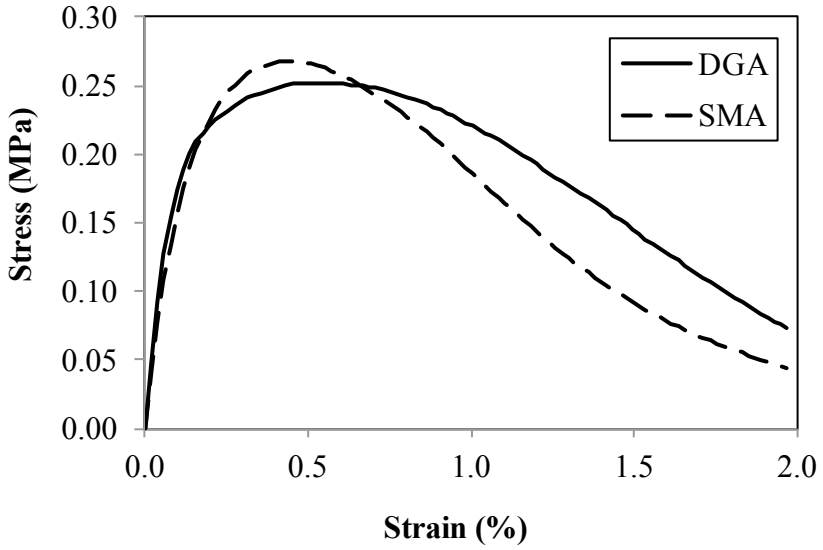

Figure V-38. Stress-strain responses of dense-graded asphalt concrete and stone matrix asphalt at 1.97×10^{-4} compressive strain rates at a temperature of 40 °C.

Damage density distributions of SMA at different temperatures are presented in Figure V-39. SMA has less damage density in the all three temperatures than the DGA as shown in Figure V-32. It is interesting to note that more localized damage occurs in SMA, which again, resists deformation primarily by the shear strength at regions of particle contacts.

The viscoplastic and viscoelastic strain distributions in SMA and DGA microstructures were also compared. A representative example of the results for viscoelastic strain at 20 °C is shown in Figure V-40 and Figure V-41. As expected, the results show that the strain magnitudes in the microstructure increase with an increase in the applied macroscopic strain. Overall, the strain distributions in SMA and DGA are similar, but the SMA has a slightly higher percentage of the high strain values than

DGA. The same finding applies for the viscoplastic strain. These results along with the stress-strain diagrams in Figure V-36 to Figure V-38 confirm that SMA mixtures can sustain higher strain values in the microstructure and achieve a higher ultimate macroscopic strength than DGA.

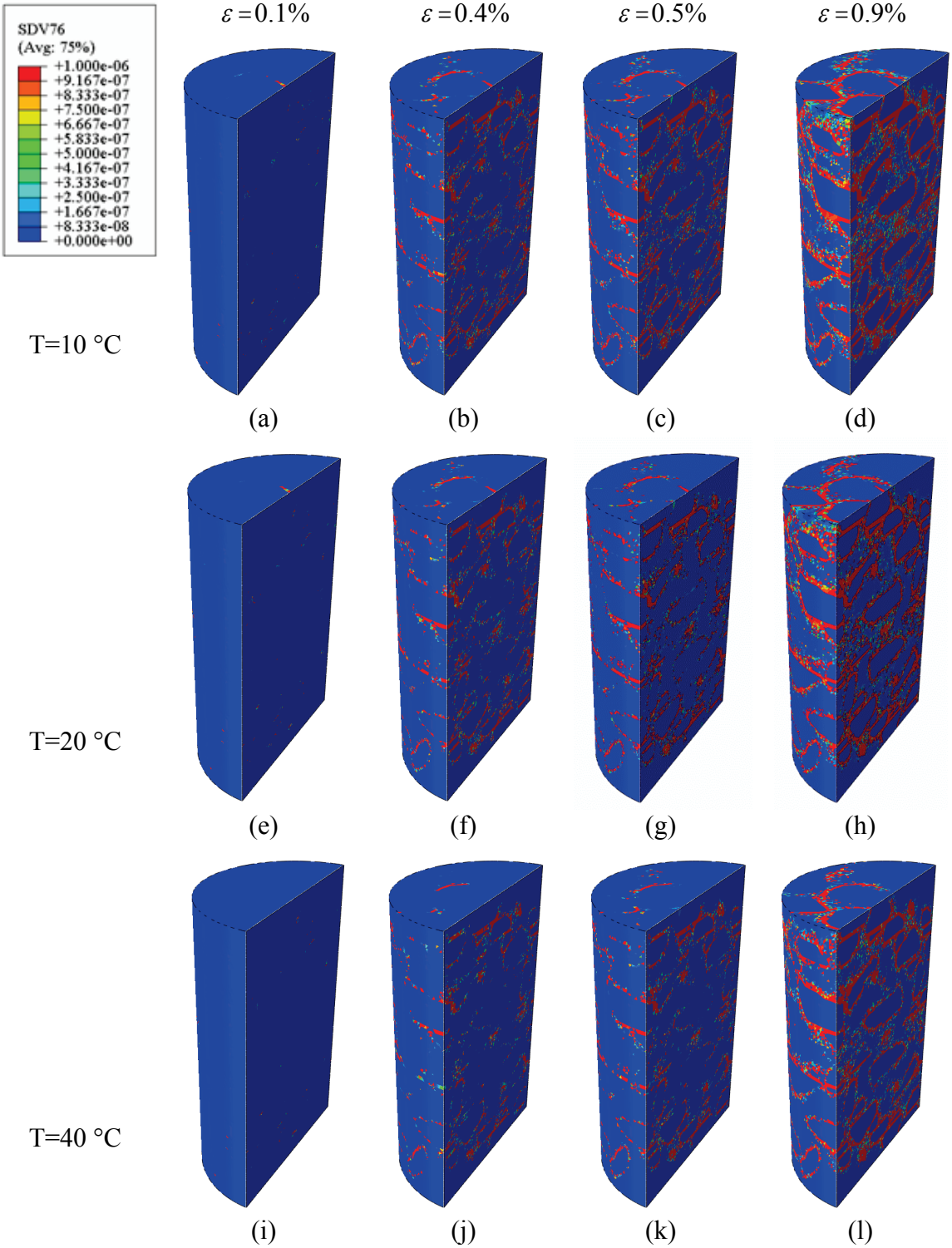

Figure V-39. Damage density distribution of stone matrix asphalt (SMA) at four different strain levels for various temperatures (compressive strain rate 1.97×10^{-4}/second).

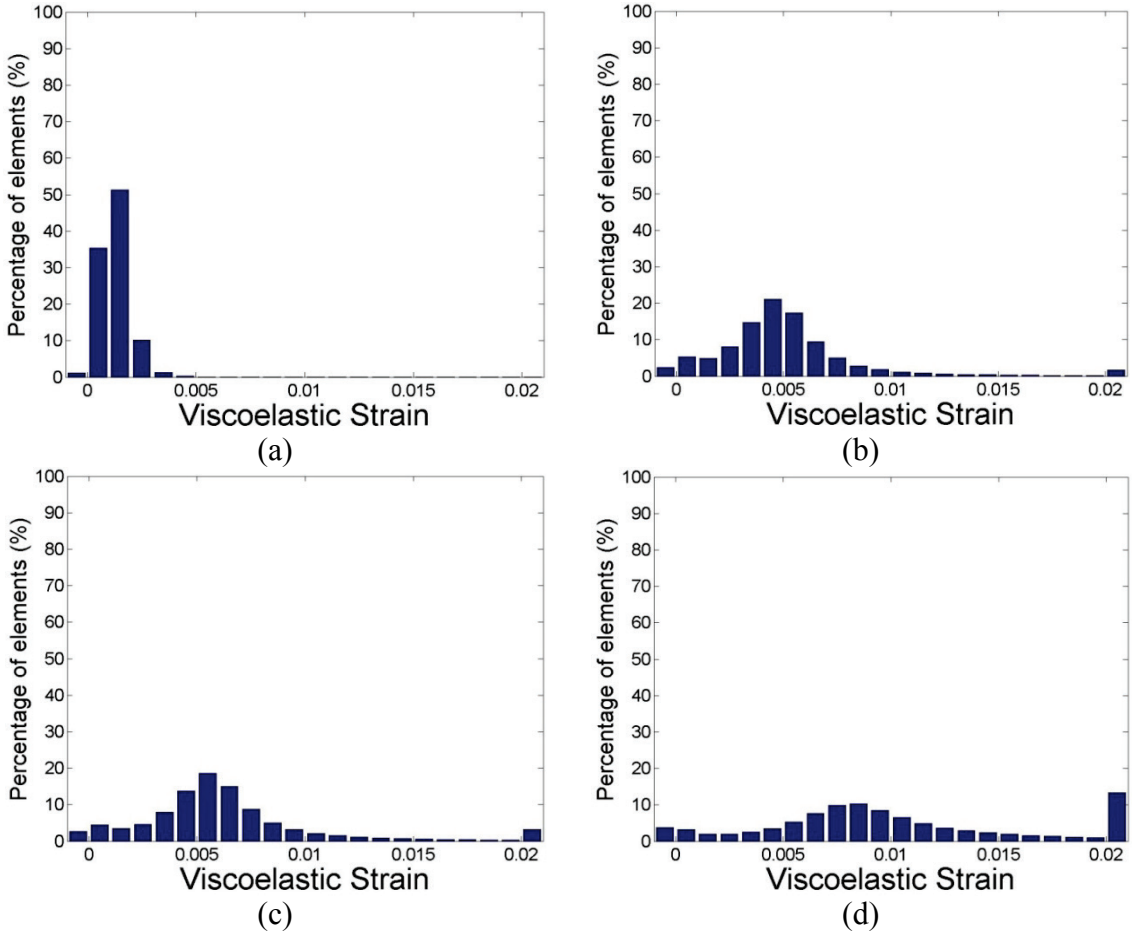

Figure V-40. Viscoelastic strain histogram of dense-graded asphalt concrete at four different strain levels for T=20 °C (compressive strain rate 1.97×10^{-4}/second): (a) $\varepsilon=0.1\%$, (b) $\varepsilon=0.4\%$, (c) $\varepsilon=0.5\%$, and (d) $\varepsilon=0.9\%$.

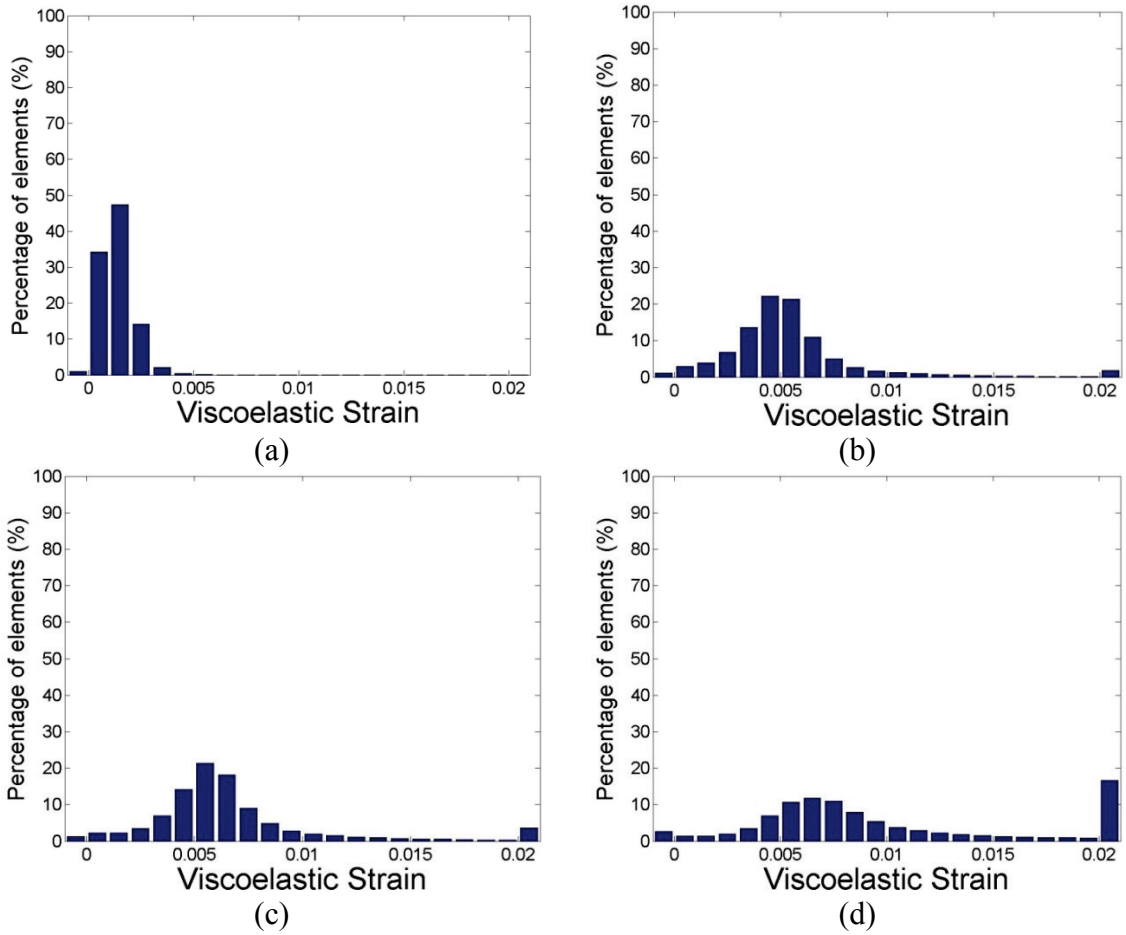

Figure V-41. Viscoelastic strain histogram of stone matrix asphalt (SMA) at four different strain levels for T=20 °C (compressive strain rate 1.97×10^{-4}/second): (a) $\varepsilon=0.1\%$, (b) $\varepsilon=0.4\%$, (c) $\varepsilon=0.5\%$, and (d) $\varepsilon=0.9\%$.

V.6 Conclusions

The microstructure-based computational framework presented in this chapter employs the capabilities of X-ray CT in capturing realistic 3D microstructure and a unified coupled nonlinear-thermo-viscoelastic, thermo-viscoplastic, and thermo-viscodamage constitutive model. The X-ray CT images were processed using various imaging filters and segmentation techniques to better identify and model the mixture components. The

rate-, time-, and temperature-dependent responses of asphalt concrete were simulated successfully in this study. The results showed that asphalt concrete was stronger and more brittle at faster loading rates and lower temperatures. In addition, asphalt concrete was stronger in compression than in tension. Damage density distribution of the 3D microstructure showed that asphalt concrete is more prone to damage at faster loading rates and lower temperatures. Finally, the comparison of the macroscopic and microscopic responses of DGA with continuous gradation and SMA provided insight on the failure mechanisms in these mixtures and on the ability of SMA to sustain more loads.

The results demonstrated that the presented framework including the 3D image-based microstructure and the coupled thermo-viscoelastic, thermo-viscoplastic, and thermo-viscodamage model can be used to predict the macroscopic thermo-mechanical response of asphalt concrete under various loading conditions and temperature. It allows conducting 'virtual experiments' to save lots of resources and efforts in performing macroscopic experimental tests. Moreover, this framework can be utilized to investigate the mechanical responses of different types of asphalt concrete and to understand the microscopic behavior of asphalt concrete and find the relationship between microscopic and macroscopic responses. The current proposed framework can be applied in guiding to design microstructures of asphalt concrete in order to obtain the desired macroscopic response.

CHAPTER VI

CALIBRATION AND VALIDATION OF THE CONSTITUTIVE MODEL USING FINE AGGREGATE MIXTURES AND FULL MIXTURES

VI.1 Introduction

This chapter presents the laboratory testing methods needed for calibration and validation of the constitutive model discussed in chapter III. Several experimental tests that include dynamic modulus test, repeated creep-recovery test, and constant strain rate test are required for calibration and validation of the model using FAM and full asphalt mixture. The dynamic modulus test is conducted to identify the linear viscoelastic model parameters, while the repeated creep-recovery tests are performed to identify the nonlinear viscoelastic and viscoplastic parameters. The viscodamage model parameters are identified using the experimental results from the constant strain rate test.

The identified model parameters for FAM and full mixture are used to simulate the repeated creep-recovery tests with various resting time at different temperatures. Theses simulation results are compared to the corresponding experimental tests for validating the model parameters for the constitutive model.

VI.2 Materials

The FAM consists of an asphalt binder mixed with fine portion of aggregate gradation passing No. 16 (1.18 mm). Figure VI-1 shows the aggregate gradation of the full mixture and FAM. In this study, limestone and unmodified binder PG 67-22 were used to prepare the full mixture and FAM test specimens. The aggregate blend for the full

mixture includes 30% Type C rock, 36% Type F rock, 24% washed screening, and 10% of manufactured sand. Theses rock designations refer to size distribution following the specifications of the Texas Department of Transportation (TxDOT).

The full mixture has a nominal maximum aggregate size of 19.0 mm and a binder content of 4.4%. The aggregate gradation and binder content of the FAM was determined according to the procedure by Sousa et al. [62] to represent the mastic phase of the full mixture. The binder content of the FAM was 8% and the FAM aggregate gradation is given in Figure VI-1.

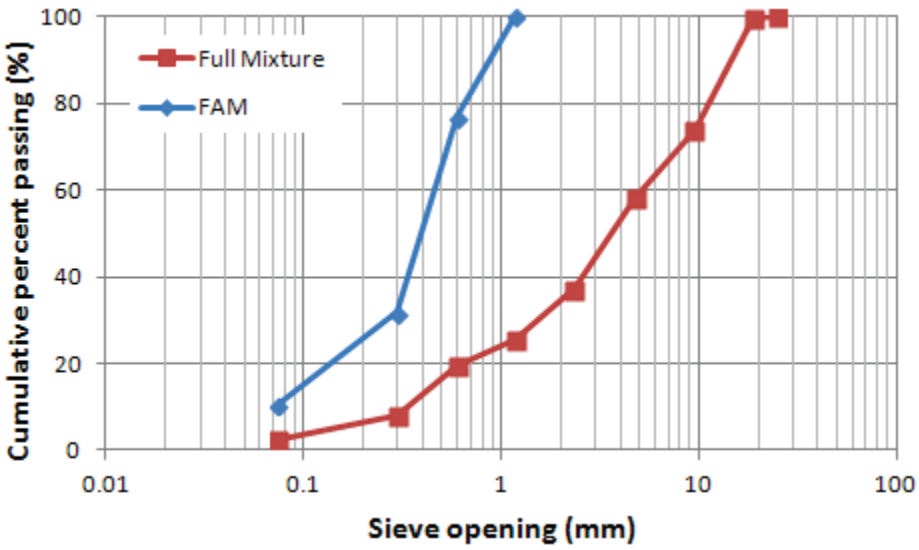

Figure VI-1. Aggregate gradation of full mixture and FAM.

Cylindrical laboratory test specimens of the FAM and full mixture were prepared using a Superpave gyratory compactor (SGC). The SGC was used to compact 6-inch (150 mm) diameter by 7-inch (175 mm) height specimens. Then, the SGC specimens

were cored and cut to 4-inch (100 mm) diameter by 6-inch (150 mm) height. Figure VI-2 shows test specimens prepared using the full mixture and FAM. The test specimen of full mixture and FAM had average percent air voids of 7.0±0.5%.

(a) (b)

Figure VI-2. (a) Full asphalt mixture and (b) FAM.

VI.3 Testing Methods

The researchers conducted several tests to determine the material parameters needed for the calibration and validation of different components of the constitutive model. The dynamic modulus test was used to identify the linear viscoelastic model parameters and the time-temperature shift factors. The repeated creep-recovery test at variable stress level was used to identify the viscoplastic model parameters. The uniaxial constant strain rate test in tension was used to determine the viscodamage model parameters. The

repeated creep-recovery test at constant loading and resting times was used to validate the model.

Table VI-1 summarizes the test methods required to determine the model parameters for the full mixture and FAM. The following section discusses the testing protocols with more details.

Table VI-1. Testing matrix of full mixture and FAM.

Mixture	Test Mode	Total No. of Specimens	Test Method	Temperature (°C)	Level	Confinement stress (kPa)	LT/RT* (sec)
Full Mixture	Compression	2	TP-62	Various	80-110με	0	N/A
		2	RCRT-VS	55	Various	70	0.4/30
		6	RCRT-CLR	40	840	140	0.4/0.4
							0.4/2.0
							0.4/5.0
		6	RCRT-CLR	55	840	140	0.4/0.4
							0.4/1.0
							0.4/5.0
	Tension	6	Uniaxial constant strain rate test	5	5E-5/sec	0	N/A
					1E-5/sec		
					5E-6/sec		
FAM	Compression	2	TP-62	Various	80-110με	0	N/A
		2	RCRT-VS	40	Various	70	0.4/30
		6	RCRT-CLR	40	630	70	0.4/0.4
							0.4/2.0
							0.4/5.0
	Tension	6	Uniaxial constant strain rate test	5	2E-4/sec	0	N/A
					1E-4/sec		
					2E-5/sec		

* LT=Loading time, RT=Resting time.

VI.3.1 Dynamic Modulus Test

The dynamic modulus test was conducted in accordance with the AASHTO TP-62 [63] at five temperatures (-10 °C, 4 °C, 21 °C, 38 °C, and 54 °C) and six frequencies (0.1 Hz, 0.5 Hz, 1 Hz, 5 Hz, 10 Hz, and 25 Hz). Testing started from the lowest to highest

temperature and from the highest to the lowest frequency. A sinusoidal loading was applied and adjusted to obtain axial strain between 80 to 100 microstrain in order to remain within the linear viscoelastic region and prevent any damage for the material. The applied stress and recorded strain were used to calculate the dynamic modulus and phase angle. Figure VI-3 shows a test specimen and testing setup for the dynamic modulus test. Three axial linear variable differential transformers (LVDTs) and three radial LVDTs were used to measure the deformation during testing.

Figure VI-3. The setup used in the dynamic modulus test.

VI.3.2 Repeated Creep-recovery Tests at Variable Stress Level

The repeated creep-recovery test at variable stress levels (RCRT-VS) was conducted to identify the viscoplastic model parameters. Table VI-1 summarized the RCRT-VS test parameters used in full mixture and FAM testing. The test included six loading blocks.

Each loading block consisted of eight creep-recovery cycles with increasing applied deviatoric stress level. The loading time and resting times of each loading cycle remained constant through the entire test. The loading time was 0.4 sec, while the unloading time was 30 sec. The deviatoric stress of the first loading cycle of the first loading block was 140 kPa and it increased by a factor of $1.2^{(n-1)}$, where n is the number of loading cycle in a specific loading block, for the next loading cycles until the 8^{th} loading cycle. The first deviatoric stress of the subsequent loading blocks equaled to the third stress level in the previous loading block, and it increased by the same factor of $1.2^{(n-1)}$ for the next loading cycles until the 8^{th} loading cycle of the loading block. A confining pressure of 70 kPa was maintained during the entire test. Figure VI-4 shows an example for the first three loading blocks of the RCRT-VS. The axial and radial deformations were measured using the linear variable differential transformers. Three axial LVDTs were used to measure axial deformation. The LVDTs were placed on the test specimens at 120 degree apart. A schematic view of the test setup with mounted axial LVDTs was given in Figure VI-5. Three LVDTs were employed to measure the radial deformation at the center of the test specimens. Figure VI-5 shows the used tri-axial with "through-the-wall" radial LVDTs.

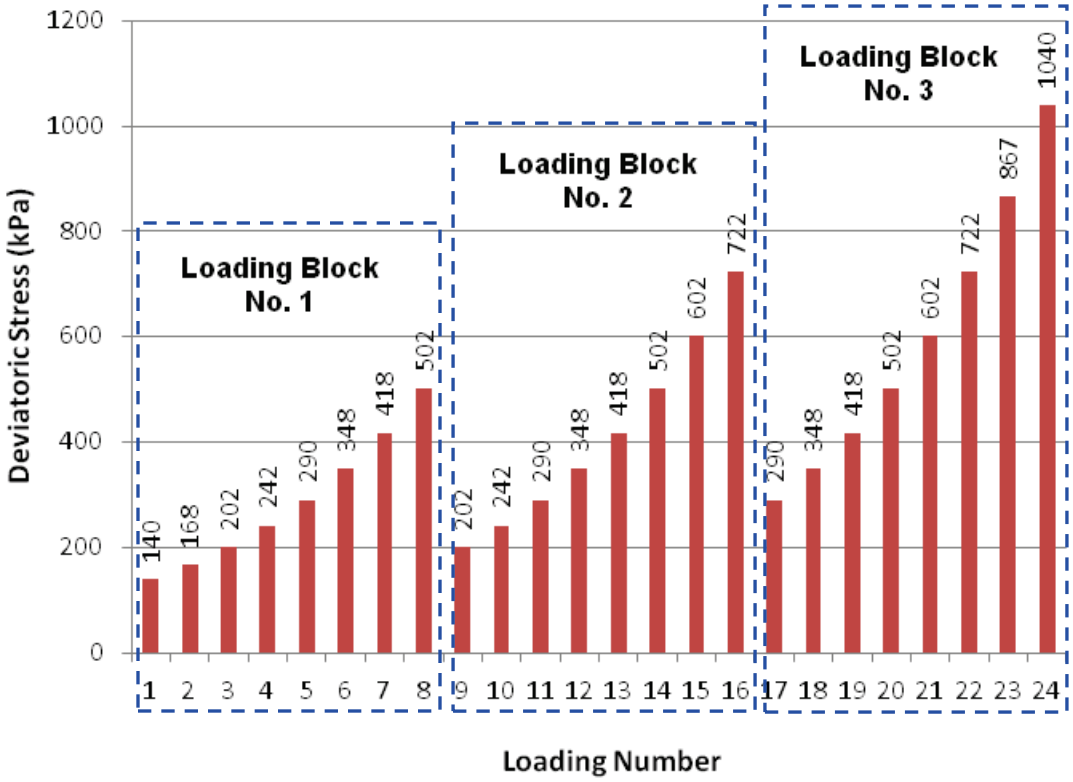

Figure VI-4. Applied deviatoric stress in the first three blocks of the RCRT-VS.

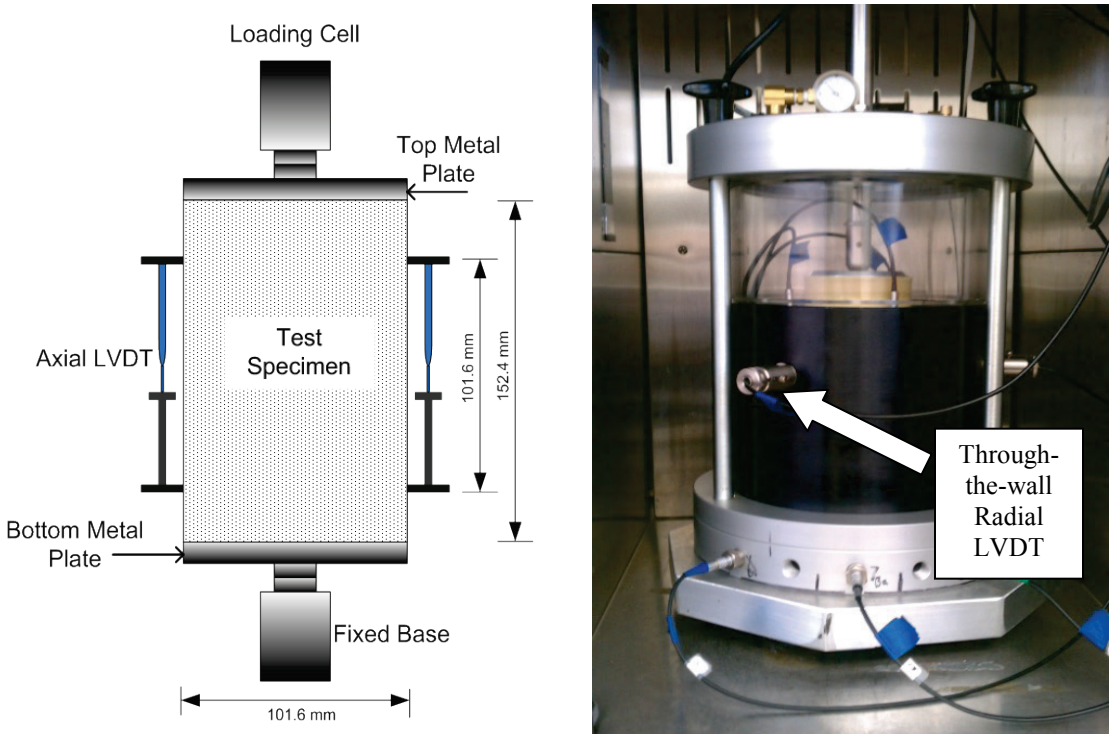

(a) (b)

Figure VI-5. (a) Schematic of test specimen with mounted axial LVDTs and (b) triaxial cell inside a temperature-controlled chamber.

VI.3.3 Repeated Creep-recovery Tests at Constant Loading and Resting Times

The creep-recovery test at constant loading and resting times (RCRT-CLR) was performed in this study to validate the model. The RCRT-CLR consisted of repeated creep-recovery loading cycles.

Table VI-1 summarized the RCRT-CLR test parameters used in full mixture and FAM testing. The loading time and resting period of all loading cycles were maintained constant through the entire test. Two specimens were tested at each resting period as given in Table VI-1. Figure VI-6 illustrates a schematic for the RCRT-CLR test.

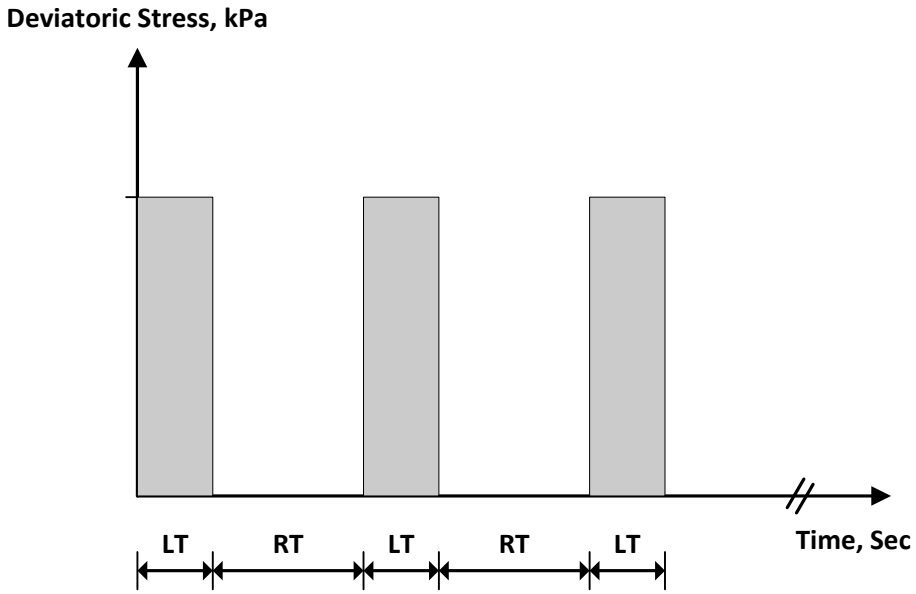

Figure VI-6. Schematic for loading cycles of RCRT-CLR (LT is loading time and RT is resting time).

VI.3.4 Constant Tensile Strain Rate Test

The uniaxial constant tensile strain rate tests (CTSR) was conducted to identify the viscodamage model parameters. The test was conducted at 5 °C at three different tensile strain rates, as given in Table VI-1. Figure VI-7 shows testing setup. Three axial LVDTs were used to measure the axial deformation, while one circumferential LVDT was used to measure the radial deformation. The circumferential LVDT was found to provide consistent reading compared to the average of three radial LVDTs in tension.

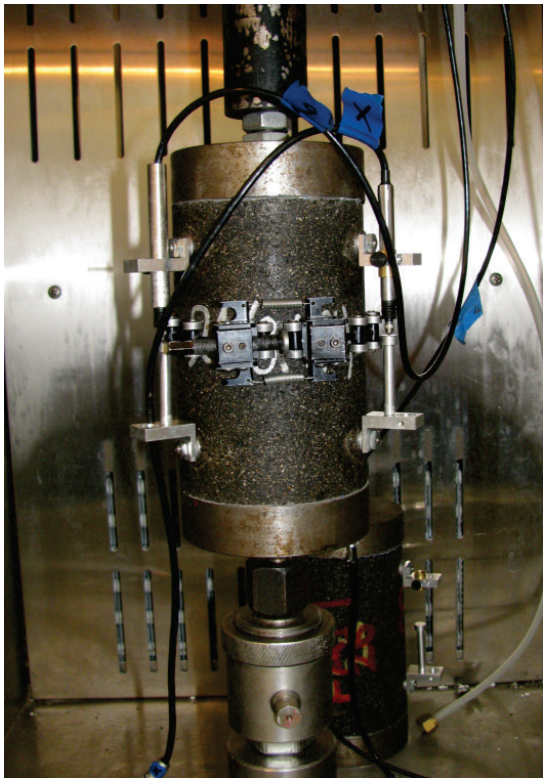

Figure VI-7. Testing setup for CTSR.

VI.4 Identification of Material Properties

VI.4.1 Identification of Viscoelastic Parameters

Firstly, it should be noted that the procedure used to identify the material parameters for the constitutive model for the full asphalt mixture is the same procedure for the FAM. The dynamic modulus test was used to identify the material parameters for the viscoelastic model. Figure VI-9 (a) shows the experimental measurements of the dynamic modulus for the full mixture, while Figure VI-9 (b) shows the dynamic modulus data of the FAM. The time-temperature shift factors are obtained by minimizing the error between the experimental measurements and the sigmoidal function using the generalized reduced gradient algorithm, to build the master curve for

the complex compliance (D^*). Generally, the sigmoidal function [64] can be expressed as follows:

$$S(t) = \frac{1}{1+\exp(-t)} \tag{6.1}$$

where *S(t)* is the sigmoidal function and *t* is a variable, and it is shown in Figure VI-8.

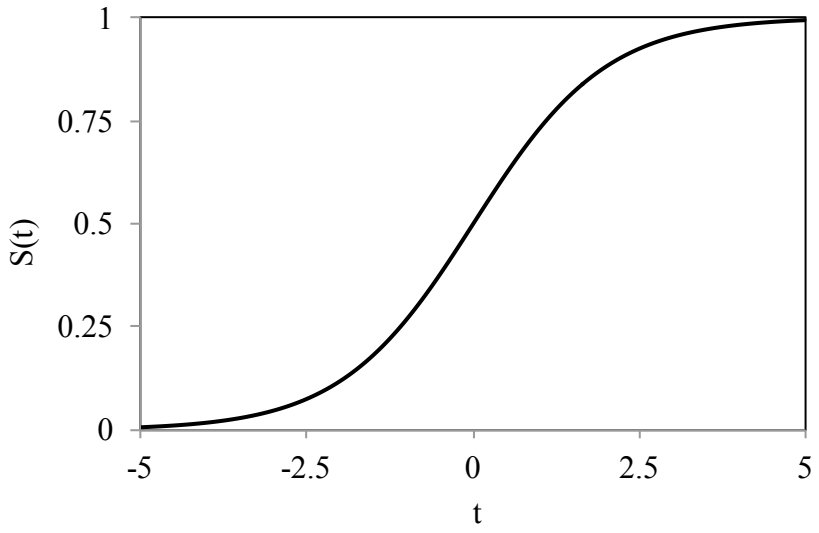

Figure VI-8. Sigmoidal function.

The identified time-temperature shift factors for various temperatures are presented Table VI-2 and the master curve for the complex compliance (D^*) is shown in Figure VI-9 (b). Once the complex compliance data at different temperatures are shifted by the time-temperature shift factors, the Prony series coefficients (D_n and λ_n) in Eq. (3.5) can be identified by minimizing the error between the storage compliance (D') and loss

compliance (D'') from experiment and prediction, where D' and D'' are calculated as follows [65]:

$$\text{(Experiment)} \quad D' = \left\|D^*\right\|\cos\theta; \qquad D'' = \left\|D^*\right\|\sin\theta$$

$$\text{(Prediction)} \quad D' = D_0 + \sum_{n=1}^{N} \frac{D_n}{1+\left(\omega/\lambda_n\right)^2}; \quad D'' = D_0 + \sum_{n=1}^{N}\left[\frac{1}{\lambda_n}\frac{D_n}{1+\left(\omega/\lambda_n\right)^2}\right]^2 \tag{6.2}$$

Figure VI-10 shows that there is a strong agreement in the storage and loss compliances from the experiment and predictions. The model parameters D_n and λ_n at the reference temperature of 21 °C are presented in Table VI-2. The storage and loss compliances of full asphalt mixture from experiment also agree with the ones from prediction and the identified Prony's coefficients (D_n and λ_n) are summarized in Table VI-4.

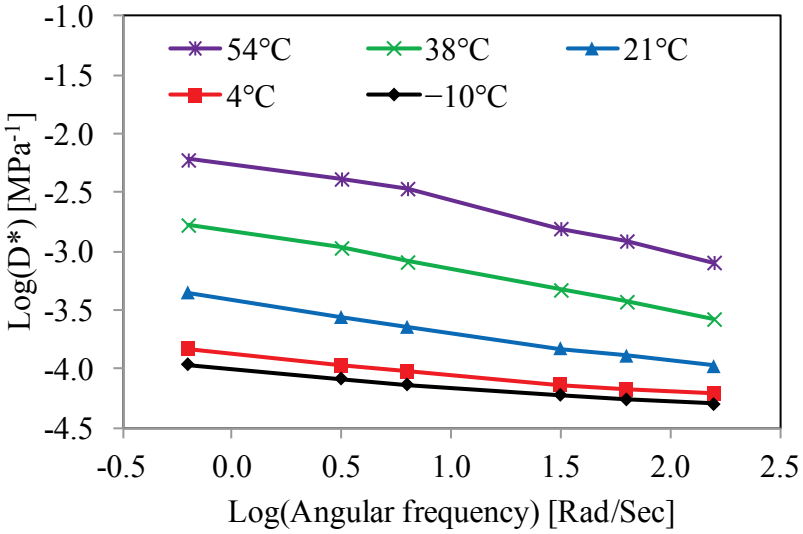

(a)

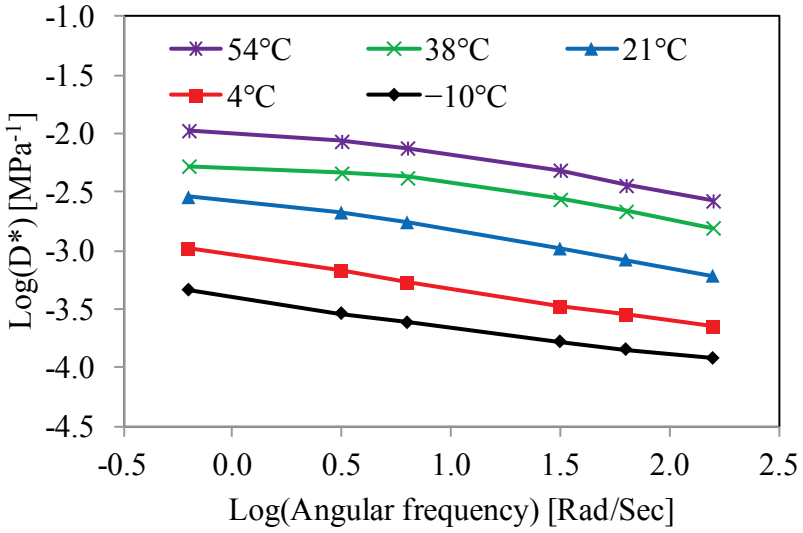

(b)

Figure VI-9. (a) Complex compliance data for full mixture at different temperatures, (b) complex compliance data for FAM at different temperatures, and (c) master curves for the complex compliance at 21 °C built using time-temperature shift factors.

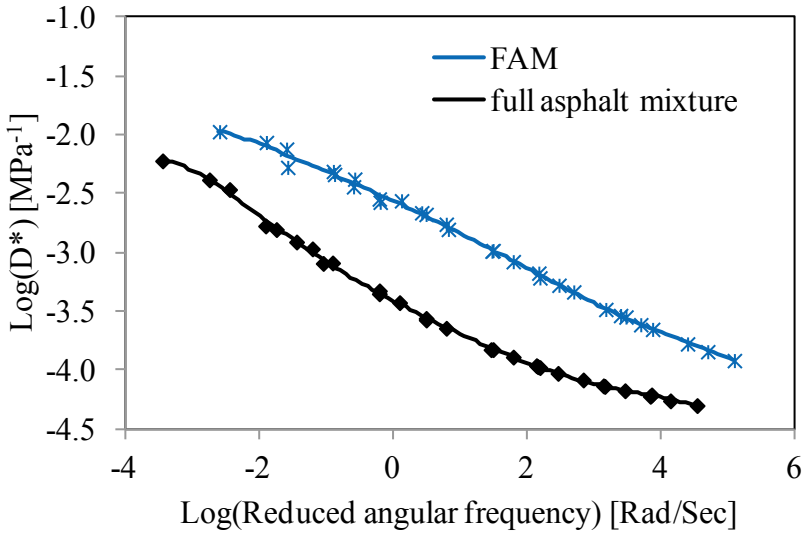

(c)

Figure VI-9 Continued.

Table VI-2. List of material parameters for FAM at 21 °C.

Viscoelastic model (Prony Series) parameters						
n		λ_n (Sec^{-1})		D_n (MPa^{-1})		D_0 (MPa^{-1})
1		1.00×10^{5}		3.85×10^{-5}		
2		1.00×10^{4}		9.58×10^{-5}		
3		1.00×10^{3}		2.11×10^{-4}		
4		1.00×10^{2}		4.31×10^{-4}		
5		1.00×10^{1}		7.94×10^{-4}		1.07×10^{-4}
6		1.00×10^{0}		1.29×10^{-3}		
7		1.00×10^{-1}		1.88×10^{-3}		
8		1.00×10^{-2}		2.47×10^{-3}		
9		1.00×10^{-3}		3.56×10^{-3}		
Viscoplastic model parameters						
α	β	Γ_0^{vp} (sec^{-1})	N	κ_0 (kPa)	κ_1 (kPa)	κ_2
0.25	0.20	4.32×10^{-5}	1.98	43.32	600.00	437.00
Time-temperature shift factor (a_T)						
$T=5°C$	$T=19°C$	$T=21°C$	$T=40°C$	$T=55°C$		
41.918	1.591	1.000	0.0306	0.0038		
Viscodamage model parameter						
Γ_0^{vd} (Sec^{-1})		Y_0 (kPa)		q		k
2.95×10^{-20}		1000		6.34		-6.30

Table VI-3. List of material parameters for full asphalt mixture at 21 °C.

Viscoelastic model (Prony Series) parameters						
n	λ_n (Sec^{-1})		D_n (MPa^{-1})		D_0 (MPa^{-1})	
1	1.00×10^{4}		1.31×10^{-5}			
2	1.00×10^{3}		2.07×10^{-5}			
3	1.00×10^{2}		4.86×10^{-5}			
4	1.00×10^{1}		1.03×10^{-4}			
5	1.00×10^{0}		2.32×10^{-4}		5.16×10^{-5}	
6	1.00×10^{-1}		5.27×10^{-4}			
7	1.00×10^{-2}		1.16×10^{-3}			
8	1.00×10^{-3}		2.56×10^{-3}			
9	1.00×10^{-4}		5.42×10^{-3}			
Viscoplastic model parameters						
α	β	Γ_0^{vp} (sec^{-1})	N	κ_0 (kPa)	κ_1 (kPa)	κ_2
0.25	0.20	7.54×10^{-6}	2.78	94.69	1800.00	207.00
Time-temperature shift factor (a_T)						
$T = 5°C$	$T = 19°C$	$T = 21°C$	$T = 40°C$	$T = 55°C$		
24.294	1.701	1.000	0.0171	0.0004		
Viscodamage model parameter						
Γ_0^{vd} (Sec^{-1})	Y_0 (kPa)		q	k		
8.95×10^{-21}	1000		4.61	-5.02		

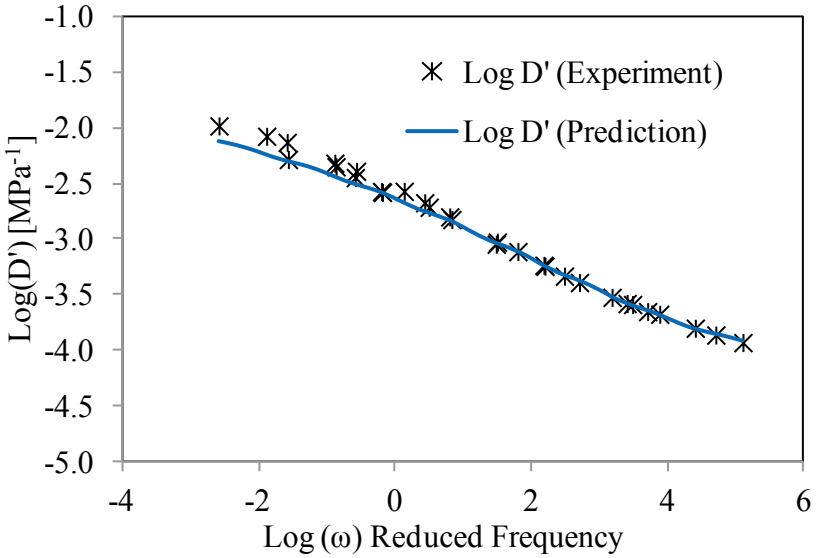

(a)

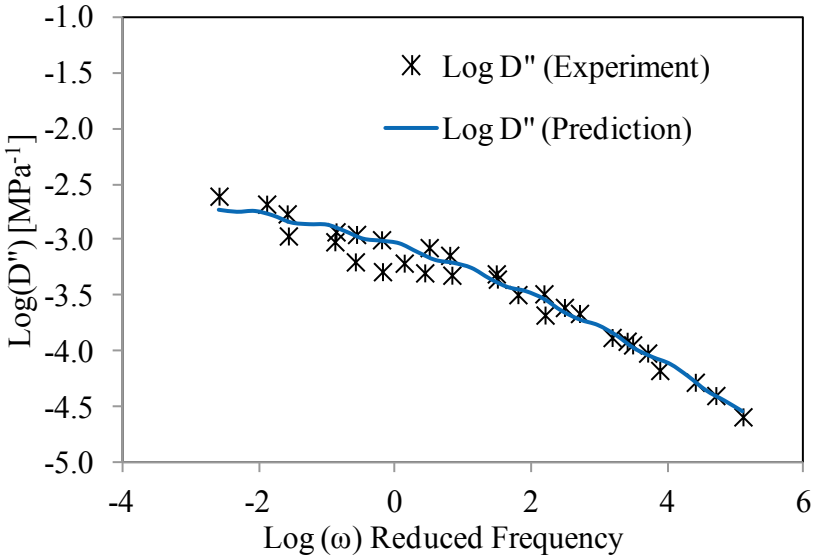

(b)

Figure VI-10. Comparison between experiment and prediction for (a) storage compliance (D') and (b) loss compliance (D'') for FAM.

Schapery's nonlinear viscoelasticity theory [4] is employed to model the viscoelastic component such that for one-dimensional problems one can write

$$\varepsilon^{ve,t} = g_0 D_0 \bar{\sigma}^t + g_1 \int_0^t \Delta D^{\left(\psi^t - \psi^\tau\right)} \frac{d\left(g_2 \bar{\sigma}^t\right)}{d\tau} d\tau \tag{6.3}$$

Once the Prony's coefficients are obtained, it is necessary to identify the nonlinear viscoelastic parameters such as g_0, g_1, g_2 in Eq. (3.3) by conducting the repeated creep-recovery test at variable stress levels. It is noted that g_0 is assumed to be unity here because the g_0 affects the instantneous response of asphalt concrete and does not have an important role in the transient and recovery behaviors [48]. Recently, Rahmani et al. [66] proposed a power law type function to relate the nonlinear viscoelastic parameters with a triaxiality ratio (η), expressed as:

$$g_i\left(\eta\right) = a_i \eta^{b_i} + c_i;\ i = 1,\ 2 \tag{6.4}$$

This triaxiality ratio can be defined in terms of the hydrostatic pressure (i.e., mean stress) and the von Misses equivalent stress and is written by:

$$\eta = \frac{I_1 / 3}{\sqrt{3J_2}} \tag{6.5}$$

where I_1 and J_2 are the first stress invariant and the second deviatoric stress invariant, respectively. Figure VI-11 shows the nonlinear parameters obtained from the experimental tests and the predicted values using Eq. (6.4) with respect to the triaxiality. Moreover, the identified constants in Eq. (6.4) for g_1 and g_2 are listed in Table VI-4.

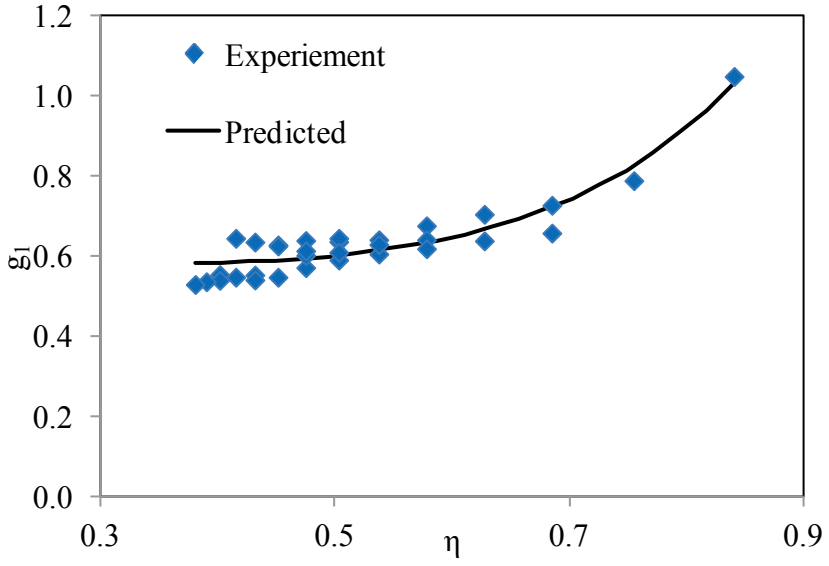

(a)

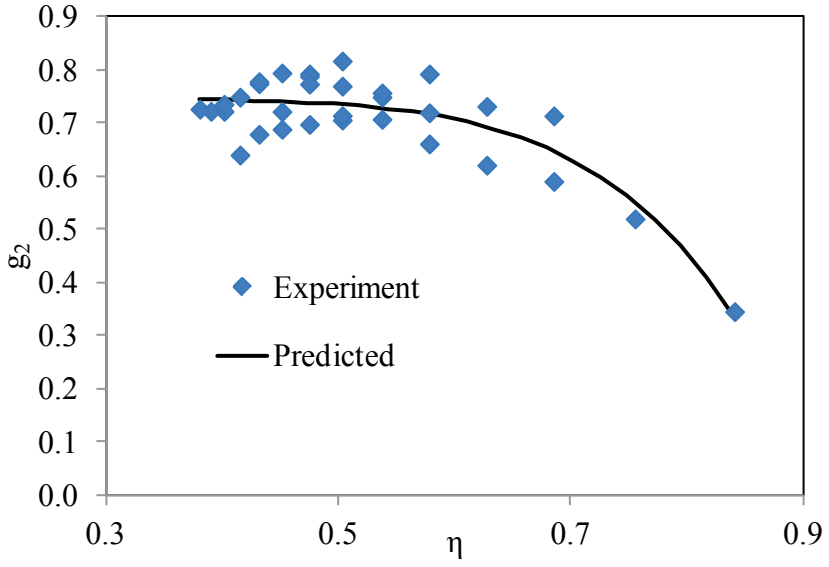

(b)

Figure VI-11. Comparison between experiment and prediction for the nonlinear viscoelastic parameters: (a) g_1 and (b) g_2 for FAM.

Table VI-4. Constants for nonlinear viscoelastic parameter g_i for FAM and full asphalt mixture.

FAM			
i	a_i	b_i	c_i
1	1.17	5.47	0.58
2	-1.39	7.00	0.75
Full asphalt mixture			
i	a_i	b_i	c_i
1	1.84	9.37	1.36
2	-0.85	14.60	0.29

VI.4.2 Identification of Viscoplastic Parameters

In order to identify the viscoplastic model parameters, the repeated creep-recovery tests at variable stress levels were conducted. The viscoplastic strain is extracted by subtracting the viscoelastic strain from the experimental total strain, as shown in Figure VI-12. The viscoelastic strain can be calculated by the viscoelastic parameters obtained as described above. The viscoplastic dynamic yield surface is derived by Eqs. (3.14) to (3.17), and written by;

$$\chi^{vp} = \overline{\tau} - \alpha \overline{I}_1 - \kappa_0 - \kappa_1 \left[1 - \exp\left(-\kappa_2 p\right)\right] - \sigma_y^0 \left(\frac{\dot{\gamma}^{vp}}{\Gamma^{vp}} \right)^{1/N} \cong 0 \tag{6.6}$$

Rearranging Eq. (6.6) gives:

$$\frac{\Delta \gamma^{vp}}{\Delta t} = \Gamma^{vp} \left\{ \frac{\overline{\tau} - \alpha \overline{I}_1 - \kappa_0 - \kappa_1 \left[1 - \exp\left(-\kappa_2 p\right)\right]}{\sigma_y^0} \right\}^N \tag{6.7}$$

where $\Delta \gamma^{vp}$ can be calculated by:

$$\Delta\gamma^{vp} = \frac{\Delta\varepsilon_1^{vp,t}}{\partial g / \partial \sigma_1} = \frac{\Delta\varepsilon_1^{vp,t}}{\left(1 - \beta/3\right)} \tag{6.8}$$

In this study, it is noted that α and β are assumed to be 0.25 and 0.20, respectively. The $\Delta\gamma^{vp}/\Delta t$ for the eight stress levels of the first block of the RCRT-VS test are shown in Figure VI-13. By selecting a specific level of $\Delta\gamma^{vp}/\Delta t$, the times for each stress level are found, and then the viscoplastic strains (ε_1^{vp}) corresponded the times are determined. The effective viscoplastic strain can be calculated by:

$$p = \left(\sqrt{1 + 2\left(\frac{0.5 + \beta/3}{1 - \beta/3} \right)^2} \right)^{-1} \sqrt{\left(\varepsilon_1^{vp}\right)^2 + \left(\varepsilon_2^{vp}\right)^2} \tag{6.9}$$

where $\varepsilon_2^{vp} = \frac{0.5 + \beta/3}{1 - \beta/3}\varepsilon_1^{vp}$. Rearranging Eq. (6.7) provides:

$$\overline{\tau} - \alpha \overline{I}_1 = C - \kappa_1 \exp\left(-\kappa_2 p\right) \tag{6.10}$$

where $C = \sigma_y^0 \left(\frac{\Delta\gamma^{vp}}{\Delta t \Gamma^{vp}} \right)^{1/N} + \kappa_0 + \kappa_1$. As shown in Figure VI-14, $\left(\tau - \alpha I_1\right)$ and p can be plotted for the selected level of $\Delta\gamma^{vp}/\Delta t$ at the eight stress levels. Therefore, κ_1 and κ_2 can be identified by minimizing the error between the experimental data and the prediction using Eq. (6.10). Then the remaining viscoplastic parameters such as Γ^{vp} and N can be determined by minimizing the error between the experimental results of $\Delta\gamma^{vp}/\Delta t$ for the eight stress levels in Figure VI-13 and the prediction using Eq. (6.7). It is noted that σ_y^0 is assumed to be 100 kPa because σ_y^0 is varied proportionally by the change of Γ^{vp}. The identified viscoplastic model parameters at the reference temperature

(21 °C) are summarized in Table VI-2 for FAM and Table VI-3 for full asphalt mixture, where Γ^{vp} for the temperature 40 °C for FAM and 55 °C for full asphalt mixture can be shifted for the reference temperature (21 °C) by multiplying the time-temperature shift factor, such that $\Gamma_0^{vp} = \Gamma^{vp}$ (21 °C)= Γ^{vp} (40 °C)× a_T (40 °C, T_0 = 21 °C) for FAM and $\Gamma_0^{vp} = \Gamma^{vp}$ (21 °C)= Γ^{vp} (55 °C)× a_T (55 °C, T_0 = 21 °C) for full asphalt mixture.

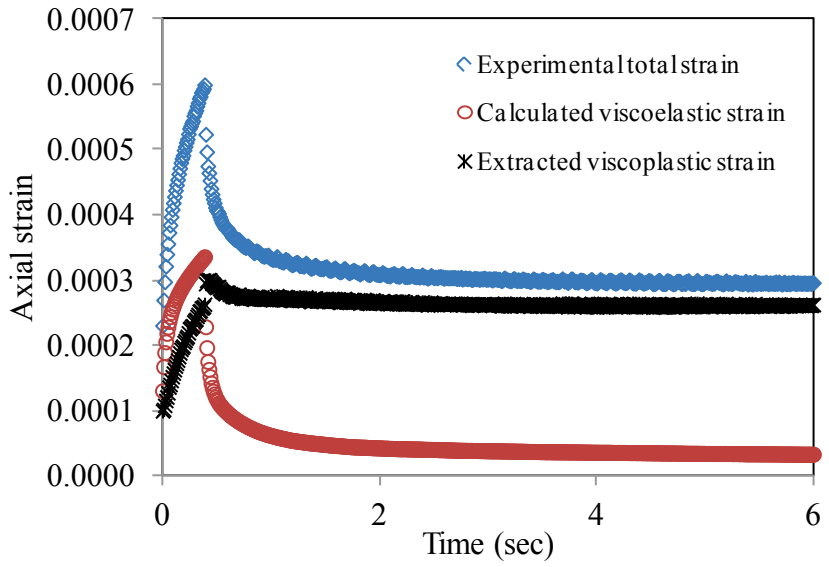

Figure VI-12. The total strain from experimental measurement, the viscoelastic strain calculated using viscoelastic model, and the extracted viscoplastic strain for FAM.

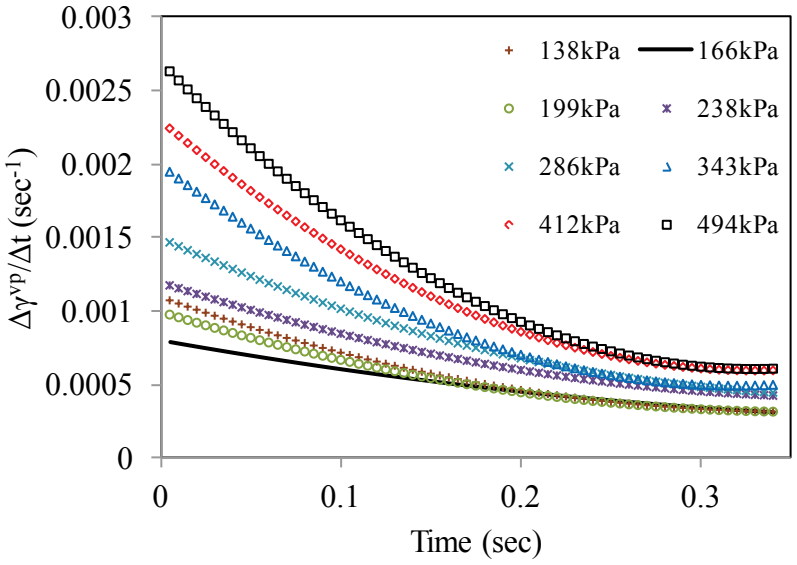

Figure VI-13. $\Delta\gamma^{vp}/\Delta t$ and time diagram for the eight stress levels of the first block of RCRT-VS test for FAM.

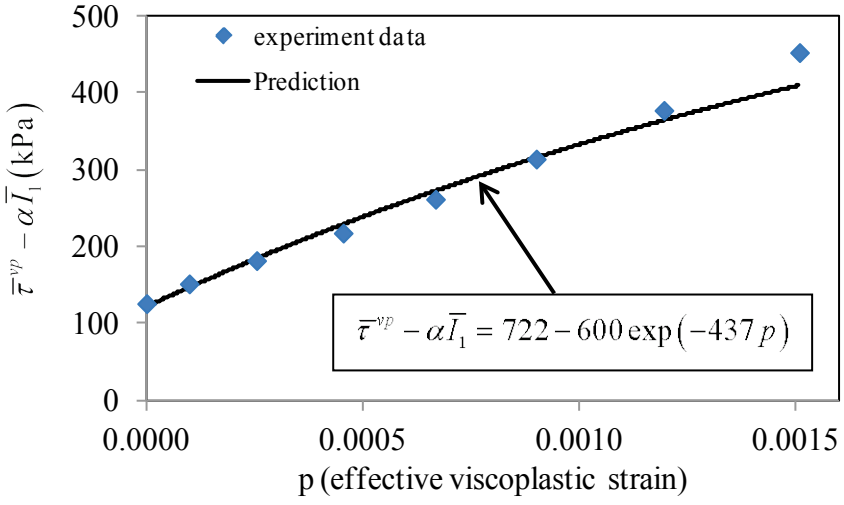

Figure VI-14. Diagram of $\left(\bar{\tau} - \alpha\bar{I}_1\right)$ and the effective viscoplastic strain (p) at the eight stress levels for 0.075% of $\Delta\gamma^{vp}/\Delta t$ for FAM.

VI.4.3 Identification of Viscodamage Parameters

The uniaxial constant tensile strain rate tests at 5 °C were performed to identify the viscodamage parameters. It is a reasonable assumption that the viscoplastic strain at this temperature is negligible. The viscoelastic and viscoplastic parameters identified previously are used to calculate the effective (undamaged) stress, $\bar{\sigma}$. By rearranging Eq. (3.2), the damage density, ϕ, can be expressed as:

$$\phi(t) = 1 - \frac{\sigma(t)}{\bar{\sigma}(t)} \tag{6.11}$$

where $\sigma(t)$ is the nominal (damaged) stress, which is experimentally measured. Taking the natural logarithm of both sides of Eq. (3.29) provides:

$$Ln\left(\dot{\phi}\right) = Ln\left(\frac{\Gamma_0^{vd}}{a_T}\right) + qLn\left[\frac{\bar{\tau}^{vd} - \alpha \bar{I}_1}{Y_0}\right] + kLn\left(\varepsilon_{eff}^{Tot}\right) + D \tag{6.12}$$

where D is constant. As shown in Figure VI-15 (a), the first, third, and fourth terms $(\frac{\Gamma_0^{vd}}{a_T}, kLn\left(\varepsilon_{eff}^{Tot}\right), D)$ in the right-hand side of Eq. (6.12) at a fixed effective strain level $(\varepsilon_{eff}^{Tot})$ are constant. To identify q, the diagram of the damage density rate and $\bar{Y}/Y_0$ at different strain levels is plotted. As shown in Figure VI-15 (b), q can be identified as the slope of the lines. Similarly, by making the first, second, and fourth terms $(\frac{\Gamma_0^{vd}}{a_T}, qLn\left[\frac{\bar{\tau}^{vd} - \alpha \bar{I}_1}{Y_0}\right], D)$ in the right-hand side of Eq. (6.12) at a fixed $\bar{Y}/Y_0$ be constant as shown in Figure VI-16 (a), the diagram of the rate of damage density and the effective strain at different $\bar{Y}/Y_0$ values is plotted. In Figure VI-16 (b), k can be identified as the slope of the lines. The intersections between the lines and Y-axis are used to identify

$\frac{\Gamma_0^{vd}}{a_T}$, where the intersections in Figure VI-15 (b) are the sum of the first and third terms in the right-hand side of Eq. (6.12) and the intersections in Figure VI-16 (b) are the sum of the first two terms in the right-hand side of Eq. (6.12). It is noted that the damage density and the rate of the damage density are zero on the Y-axis in Figure VI-15 (b) and Figure VI-16 (b). The identified viscodamage parameters at the reference temperature (21 °C) are summarized in Table VI-2 for FAM and Table VI-3 for full asphalt mixture.

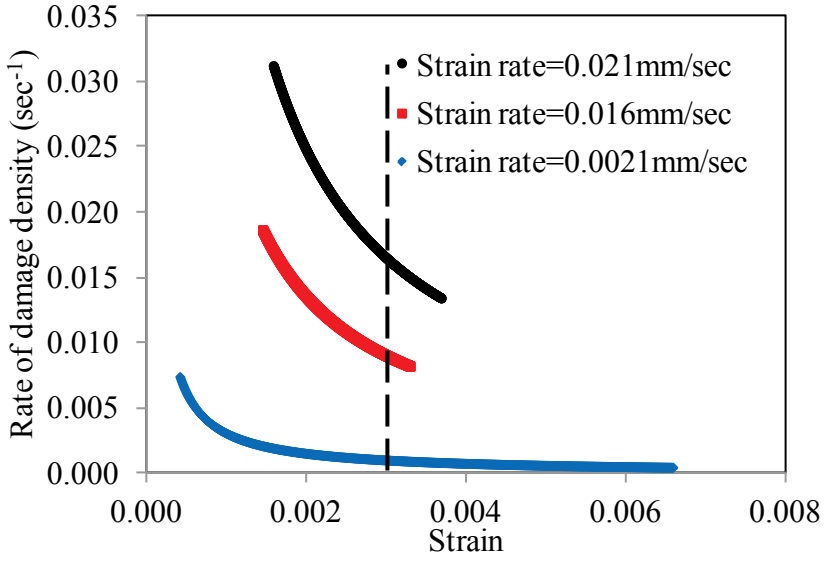

(a)

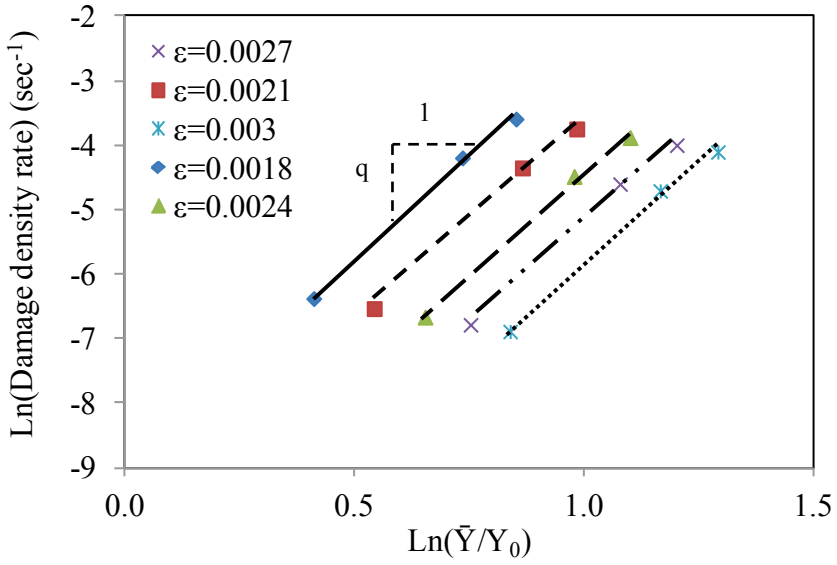

(b)

Figure VI-15. (a) Diagram of rate of damage density and the effective strain at different tensile strain rates at 5 °C; and (b) diagram of damage density rate and $\bar{Y}/Y_0$ at different strain levels for FAM.

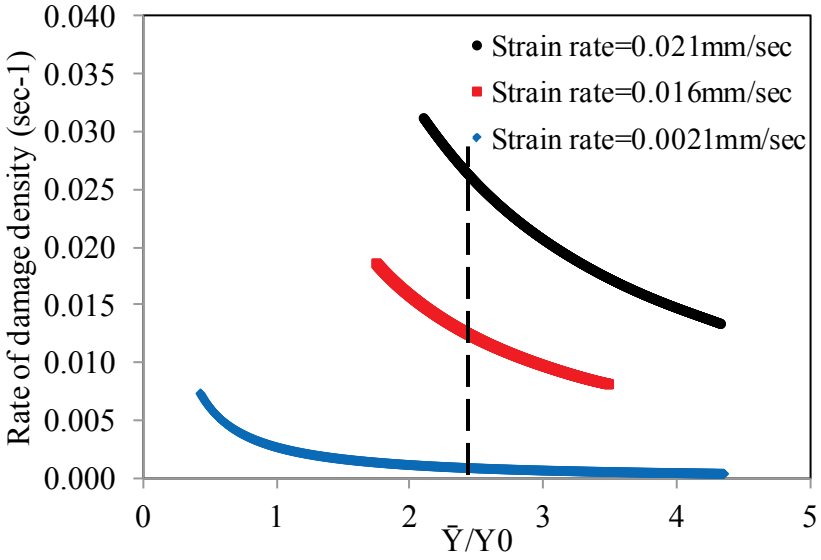

(a)

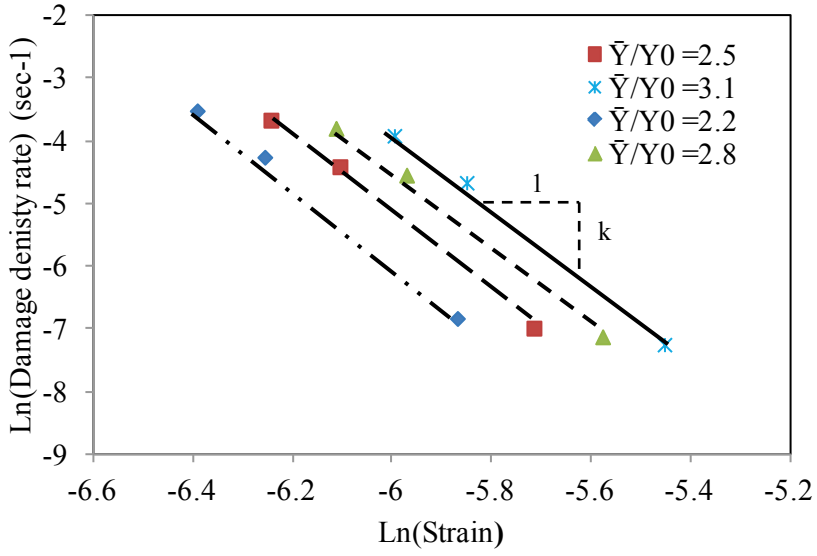

(b)

Figure VI-16. (a) Diagram of rate of damage density and $\bar{Y} - Y_0$ at different tensile strain rates at 5 °C; and (b) diagram of damage density rate and the effective strain at different $\bar{Y}/Y_0$ values for FAM.

VI.4.4 Comparison of the Identified Material Parameters for FAM and Full Asphalt Mixture

As shown in Figure VI-9 (c), dynamic modulus tests show that the complex compliance for full asphalt mixture is less than the one for FAM, meaning that full asphalt mixture is stiffer than FAM. This observation is also shown in comparing the identified viscoelastic parameters for FAM in Table VI-2 with the ones for full asphalt mixture in Table VI-3. Full asphalt mixture has smaller instantaneous compliance (D_0) and transient compliances [67], which results in stiffer material. In addition, it is clear that the time-temperature shift factors for FAM and full asphalt mixture are not significantly different, which is showing that the time-temperature dependency of asphalt mixtures comes from asphalt matrix mainly. Moreover, more viscoplastic strain can be accumulated in FAM that has more binder. The viscoplastic viscosity, Γ_0^{vp}, of FAM in Table VI-2 is greater than that of full asphalt mixture. It is also presented that FAM can harden faster, as the strain hardening rate, κ_2, in Table VI-2 is greater. It can be concluded that FAM is less resistant to permanent deformation. Finally, due to greater q, k, and viscodamage viscosity, Γ_0^{vd}, FAM is damaged more rapidly, as shown in Table VI-2.

VI.5 Validation of Material Parameters

In order to validate the approach used to determine the material parameters obtained above, repeated creep-recovery tests with constant loading time and resting period were conducted using full asphalt mixtures and FAM. Model predictions and experimental measurements for the repeated creep-recovery tests at 40 ºC and 55 ºC using the full mixtures are presented in Figure VI-17 and Figure VI-18, while the results from model

predictions and experimental measurements at 40 ºC using FAM are shown in Figure VI-19. In those figures, 'FAM' indicates the simulation results using the material parameters for FAM in Table VI-2, while 'FULL' refers the model prediction using the material parameters for full asphalt mixture in Table VI-3. It is clear that the predictions using the material parameters for full asphalt mixture agree with the experimental measurements using the full mixtures, as shown in Figure VI-17 and Figure VI-18. Additionally, there is good agreement between the model prediction using the material parameters for FAM and the experimental results using FAM, as shown in Figure VI-19. Furthermore, with longer resting periods, more deviations of the experimental results from the model prediction for full asphalt mixture are shown due to micro-damage healing in the resting period. In other words, the size of micro-damage (micro-cracks and micro-voids) is reduced during the unloading period [25], resulting that less strain are accumulated in the material under longer resting time. However, the micro-damage healing was not considered in the constitutive model used in this study.

Moreover, the different material parameters for FAM and asphalt mixture presented in Table VI-2 and Table VI-3 results in the deviations of simulation results for FAM from the model prediction using the material parameters for full asphalt concrete. In particular, the model predictions of FAM for which κ_2 and Γ_0^{vp} are greater show higher strain value, where κ_2 and Γ_0^{vp} are strain hardening rate and the viscoplastic viscosity in a reference temperature, respectively. Higher q and k for FAM can also influence the simulation results.

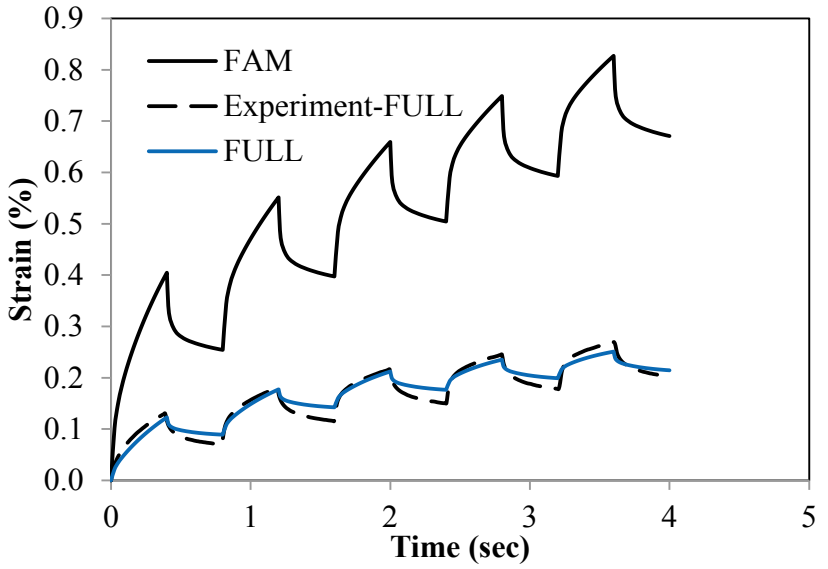

(a)

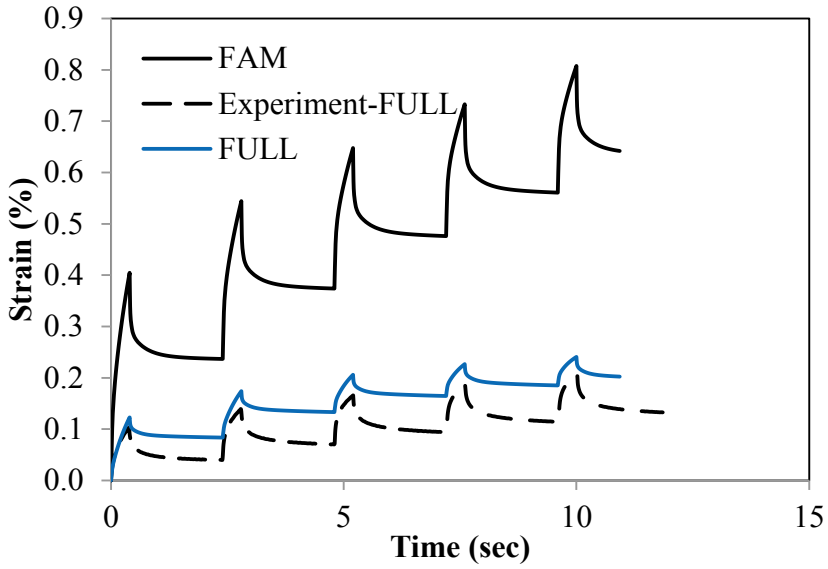

(b)

Figure VI-17. Model predictions and experimental measurements for repeated creep-recovery tests at 40 °C using full mixture with 0.4 seconds of loading time and different resting periods: (a) 0.4 seconds, (b) 2.0 seconds, and (c) 5.0 seconds.

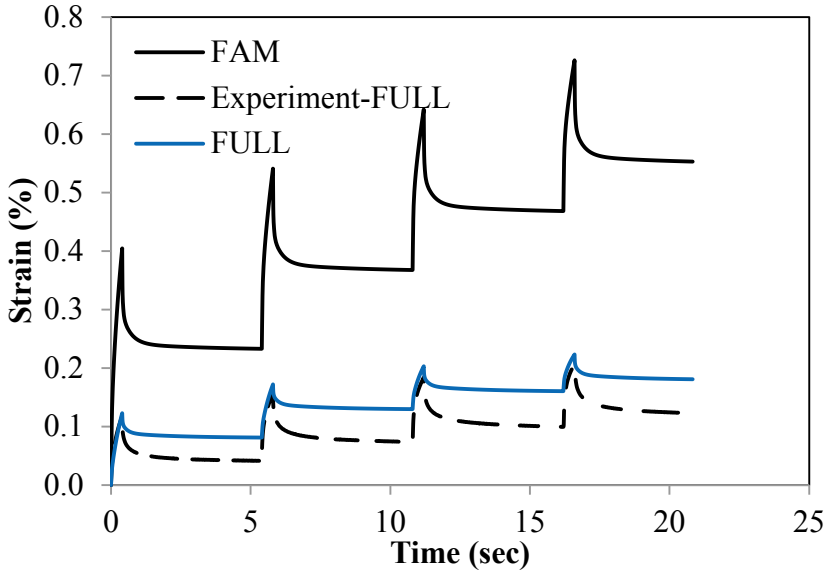

(c)

Figure VI-17 Continued.

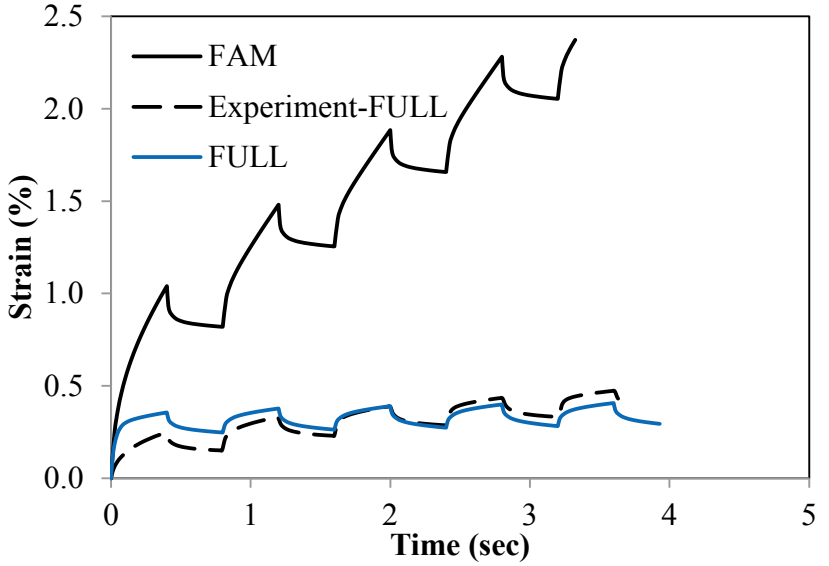

(a)

Figure VI-18. Model predictions and experimental measurements for repeated creep-recovery tests at 55 °C using full mixture with 0.4 seconds of loading time and different resting periods: (a) 0.4 seconds, (b) 1.0 seconds, and (c) 5.0 seconds.

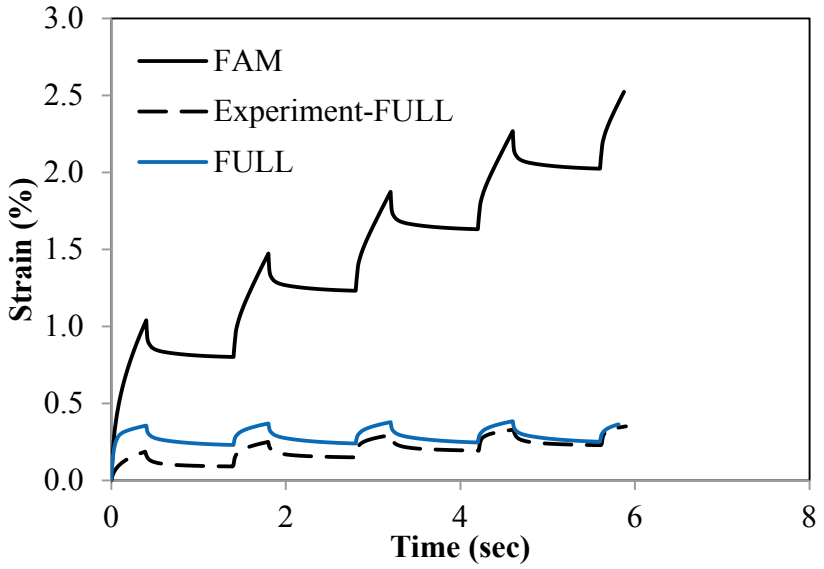

(b)

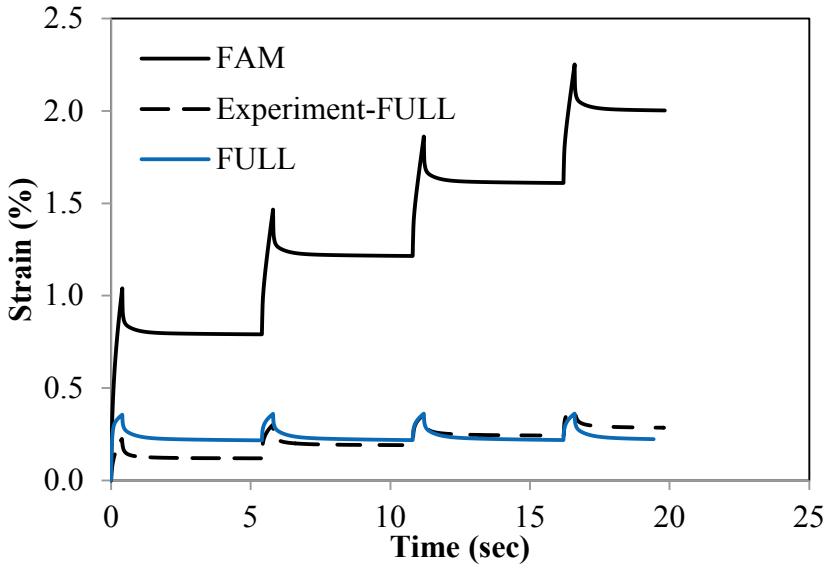

(c)

Figure VI-18 Continued.

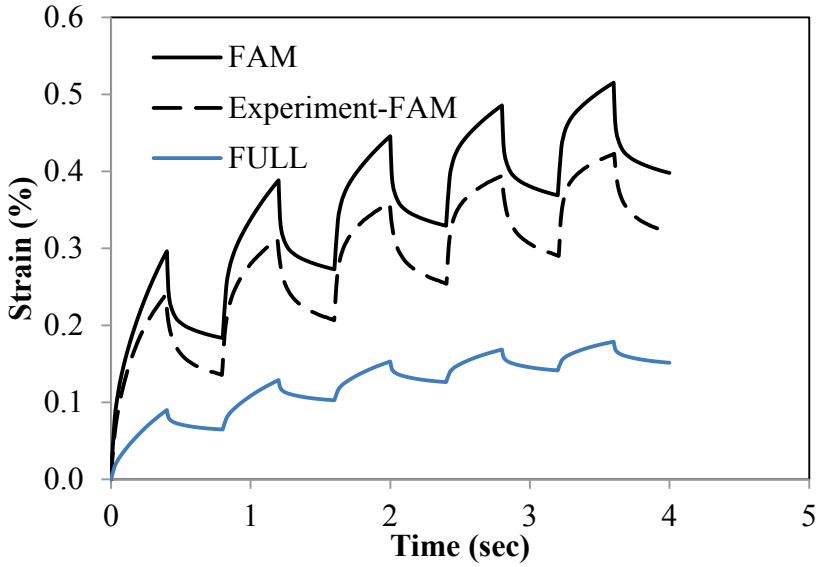

(a)

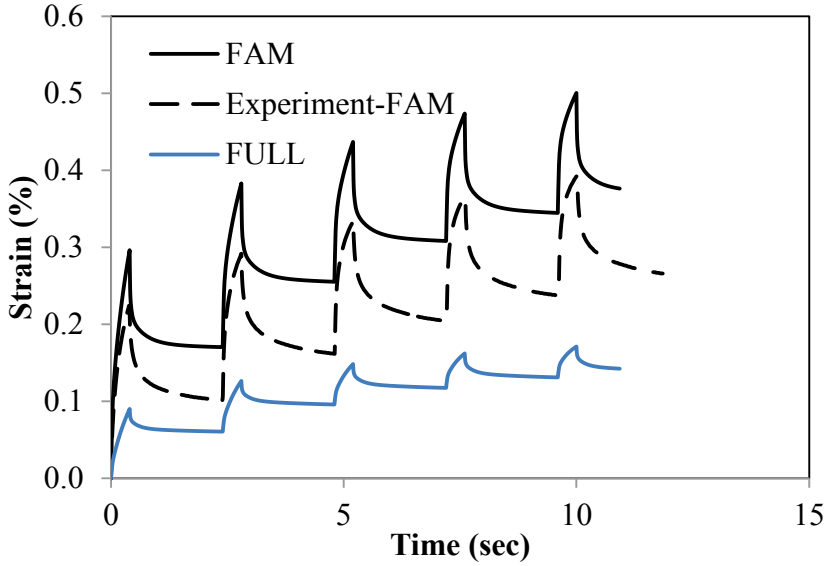

(b)

Figure VI-19. Model predictions and experimental measurements for repeated creep-recovery tests at 40 °C using FAM with 0.4 seconds of loading time and different resting periods: (a) 0.4 seconds, (b) 2.0 seconds, and (c) 5.0 seconds.

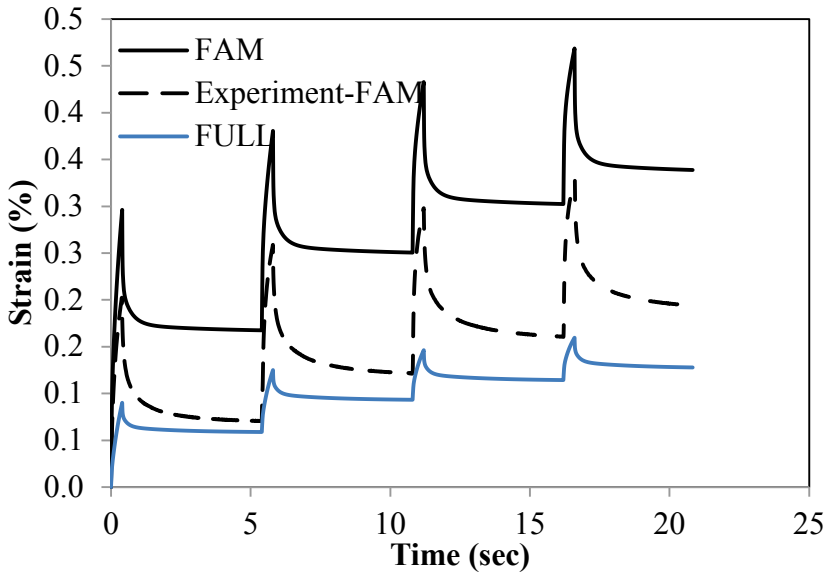

(c)

Figure VI-19 Continued.

VI.6 Conclusions

This chapter presented methods for identifying the constitutive model parameters for FAM and full asphalt mixtures. The identified model parameters were used to better understand the relationship between the FAM and full asphalt mixture responses. The instantaneous compliance and transient compliance for the FAM were greater than the corresponding values of the full asphalt mixture. It was also shown that the FAM accumulated more viscoplastic strains than the full asphalt mixtures; this behavior was reflected in the higher viscoplastic parameters (Γ_0^{vp} and κ_2) of the FAM. In addition, higher values for the viscodamage model parameters (q and k) for the FAM indicate that FAM experiences more damage than the full asphalt mixture.

The model predictions of the FAM and full asphalt mixture were found to be in good agreement with the experimental data using the repeated creep-recovery tests with

various unloading time and temperature values. Deviations of the model prediction from the experimental data were more when longer resting periods were used. This can be improved by accounting for the micro-damage healing mechanism in the constitutive model.

CHAPTER VII

SUMMARY, CONCLUSIONS, AND RECOMMENDATIONS

VII.1 Summary and Conclusions

This dissertation includes a framework for modeling the response of asphalt concrete at the microstructural level. This framework combines the capabilities of a nonlinear thermo-mechanical constitutive models, finite element analysis, and X-ray Computed Tomography (CT). The use of X-ray CT provides more accurate 2D and 3D representations of the asphalt concrete microstructure than the idealized, circular shape particles that were typically used in micromechanical models in the past. The results of the developed modeling framework can be used to provide guidelines for designing microstructures of asphalt concrete that can achieve the desired macroscopic behavior. In addition, this modeling framework allows for conducting 'virtual experiments' in order to save resources and efforts in performing macroscopic experimental tests. These virtual experiments can be conducted for representations of different asphalt concrete mixtures in order to determine the relationship between microscopic and macroscopic responses.

The 2D model presented in chapter IV consists of three phases: aggregate, matrix (i.e., binder with fine aggregates), and the interfacial transmission zone (ITZ). The matrix and the ITZ were considered as thermo-viscoelastic, thermo-viscoplastic, and thermo-damaged materials while the aggregate was considered as an elastic material. The 2D simulations were successful in clearly demonstrating the effects of aggregate

shape, aggregate distribution, aggregate volume fraction, the strength of the ITZ, strain rate, and temperature on the mechanical behavior of asphalt concrete. The 2D computational framework allows one to gain insight on the effects of different microstructural morphologies and different loading conditions on the behavior of asphalt concrete.

In chapter V, 3D micromechanical simulations of the mechanical response of asphalt concrete under various loading conditions were conducted. As it was done for the 2D simulations in chapter IV, the matrix in the 3D microstructure was modeled using a coupled nonlinear-thermo-viscoelastic, thermo-viscoplastic, and thermo-viscodamage model. The aggregate phase was modeled as a linear elastic material. X-ray CT was utilized to scan cylindrical asphalt concrete specimens. The slices of the captured CT images were then used to reconstruct 3D microstructures of stone matrix asphalt (SMA) and dense graded asphalt concrete (DGA).

The rate-, time-, and temperature-dependent responses of asphalt concrete were simulated successfully in 3D simulations. The results showed that asphalt concrete was stronger and more brittle at faster loading rates and lower temperatures. In addition, asphalt concrete was stronger in compression than in tension. Damage density distribution of the 3D microstructure showed that asphalt concrete is more prone to damage at faster loading rates and lower temperatures. Finally, the comparison of the macroscopic and microscopic responses of DGA with continuous gradation and SMA provided insight on the failure mechanisms in these mixtures and on the ability of SMA to sustain more loads.

The results demonstrated that the presented framework including the 3D image-based microstructure and the coupled thermo-viscoelastic, thermo-viscoplastic, and thermo-viscodamage model can be used to predict the macroscopic thermo-mechanical response of asphalt concrete under various loading conditions and temperatures.

Chapter VI presented methods for identifying the constitutive model parameters for Fine Aggregate Mixture (FAM) and full asphalt mixtures. The identified model parameters were used to better understand the relationship between the FAM and full asphalt mixture responses. The instantaneous compliance and transient compliance for the FAM were greater than the corresponding values of the full asphalt mixture. It was also shown that the FAM accumulated more viscoplastic strains than the full asphalt mixtures; this behavior was reflected in the higher viscoplastic parameters (Γ_0^{vp} and κ_2) of the FAM. In addition, higher values for the viscodamage model parameters (q and k) for the FAM indicate that FAM experiences more damage than the full asphalt mixture.

The model predictions of the FAM and full asphalt mixture were found to be in good agreement with the experimental data using the repeated creep-recovery tests with various unloading time and temperature values. Deviations of the model prediction from the experimental data were more when longer resting periods were used. This can be improved by accounting for the micro-damage healing mechanism in the constitutive model.

VII.2 Recommendations

The microstructural modeling framework presented in this dissertation included several attributes that are considered major improvements over previous models. This framework can be further developed and validated in future studies:

1. The results from the microstructural model can be validated by comparing with experimental measurements at different testing conditions (e.g., temperatures, stresses, and loading rates). The comparison can include both macroscopic measurements as well as microscopic measurements of strain and deformation distributions.
2. The constitutive models that are used in this dissertation can be modified in order to include recent developments in accounting for hardening-relaxation and micro-damage healing phenomena. Recent research at Texas A&M University has shown that hardening-relaxation is an important mechanism that should be considered in modeling permanent deformation and micro-damage healing is an integral part of modeling fatigue damage [25, 68].
3. Air voids in particulate composite materials such as asphalt concrete have a significant effect on durability (i.e., moisture damage and aging). In addition, air voids percentage and distribution influence resistance to mechanical loads. The microstructure representations used in this dissertation can be further enhanced to include air voids. This offers the opportunity to evaluate the effect of air voids on performance.

REFERENCES

[1] Collop A, Scarpas A, Kasbergen C, de Bondt A. Development and finite element implementation of stress-dependent elastoviscoplastic constitutive model with damage for asphalt. Transportation Research Record: Journal of the Transportation Research Board. 2003;1832:96-104.

[2] Perl M, Uzan J, Sides A. Visco-elasto-plastic constitutive law for bituminous mixture under repeated loading. Transportation Research Record: Journal of the Transportation Research Board. 1983;911:20-7.

[3] Kim Y, Lutif J, Allen D. Determining representative volume elements of asphalt concrete mixtures without damage. Transportation Research Record: Journal of the Transportation Research Board. 2009;2127:52-9.

[4] Schapery R. On the characterization of nonlinear viscoelastic materials. Polymer Engineering and Science. 1969;9(4):295–310.

[5] Perzyna P. Thermodynamic theory of viscoplasticity. Advances in Applied Mechanics. 1971;11:313-54.

[6] Haj-Ali R, Muliana A. Numerical finite element formulation of the Schapery non-linear viscoelastic material model. International Journal for Numerical Methods in Engineering. 2004;59(1):25-45.

[7] Huang C, Masad E, Muliana A, Bahia H. Nonlinearly viscoelastic analysis of asphalt mixes subjected to shear loading. Mechanics of Time-Dependent Materials. 2007;11(2):91-110.

[8] Lee H-J, Kim YR. Viscoelastic constitutive model for asphalt concrete under cyclic loading. Journal of Engineering Mechanics. 1998;124(1):32-40.

[9] Masad E, Huang C-W, Airey G, Muliana A. Nonlinear viscoelastic analysis of unaged and aged asphalt binders. Construction and Building Materials. 2008;22(11):2170-9.

[10] Sadd M, Dai Q, Parameswaran V, Shukla A. Simulation of asphalt materials using finite element micromechanical model with damage mechanics. Transportation Research Record: Journal of the Transportation Research Board. 2003;1832:86-95.

[11] Abaqus. User's Manual Version 6.8. Providence, RI.: Habbit, Karlsson and Sorensen, Inc.; 2008.

[12] Kim Y-R, Allen D, Little D. Computational constitutive model for predicting nonlinear viscoelastic damage and fracture failure of asphalt concrete mixtures. International Journal of Geomechanics. 2007;7(2):102-10.

[13] Allen DH, Searcy CR. A micromechanical model for a viscoelastic cohesive zone. International Journal of Fracture. 2001;107(2):159-76.

[14] Lai J, Bakker A. 3-D Schapery representation for non-linear viscoelasticity and finite element implementation. Computational Mechanics. 1996;18(3):182-91.

[15] Huang C, ABu Al-Rub R, Masad E, Little D, Airey G. Numerical implementation and validation of a nonlinear viscoelastic and viscoplastic model for asphalt mixes. International Journal of Pavement Engineering. 2011;12(4):433-47.

[16] Lu Y, Wright P. Numerical approach of visco-elastoplastic analysis for asphalt mixtures. Computers & Structures. 1998;69(2):139-47.

[17] Masad E, Dessouky S, Little D. Development of an elastoviscoplastic microstructural-based continuum model to predict permanent deformation in hot mix asphalt. International Journal of Geomechanics. 2007;7(2):119-30.

[18] Masad E, Tashman L, Little D, Zbib H. Viscoplastic modeling of asphalt mixes with the effects of anisotropy, damage and aggregate characteristics. Mechanics of Materials. 2005;37(12):1242-56.

[19] Saadeh S, Masad E. On the relationship of microstructure properties of asphalt mixtures to their constitutive behaviour. International Journal of Materials and Structural Integrity. 2010;4(2):186-214.

[20] Saadeh S, Masad E, Little D. Characterization of asphalt mix response under repeated loading using anisotropic nonlinear viscoelastic-viscoplastic model. Journal of Materials in Civil Engineering. 2007;19(10):912-24.

[21] Seibi AC, Sharma MG, Ali GA, Kenis WJ. Constitutive relations for asphalt concrete under high rates of loading. Transportation Research Record: Journal of the Transportation Research Board. 2001;1767(1):111-9.

[22] Huang C, Abu Al-Rub R, Masad E, Little D. Three dimensional simulations of asphalt pavement performance using a nonlinear viscoelastic-viscoplastic model. Journal of Materials in Civil Engineering. 2011;23(1):56-68.

[23] Darabi M, Abu Al-Rub R, Masad E, Huang C, Little D. A thermo-viscoelastic-viscoplastic-viscodamage constitutive model for asphaltic materials. International Journal of Solids and Structures. 2011;48(1):191-207.

[24] Darabi M, Abu Al-Rub R, Masad E, Little D. A thermodynamic framework for constitutive modeling of time- and rate-dependent materials. Part II: Numerical aspects and application to asphalt concrete. International Journal of Plasticity. 2012;35:67-99.

[25] Abu Al-Rub RK, Darabi M, Little D, Masad E. A micro-damage healing model that improves prediction of fatigue life in asphalt mixes. International Journal of Engineering Science. 2010;48(11):966-90.

[26] Chang G, Meegoda J. Micromechanical model for temperature effects of hot-mix asphalt concrete. Transportation Research Record: Journal of the Transportation Research Board. 1999;1687:95-103.

[27] Abbas A, Masad E, Papagiannakis T, Harman T. Micromechanical modeling of the viscoelastic behavior of asphalt mixtures using the discrete-element method. International Journal of Geomechanics. 2007;7(2):131.

[28] Mahmoud E, Masad E, Nazarian S. Discrete element analysis of the influences of aggregate properties and internal structure on fracture in asphalt mixtures. Journal of Materials in Civil Engineering. 2010;22(1):10-20.

[29] Masad E, Somadevan N. Microstructural finite-element analysis of influence of localized strain distribution on asphalt mix properties. Journal of Engineering Mechanics. 2002;128(10):1105-14.

[30] Papagiannakis A, Abbas A, Masad E. Micromechanical analysis of viscoelastic properties of asphalt concretes. Transportation Research Record: Journal of the Transportation Research Board. 2002;1789:113-20.

[31] Dai Q, Sadd M. Parametric model study of microstructure effects on damage behavior of asphalt samples. International Journal of Pavement Engineering. 2004;5(1):19-30.

[32] Dai Q, Sadd M, You Z. A micromechanical finite element model for linear and damage-coupled viscoelastic behaviour of asphalt mixture. International Journal for Numerical and Analytical Methods in Geomechanics. 2006;30(11):1135.

[33] Dessouky S, Masad E, Little D, Zbib H. Finite-element analysis of hot mix asphalt microstructure using effective local material properties and strain gradient elasticity. Journal of Engineering Mechanics. 2006;132(2):158-71.

[34] Woldekidan M. Performance study of C-Fix in PAC using a 2D finite element model [Thesis]. The Netherlands: Delft University of Technology; 2006.

[35] Mo L, Huurman M, Wu S, Molenaar A. Investigation into stress states in porous asphalt concrete on the basis of FE-modelling. Finite Elements in Analysis and Design. 2007;43(4):333-43.

[36] Collop A, McDowell G, Lee Y. Modelling dilation in an idealised asphalt mixture using discrete element modelling. Granular Matter. 2006;8(3):175-84.

[37] Wu J, Collop A, McDowell G. Discrete element modeling of constant strain rate compression tests on idealized asphalt mixture. Journal of Materials in Civil Engineering. 2011;23(1):2-11.

[38] Mo L, Huurman M, Wu S, Molenaar A. 2D and 3D meso-scale finite element models for ravelling analysis of porous asphalt concrete. Finite Elements in Analysis and Design. 2008;44(4):186-96.

[39] Liu Y, You Z. Visualization and simulation of asphalt concrete with randomly generated three-dimensional models. Journal of Computing in Civil Engineering. 2009;23(6):340-7.

[40] Liu Y, You Z. Accelerated discrete-element modeling of asphalt-based materials with the frequency-temperature superposition principle. Journal of Engineering Mechanics. 2011;137(5):355-65.

[41] Liu Y, You Z. Discrete-element modeling: impacts of aggregate sphericity, orientation, and angularity on creep stiffness of idealized asphalt mixtures. Journal of Engineering Mechanics. 2011;137(4):294-303.

[42] Wang L. Digital specimen and multiple functional digital tester technique for performance evaluation of asphalt mixes. Washington, D. C.: Transportation Research Board; 2007.

[43] You Z, Adhikari S, Dai Q. Three-dimensional discrete element models for asphalt mixtures. Journal of Engineering Mechanics. 2008;134(12):1053-63.

[44] You Z, Adhikari S, Emin Kutay M. Dynamic modulus simulation of the asphalt concrete using the X-ray computed tomography images. Materials and Structures. 2009;42(5):617-30.

[45] You Z, Liu Y, Dai Q. Three dimensional microstructural based discrete element viscoelastic modeling of creep compliance tests for asphalt mixtures. Journal of Materials in Civil Engineering. 2011;23(1):79-87.

[46] Dai Q. Three-dimensional micromechanical finite-element network model for elastic damage behavior of idealized stone-based composite materials. Journal of Engineering Mechanics. 2011;137(6):410-21.

[47] Dai Q. Two-and three-dimensional micromechanical viscoelastic finite element modeling of stone-based materials with X-ray computed tomography images. Construction and Building Materials. 2011;25(2):1102-14.

[48] Masad E, Huang C, DAngelo J, Little D. Characterization of asphalt binder resistance to permanent deformation based on nonlinear viscoelastic analysis of multiple stress creep recovery (MSCR) test. Journal of the Association of Asphalt Paving Technologists. 2009;78:535-66.

[49] Darabi M, Abu Al-Rub R, Masad E, Little D. Thermodynamic-based model for coupling temperature-dependent viscoelastic, viscoplastic, and viscodamage constitutive behavior of asphalt mixtures. International Journal for Numerical and Analytical Methods in Geomechanics. 2012;36(7):817-54.

[50] Abu Al-Rub R, You T, Masad E, Little D. Mesomechanical modeling of the thermo-viscoelastic, thermo-viscoplastic, and thermo-viscodamage response of asphalt concrete. International Journal of Advances in Engineering Sciences and Applied Mathematics. 2011;3(1-4):14-33.

[51] Kachanov L. On time to rupture in creep conditions (in Russian). Izviestia Akadamii Nauk SSSR, Otdelenie Tekhnicheskikh Nauk. 1958;8:26-31.

[52] Abu Al-Rub RK, Voyiadjis G. On the coupling of anisotropic damage and plasticity models for ductile materials. International Journal of Solids and Structures. 2003;40(11):2611-43.

[53] Lemaitre J, Chaboche J. Mechanics of solid materials. Cambridge, UK: Cambridge University Press; 1990.

[54] Tashman L, Masad E, Little D, Zbib H. A micro structure-based viscoplastic model for asphalt concrete. International Journal of Plasticity. 2005;21(9):1659-85.

[55] Dessouky S. Multiscale approach for modeling hot mix asphalt [Disseration]. College Station, Texas: Texas A&M University; 2005.

[56] Abu Al-Rub R, Masad E, Huang C. Improving the sustainability of asphalt pavements through developing a predictive model with fundamental material properties. Final Report submitted to Southwest University Transportation Center, Report # SWUTC/08/476660-0007-1, 54 pages. 2009.

[57] Masad E, Somadevan N, Bahia H, Kose S. Modeling and experimental measurements of strain distribution in asphalt mixes. Journal of Transportation Engineering. 2001;127:477.

[58] You T, Abu Al-Rub R, Darabi M, Masad E, Little D. Three-dimensional microstructural modeling of asphalt concrete using a unified viscoelastic–viscoplastic–viscodamage model. Construction and Building Materials. 2012;28(1):531-48.

[59] Kassem E, Walubita L, Scullion T, Masad E, Wimsatt A. Evaluation of full-depth asphalt pavement construction using X-ray computed tomography and ground penetrating radar. Journal of Performance of Constructed Facilities. 2008;22(6):408-16.

[60] Avizo. Avizo User's Guide. Vordeaux, France: Visualization Sciences Group; 2009.

[61] Bhasin A, Little D, Bommavaram R, Vasconcelos K. A framework to quantify the effect of healing in bituminous materials using material properties. Road Materials and Pavement Design. 2008;9:219-42.

[62] Sousa P, Kassem E, Masad E, Little D. New design method of fine aggregates mixtures and automated method for analysis of dynamic mechanical characterization data. Construction and Building Materials. 2013;41:216-23.

[63] AASHTO. Standard Method of Test for Determining Dynamic Modulus of Hot-Mix Asphalt Concrete Mixtures. TP-62. Washing, D.C.: AASHTO Provisional Standards; 2003.

[64] Han J, Moraga C. The influence of the sigmoid function parameters on the speed of backpropagation learning. From Natural to Artificial Neural Computation: Springer; 1995. p. 195-201.

[65] Park S, Schapery R. Methods of interconversion between linear viscoelastic material functions. Part I—A numerical method based on Prony series. International Journal of Solids and Structures. 1999;36(11):1653-75.

[66] Rahmani E, Abu Al-Rub R, Darabi M, Kaseem E, Masad E, Little D. Effect of Confinement Pressure on the Nonlinear-Viscoelastic Response of Asphalt Concrete at High Temperatures. Transportation Research Board 92nd Annual Meeting. Washington, D.c.: Transportation Research Board; 2013.

[67] Kim Y, Little D. Linear viscoelastic analysis of asphalt mastics. Journal of Materials in Civil Engineering. 2004;16(2):122-32.

[68] Darabi MK, Abu Al-Rub RK, Masad EA, Huang C-W, Little DN. A modified viscoplastic model to predict the permanent deformation of asphaltic materials under cyclic-compression loading at high temperatures. International Journal of Plasticity. 2012.